University of Warsaw, Faculty of Physics
Doctoral thesis

Protocols for selected quantum technologies based on feasible multi-photon bipartite entanglement

Monika E. Mycroft

Supervisor: Dr. habil. Magdalena Stobińska
Co-supervisor: Dr. Thomas McDermott

October 27, 2022

Abstract

Quantum technologies are expected to revolutionise the world. From fast quantum computers through secure quantum communications to precise quantum sensing, quantum protocols promise to outperform their classical equivalents. But in order to achieve that we need robust quantum hardware and protocols which are useful even when that hardware is imperfect. An obvious consideration are losses and inefficiencies but it is equally important not to make unfeasible assumptions. One such example is generating single photon states from a source which is naturally multi-photon under the assumption that the creation of multi-photon components is small.

This thesis proposes two protocols which avoid making this assumption by including all components of the generated states. With this approach we take advantage of the possibilities given by multi-photon states, which include ease of generation and robustness to losses.

The first protocol is an entanglement distribution protocol. We show that the generated multi-photon bipartite entanglement is robust to very high losses in the transmitting channels. As an example we analyse the protocol in settings which point towards its potential application in quantum communications, namely we consider scenarios of Earth-space transmissions or through very long optical fibres. Our entanglement distribution protocol achieves a quadratic improvement of transmission rates compared to the typically used polarization-entangled photon pairs.

The second protocol is designed to provide quantum-enhanced sensitivity in optical phase measurements. Indeed, the multi-photon bipartite entangled states generated with our setup are shown to be robust against losses in the interferometer and perform at least as well as the shot noise limit, the maximal precision achievable with classical light, even at very high losses. The scheme provides an additional possibility of tuning the multi-photon states towards the optimal states which is advantageous if the level of noise in the system is known.

These two examples show that multi-photon technologies are in fact feasible and efficient, and that their properties allow them to outperform protocols based on single photon states.

Streszczenie

Technologie kwantowe mają potencjał by zrewolucjonizować świat. Komputery kwantowe, komunikacja kwantowa czy pomiary kwantowe to przykłady technologii, które – dzięki zastosowaniu specjalnych protokołów kwantowych – mogą okazać się szybsze, bezpieczniejsze i dokładniejsze niż ich klasyczne odpowiedniki. Jednak, aby je zrealizować, potrzebujemy kwantowego hardware'u oraz protokołów, które działają nawet wtedy, gdy ten hardware jest niedoskonały. Należy wziąć pod uwagę nie tylko straty i ograniczoną sprawność urządzeń, ale również realistyczną ocenę przyjętych założeń. Jednym z takich nierealistycznych założeń jest na przykład uznanie, że źródła, które naturalnie produkują stany wielofotonowe, ale w których prawdopodobieństwo powstania par wielofotonowych jest niewielkie, generują pojedyncze fotony.

W rozprawie przedstawiamy dwa nowe protokoły, w których uchylamy to założenie, uwzględniając wszystkie składowe generowanych stanów. Dzięki temu mamy możliwość skorzystania z zalet, jakie dają stany wielofotonowe, takich jak na przykład względnie prosty sposób ich wytwarzania czy odporność na straty.

Pierwszym rozważanym protokołem jest protokół dystrybucji splątania kwantowego. Pokazujemy, że wygenerowane wielofotonowe dwumodowe splątanie jest odporne na bardzo duże straty w kanałach transmisyjnych. Jako przykład analizujemy protokół pod kątem jego potencjalnego zastosowania w komunikacji kwantowej, a mianowicie rozważamy scenariusze transmisji Ziemia-przestrzeń kosmiczna lub przez bardzo długie włókna optyczne. Nasz protokół dystrybucji splątania osiąga kwadratowe przyspieszenie transmisji w porównaniu do typowych protokołów opartych na parach fotonów splątanych polaryzacyjnie.

Drugi protokół zapewnia zwiększoną czułość w pomiarach fazy optycznej. Pokazujemy, że wielofotonowe dwumodowe stany splątane wygenerowane w naszym układzie są odporne na straty w interferometrze i działają co najmniej na granicy szumu śrutowego, czyli maksymalnej precyzji osiągalnej za pomocą światła klasycznego, nawet przy bardzo dużych wartościach strat. Schemat daje dodatkową możliwość dostrojenia stanów wielofotonowych do stanów optymalnych, co jest szczególnie korzystne w sytuacji, gdy znana jest wysokość strat w układzie.

Opisane przykłady pokazują, że kwantowe technologie wielofotonowe rzeczywiście są osiągalne i wydajne, a nawet przewyższają pod względem wydajności i precyzji protokoły oparte na stanach pojedynczych fotonów.

Acknowledgements

I am grateful to the Foundation for Polish Science, "First Team" project No. POIR.04.04.00-00-220E/16-00 (originally FIRST TEAM/2016-2/17) for the funding.

Firstly, I would like to thank my supervisor Dr. habil. Magdalena Stobińska for her guidance, inspiration and being a role model in research. I would also like to thank my second supervisor Dr. Tom McDermott for scrupulously checking my calculations and getting my projects unstuck. My sincere thanks go also to Dr. Adam Buraczewski for teaching me how to code and making sure I am up to date with all the novelties in the scientific world.

Secondly, I am thankful to the experimental quantum optics group of Prof. Ian Walmsley at the University of Oxford, now Imperial College London, for realising the experiment in the quantum metrology part of this thesis. In particular, I would like to thank Dr. Guillaume Thekkadath for discussions and being the driving force of that experiment.

I am also very grateful to my friends Lukas Fiderer, Felix Tennie and Dmitry Manning-Coe for their invaluable comments and proofreading this thesis in the final days before submission.

Last but not least, my thanks go to all my family and friends for helping me on this journey in all the best ways they could.

Contents

Chapter 1

Introduction

At the beginning of the 20th century the quantum theory of matter and energy emerged. This new theory, which would explain the strange behaviours of particles observed in experiments, pictured the world we live in as quantized and probabilistic and laid the foundations for the inventions of the laser and the transistor, the basic building blocks of a computer. Computers revolutionized the world and hence their appearance, because it was enabled by building new devices based on the principles of quantum mechanics, is now referred to as the first quantum revolution [1].

In the first quantum revolution, however, the devices did not use the full capabilities offered by quantum mechanics. Back then full control of the individual systems was not possible but nowadays we have the technology to control quantum systems with unprecedented accuracy and to exploit their properties in completely new ways. This paves the way for the quantum technologies and a second quantum revolution.

Quantum technologies excite a lot of interest as they promise to provide solutions previously unthinkable with classical physics. The phenomena that warrant these solutions are, for example, quantum entanglement and the superposition principle and it is the application of those effects that distinguishes quantum technologies from their classical counterparts.

Entanglement refers to a property of a quantum system whereby the state of one system cannot be considered independently of the another system [2]. This is because the systems share correlations unexplainable by local hidden variable models [3] when local measurements are performed. In particular, entanglement leads to stronger correlations than shared randomness. Entanglement has no classical counterpart and is an important resource that is often used to achieve quantum advantage.

Entanglement manifests itself as a quantum superposition whenever separable states are used as the basis. Superposition relates to the fact that any quantum state can be represented as a sum of two or more distinct states. A quantum object exists thus in two or more distinct states at the same time and only upon measurement (which can include interactions with the environment) does the state decay with some probability into one of its basis states. Thanks to superposition, quantum operations can be done in parallel which promises exponential acceleration for tasks such as predicting properties of physical systems, performing quantum principal component analysis or learning about physical dynamics [4].

Quantum technologies consist of quantum communications and quantum cryptography [5], quantum metrology [6] and quantum sensing [7, 8], quantum computations and quantum computers [9]. Quantum communications and cryptography promise secure in-

formation transfer which, unlike its classical counterpart, relies on the inherent laws of quantum physics to provide unconditional security rather than the hardness of carefully tailored computational problems. Similarly, quantum metrology and sensing protocols benefit from quantum effects in order to deliver ultra-precise measurements. Finally, quantum computations and quantum computers hold promise of outperforming classical computers in some tasks thanks to the possibility of performing entangling measurements across multiple copies of quantum states [4].

It is often the case that protocols in quantum technologies are developed prior to the analysis of their hardware's actual performance. The implementation of these ideas is challenging because suitable hardware is still under development. As quantum systems are very vulnerable to uncontrolled interactions with the environment, knowledge of the hardware's realistic performance is crucial in designing feasible protocols for quantum technologies. This is the approach we take in this thesis. We analyse existing hardware in terms of its actual performance parameters, and then design protocols which can be readily implemented. In this way, we avoid making unfeasible assumptions.

Many different systems have been investigated for their potential to act as platforms for quantum technologies, examples include cold atoms, photons or superconducting materials to name just a few. All of them have advantages and disadvantages and are more suitable to particular tasks than the others. In this thesis, I will focus on quantum photonic hardware as it works particularly well for quantum communications and metrology, the two fields where my protocols find application. This is because, for a photon, information can be encoded in a wide variety of degrees of freedom, e.g. polarization, momentum, energy or photon number. In addition, photons are naturally mobile at room-temperature, they travel at the speed of light and interact only weakly with their environment over long distances, which means they will not suffer much from noise or losses. Moreover, photons can be easily manipulated using linear optical elements, such as beam-splitters, waveplates or mirrors. Finally, photonic sources and detectors are already in advanced stages of development including successful integration on chip [10].

A typical quantum photonic setup consists of a source, a detection system and an interferometer to manipulate the photons but to date, most protocols rely on single photon states [10, 11]. In this thesis I will show that multiphoton bipartite entangled states can also be used to build feasible and efficient quantum technologies. I will support my claim with two protocols, one for quantum communications and one for quantum metrology.

The outline of the thesis is as follows: I will start with a brief overview of the quantum photonics landscape in Chapter 2, introducing the state-of-the-art devices used in the field. Chapter 3 explains the concepts and methods necessary to follow the applications described in Chapters 4 and 5. Chapter 4 demonstrates a protocol to distribute multiphoton entanglement with an application to quantum key distribution and Chapter 5 presents a solution to enhancing optical phase measurements using large photon-number entangled states. Chapter 6 provides a summary and outlook.

Chapter 2

Overview of the quantum photonics landscape

This chapter presents the current state-of-the-art of the quantum photonics landscape. We look into what conditions ideal detectors and sources should satisfy, and what solutions are currently possible. We discuss advantages and disadvantages of the various implementations, and finally look at their realisations on an integrated platform.

2.1 Detectors

An ideal photon detector should click every time a photon enters the detector and should not click when a photon does not enter (i.e. it should not produce false signals, so-called "dark counts"). In addition, it should distinguish exactly the number of photons entering it and restart its operation immediately after detection [10].

Ideal detectors do not exist but there are measures quantifying how much the performance of a realistic detector varies from the ideal one. These measurable quantities are: detector's quantum efficiency (ratio of the output signals to incident photons) η_{d}, reset time (which sets the maximum detection rate) τ_{R}, time jitter (which is the fluctuation between the true arrival time of a photon and the electrically registered arrival time recorded by the system; it sets the minimum time bin size for time stamping photon arrival events) τ_{j}, dark count rate C_{d}, and photon-number-resolving (PNR) capability.

The most commonly used detectors are described in the following subsections.

2.1.1 Avalanche photodiodes

Silicon single-photon avalanche photodiodes (SPAD) operate in the Geiger mode, which means that a single photon incident on the detector triggers an avalanche multiplication process in the p-n junction of the detector [12]. A schematic diagram of this junction is shown in Fig. 2.1. The current excited in the depletion layer grows exponentially until it reaches a steady level. At that point it needs to be quenched by an external circuit and reset for the detector to continue registering incoming photons. In this reset time (also called the dead time) the detector is insensitive. There is also a danger of afterpulsing due to unrecombined free carriers.

The fast increase of the electric current marks the arrival of a photon, however, in the avalanche process the information about the absorbed energy is lost, and the detector thus cannot identify the number of photons which triggered the avalanche. This problem

can be addressed by using a cascaded detection system, where photons enter an array of beam splitters which divides the beam into single photon components with an accuracy increasing with the number of beam splitter layers. However, this process is inefficient with the SPADs as their quantum efficiency is typically limited to $\eta_{\mathrm{d}} \approx 65\%$ [13]. Practically, this implies that the probability of detecting 10 photons simultaneously is less than 1.3%. At telecom wavelengths this efficiency is even lower due to a reduced quantum efficiency of a single detection event at that wavelength which comes from silicon being transparent at the telecom wavelength and other materials not providing such efficient devices.

The advantages of this type of detectors are short reset time ($\tau_{\mathrm{R}} \leq 100\,\mathrm{ns}$) and low noise ($C_{\mathrm{d}} \sim 100$ counts per second). Because they are inexpensive, they are a popular option for many single-photon experiments.

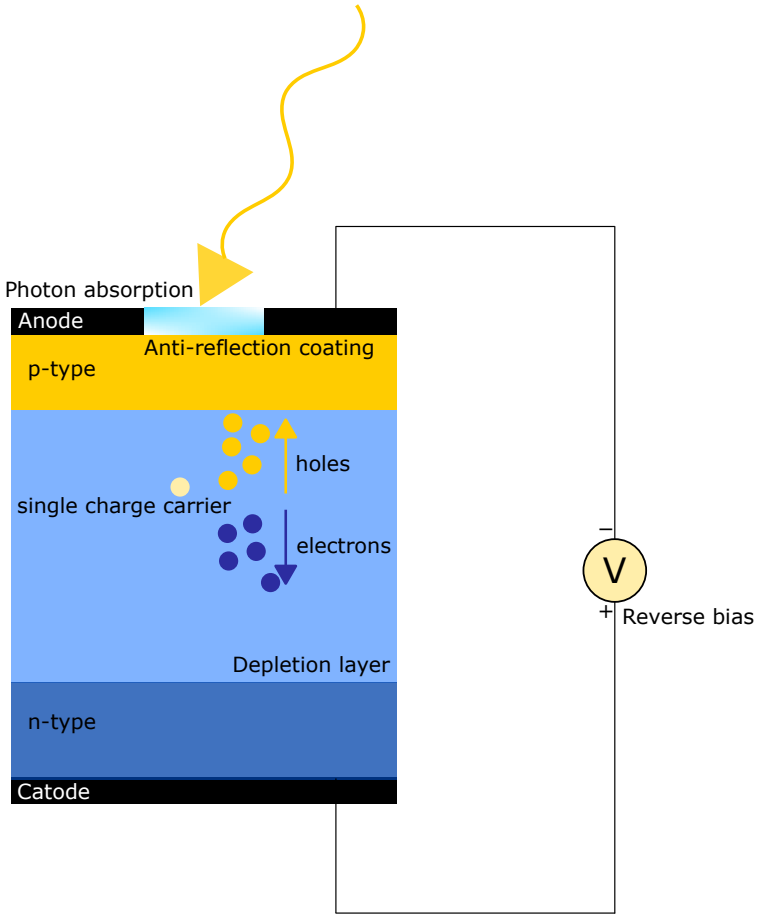

Figure 2.1: A schematic diagram of the p-n junction in a single-photon avalanche photodiode (SPAD). The reverse bias voltage sets a very high electric field in the depletion layer where no free carriers are present. When a single charge carrier is injected into this layer via the photoelectric effect, it is strongly accelerated and ionizes the atoms in the depletion layer creating an electron-hole pair. This starts a self-sustaining avalanche multiplication process, which generates an electric current that grows exponentially until it saturates to a constant level. The anti-reflection coating increases the device's efficiency.

2.1.2 Superconducting nanowire single-photon detector

An improvement on the SPAD in terms of the detection efficiency is the superconducting nanowire single-photon detector (SNSPD), which can achieve $\eta_d = 98\%$ [14] in the telecom wavelength range. The principle of operation of these detectors relies on the superconducting transition. The device consists of a thin loop made of a superconducting material through which an electric current close to the critical current is passed. When a single photon hits the detector, the energy absorbed lowers the critical current transitioning the device to normal resistivity and the voltage spike associated with the current diverting into a parallel load impedance is filtered and amplified, and registered as a detection. The detector becomes insensitive to subsequent photons while the current is not flowing through the superconducting material until it cools down and its resistivity decreases. A brief explanation of the principle of operation of this detector is provided in Fig. 2.2.

In terms of other properties, the SNSPDs have a timing jitter of ≈ 30 ps, comparable reset time to SPADs ($\tau_R \approx 40$ ns) and dark count rates C_d lower than $100\,s^{-1}$. The superconducting material can be chosen to optimize the performance for a given wavelength so that the detectors have high efficiencies for a large range of the optical spectrum. The drawback of SNSPDs is that they require cryogenic temperatures in order to maintain the superconducting properties of the material. They also do not possess photon-number-resolving capabilities, although there exist schemes which allow photon-number-resolution to some degree [15].

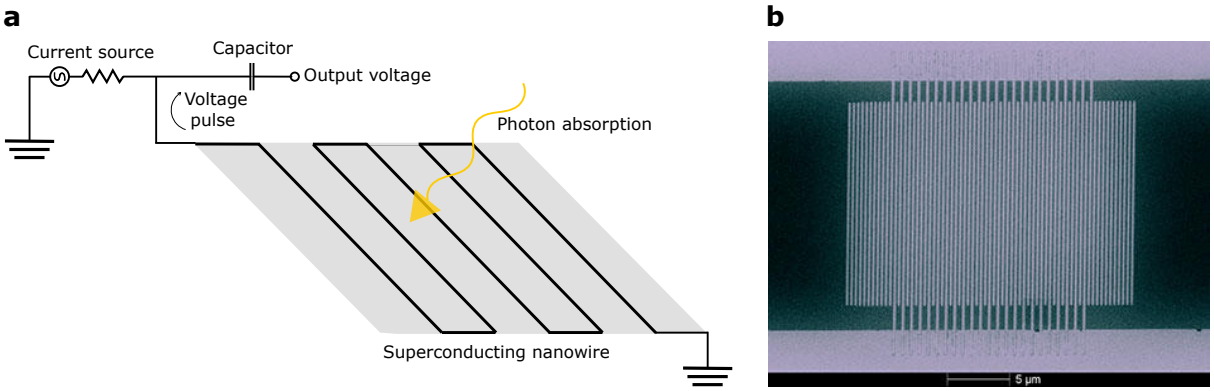

Figure 2.2: **a)** A schematic diagram of the superconducting nanowire single-photon detector. Absorption of a photon by the superconducting thin nanowire placed on a substrate results in local destruction of the superconducting state which spreads via Joule heating along the whole wire. The resistance grows to a few kΩ and therefore the current diverts into the parallel load impedance which produces a measurable voltage pulse. During the response time the detector is insensitive to any other incoming photons as there is no longer a current flowing in the nanowire. **b)** Colorized micrograph of a NIST single-photon detector made of superconducting nanowires patterned on molybdenum silicide. *Credit: Verma/NIST* [16].

2.1.3 Transition edge sensor

The first detector that has been shown to be truly photon-number-resolving is the transition edge sensor (TES), see Fig. 2.3 for a schematic diagram and photo. TES detectors are very sensitive microbolometers (devices that work by exploiting temperature dependent resistance) that are inherently energy resolving and therefore can be used to, e.g.

resolve photon number for a monochromatic source of light. For optical applications the device is usually made with a tungsten film embedded in an optical cavity optimized for a particular wavelength. The film needs to be cooled down below its superconducting critical temperature $T_c \approx 100$ mK and a voltage bias is applied in order to raise the temperature of the detector to the superconducting-to-normal transition. The steep slope of the resistive transition allows for small temperature changes to be measured. When light is absorbed by the TES, the temperature of the sensor increases and so does the electrical resistance. The resulting change in the magnetic flux is detected by an array of superconducting quantum interference devices (SQUIDs), and then amplified. An integrating circuit converts this signal to a voltage that is proportional to the photon number. Alternatively, a matched filtering technique can be used to determine the photon number [17]. Finally, the device is reset through a thermal link to a cold bath.

Compared to the other two types of detectors, the TES achieves quantum efficiency as high as the SNSPD, $\eta_d \geq 95\%$ [18], with 98% reported in Refs [19, 20]. They posses excellent PNR capabilities implementing to a good approximation a projective measurement [21] and resolving up to 29 photons [22]. Moreover, there is active development to increase this number to the hundreds and this should be attainable in a few years from now [23]. The disadvantage of the TES, however, is its slow operation. They need $\sim 5\ \mu$s to reset – at least two orders of magnitude more than SNSPDs – and the time jitter is $\tau_j \geq 50$ ns. In addition, since it is a bolometer device and relies on an analogue process, it is susceptible to analogue noise, in contrast to SPADs and SNSPDs which are digital. Still, the TES is to date the most advanced detector and the only one possesing true PNR capabilities, which makes it desirable in protocols involving multiphoton states.

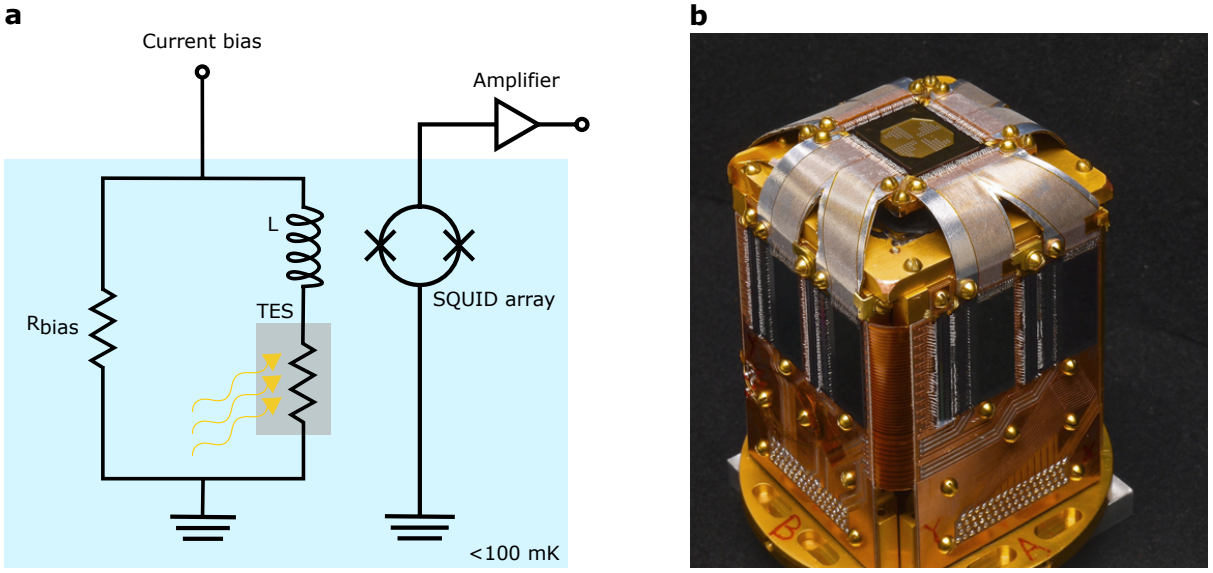

Figure 2.3: **a)** The circuit for operating the TES. Components inside the blue box are held at below 100 mK while the amplification can be performed at room temperature. When light is absorbed by the TES, the electrical resistance increases and the subsequent change in the magnetic flux generated by the inductor L is measured by an array of SQUIDs - very sensitive magnetometers. **b)** Photo of a TES detector (places at top of the device). *Credit: Dan Schmidt/NIST* [24].

2.2 Photonic sources

An ideal photon source should satisfy the following requirements [10]: (1) the generated photons must be efficiently collected without being lost so that they can be processed further, (2) they must be created in a pure quantum state and be indistinguishable from each other and (3) they must be compatible with the chosen detection strategy.

Efforts to satisfy all these conditions and create the ideal source have led to proposals coming from diverse physical systems, e.g. quantum dots [25, 26], trapped ions [27] and atoms [28], colour centres in diamonds [29, 30] or carbon nanotubes [31]. These methods are known to be "on-demand" or deterministic as they rely on the use of a single emitter, but in reality they become probabilistic in operation due to emission or extraction losses [11].

The most advanced on-demand source is the quantum dot [32]. A quantum dot is a single artificial atom grown in a semiconductor, which allows an exciton (electron-hole pair) to be produced and emission of a single photon in the resulting process of radiative recombination. Quantum dots have exceptional brightness, that is probability of providing a single photon per excitation pulse, which has led to demonstrations of new quantum computation experiments, such as boson sampling [33, 34]. On the other hand, quantum dots suffer from low coupling efficiency to single-mode fibres, which are the typical medium of transmitting photons through an optical network, and the difficulty of generating indistinguishable photons. The latter issue is connected to each quantum dot being spectrally different from others as a result of structural and environmental inhomogeneities, but there are ways to mitigate its effect for example by tuning the emission spectrum [35], or demultiplexing the emitted photons into different spatial channels and delaying them so that they can be output simultaneously [36].

Apart from on-demand sources, there are also naturally probabilistic sources based on, e.g. the spontaneous parametric down conversion (SPDC) process [37, 38, 39] or atomic ensembles [40]. These sources emit photons in correlated pairs, therefore one photon of the pair can be used to herald the creation of the other. The best performing sources of single or entangled photons are those based on SPDC and they are the standard source in experimental quantum optics nowadays [2]. SPDC sources have been shown to provide pure, highly indistinguishable photons at room temperature with high efficiency. Since they also produces multiphoton pairs with non-zero probability, they find applications in technologies using multiphoton entanglement and this is why I will focus specifically on the characteristics of SPDC sources in the following subsection.

2.2.1 Spontaneous parametric down conversion

The SPDC process is a three-wave mixing process which can occur in materials with second-order nonlinear optical susceptibility, $\chi^{(2)}$, such as, e.g. KDP (potassium dideuterium phosphate), BBO (beta barium borate) or $LiNbO_3$ (lithium niobate). These materials react in the presence of an electric field, $E(t)$, in a nonlinear way. This means that their polarization, $P(t)$, will depend quadratically on the applied electric field, $P(t) = \epsilon_0 \chi^{(2)} E^2(t)$, where ϵ_0 is the permittivity of free space. This can lead to a down conversion process, when a higher-energetic pump photon of momentum $\vec{k}_P$ and frequency (energy) ω_P from a laser is converted into two lower-energetic photons (usually referred to as signal and idler) of frequency $\omega_{s/i}$ and momentum $\vec{k}_{s/i}$ according to the momentum

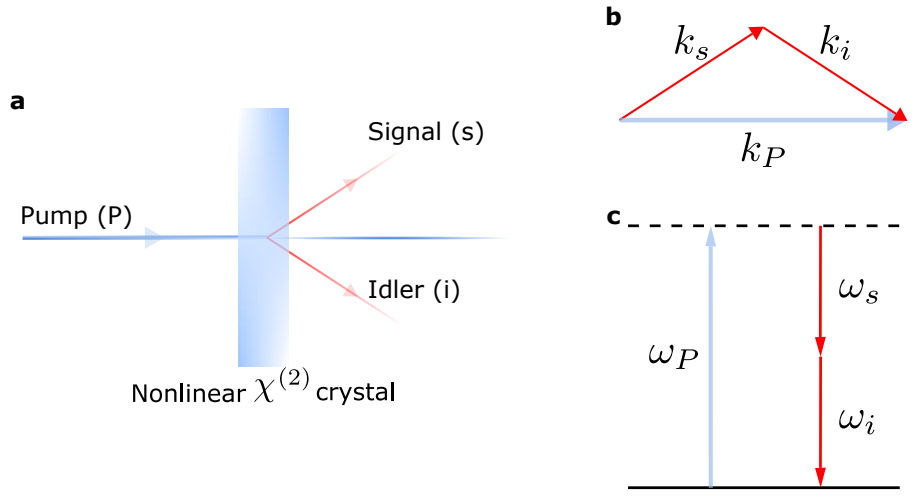

Figure 2.4: **a)** A schematic diagram of the spontaneous down conversion process. A laser is directed at a nonlinear crystal with $\chi^{(2)}$ nonlinearity. The laser contains so-called pump photons (blue) which are converted spontaneously into two photons (red) which conserve momentum (as shown in **b**) and whose frequencies sum up to the frequency of the pump photon (as shown in **c**). These two emerging photons are typically called the signal (s) and idler (i).

and energy conservation laws

$$\vec{k}_P = \vec{k}_s + \vec{k}_i, \tag{2.1}$$

$$\omega_P = \omega_s + \omega_i, \tag{2.2}$$

where P, s, i stand for pump, signal and idler, respectively. A schematic diagram of this process is shown in Fig. 2.4.

The above equations are usually known as phase matching conditions [41]. Eq. 2.1 can be satisfied for different combinations of polarization and frequencies depending on the properties of a given material. In general, when the two output photons have the same polarization but are orthogonal to the pump, we refer to the process as type-I SPDC, whereas when the two output photons have orthogonal polarizations, we refer to it as type-II SPDC. A type-0 phase matching is also possible when all polarizations are aligned, including the pump photon, but it requires additional engineering involving a technique known as quasi-phase matching (QPM) [42]. The simplest form of QPM is to periodically change the sign of the crystal nonlinearity which is referred to as periodic poling, see Fig. 2.5. QPM can also be applied to type-I and -II SPDC for additional controllability and loss reduction.

Periodically poled crystals make several orders brighter sources than traditional SPDC devices [43]. The most popular crystals in this family are periodically poled potassium titanyl phosphate (PPKTP) and periodically poled lithium niobate (PPLN). They offer high resistance to laser damage and show high birefringence. Thanks to these qualities they have been widely used in quantum communications, quantum entanglement tests and other experiments involving multiphoton states.

The parametric down-conversion process can be realised in two regimes: at the parametric approximation when the pump is treated classically and only a fraction of the photons is converted to the signal and idler fields, and at the high gain regime when the pump becomes depleted. At the parametric approximation regime, the number of down-

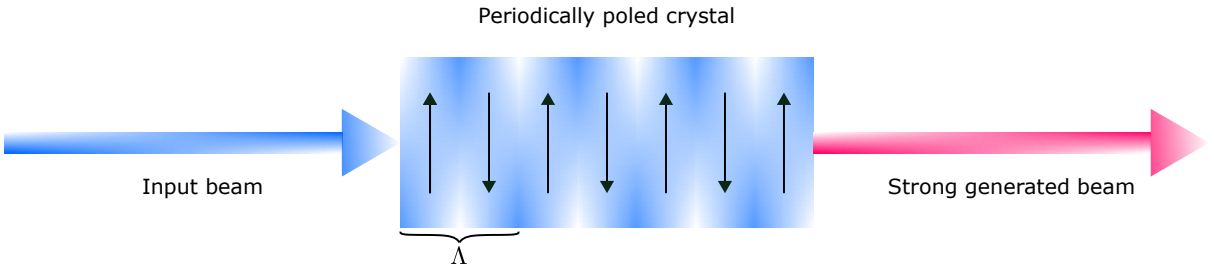

Figure 2.5: Schematic drawing of a periodically poled crystal which enables quasi-phase matching. The domains of the crystal have periodically alternating orientations so that the nonlinearity flips sign from $+\chi^{(2)}$ to $-\chi^{(2)}$ and back. The poling period Λ determines the wavelengths for which the quasi-phase matching and therefore efficient down conversion can be achieved.

converted photons, N_{SPDC}, follows an exponential growth with respect to the applied pump power. It can be described by the following relation

$$N_{\text{SPDC}} = \sinh^2 g, \tag{2.3}$$

where g is the parametric gain [44] which depends quadratically on the pump field amplitude, $g \propto |E_P|^2$.

The parametric approximation regime breaks down at different levels for different materials. For example, in the case of BBO crystals the pump power required to enter the high gain regime is tens of milliwatts [45]. At high gain the majority of the pump power goes into conversion to the signal and idler photons (we say the pump is depleted), which results in a linear growth in the number of SPDC photons. In this thesis, we will only consider the non-depletion regime, which corresponds to $g \sim 0.1 - 0.5$.

The produced photon pairs often carry correlations in frequency and transverse momentum, which are undesirable because the detection of one photon of the pair will herald the other one into a mixed state. This prevents interference between independent sources which is central to many experiments and protocols in quantum physics [46]. The tool to characterize the amount of correlations between the two modes is the joint spectral amplitude (JSA) [12]

$$f(\omega_s, \omega_i) = \alpha(\omega_s + \omega_i)\Phi(\omega_s, \omega_i). \tag{2.4}$$

It is a product of the pump spectral amplitude $\alpha(\omega_s+\omega_i)$, which is typically described by a Gaussian function and ensures that energy is conserved (Eq. 2.2), and the phase-matching function $\Phi(\omega_s, \omega_i)$ which is defined by the optical properties of the nonlinear crystal and guarantees momentum conservation (Eq. 2.1). More explicitly, they are given as

$$\alpha(\omega_P = \omega_s + \omega_i) = \frac{1}{\sigma\sqrt{2\pi}} \exp\left(-\frac{(\omega_P - \omega_0)^2}{2\sigma^2}\right), \tag{2.5}$$

for the pump central frequency ω_0 and bandwidth σ, and

$$\Phi(\omega_s, \omega_i) = \text{sinc}\left(\frac{\Delta k L}{2}\right), \tag{2.6}$$

for a crystal of length L and where $\Delta k = k(\omega_P) - k(\omega_i) - k(\omega_s)$ is the wavevector mismatch. Ideally, $\Delta k = 0$ to maximize the phase-matching function. The JSA is a measure of the modal purity of the SPDC source. When the JSA is decorrelated, i.e. $f(\omega_s, \omega_i) =$

$f(\omega_s)f(\omega_i)$, the output state is known to be in a single spectral mode and carries no spectral correlations, as is desired.

The residual spectral entanglement can be removed by applying a group velocity matching scheme [47]. It allows control over the joint spectrum of the signal and idler photons by carefully engineering the relative group velocities of the pump, signal and idler, and by adjusting the pump laser bandwidth, SPDC crystal length and choosing the right material. That way, spectral filtering, which introduces losses to the already quite inefficient SPDC process, is no longer necessary.

Another way of improving the SPDC source and reducing losses is the application of waveguides rather than bulk crystals to generate entangled photons. Waveguides are specially engineered crystallographic structures that confine and guide light into a discrete set of modes. The confinement of the three interacting waves over a small transverse area leads to extremely high field amplitudes which increase the down conversion rate by a few orders of magnitude [48]. It also allows efficient coupling to optical fibers and integration of the source on an optical chip, which will be discussed further in the following section.

With these modifications SPDC is capable of emitting almost-identical, single-mode and almost-Gaussian modes, paving the way towards an ideal source of entangled or heralded photon-number states.

2.2.2 Two-mode squeezed vacuum

The natural product of the SPDC process is the two-mode squeezed vacuum (TMSV) state. The Hamiltonian generating these states takes the form [49]

$$\hat{\mathcal{H}} = \hbar\omega_s\hat{a}^\dagger\hat{a} + \hbar\omega_i\hat{b}^\dagger\hat{b} + \hbar\omega_P\hat{c}^\dagger\hat{c} + i\hbar\chi^{(2)}(\hat{a}\hat{b}\hat{c}^\dagger - \hat{a}^\dagger\hat{b}^\dagger\hat{c}), \tag{2.7}$$

where the c mode contains the pump field and a and b correspond to the signal and idler modes, respectively. We assume the pump to be a strong coherent state $|\gamma e^{-i\omega_P t}\rangle$ which is unaffected by the wave-mixing process. Thus the parametrically approximated Hamiltonian is then

$$\hat{\mathcal{H}}^{(\mathrm{PA})} = \hbar\omega_s\hat{a}^\dagger\hat{a} + \hbar\omega_i\hat{b}^\dagger\hat{b} + i\hbar(\zeta^* e^{i\omega_P t}\hat{a}\hat{b} - \zeta e^{-i\omega_P t}\hat{a}^\dagger\hat{b}^\dagger), \tag{2.8}$$

where $\zeta = \chi^{(2)}\gamma$ quantifies the strength of the interaction. In the interaction picture, the Hamiltonian becomes

$$\hat{\mathcal{H}}_{\mathrm{I}} = i\hbar(\zeta^* e^{i(\omega_P-\omega_s-\omega_i)t}\hat{a}\hat{b} - \zeta e^{i(\omega_P-\omega_s-\omega_i)t}\hat{a}^\dagger\hat{b}^\dagger). \tag{2.9}$$

Applying Eq. 2.2 to conserve energy, reduces it to its time-independent form

$$\hat{\mathcal{H}}_{\mathrm{I}} = i\hbar(\zeta^*\hat{a}\hat{b} - \zeta\hat{a}^\dagger\hat{b}^\dagger). \tag{2.10}$$

The evolution under this Hamiltonian for a time $t = \tilde{g}/\zeta$, where $\tilde{g}$ is the parametric gain, corresponds to the following unitary

$$\hat{S}(\tilde{g}) = \exp[-i\hat{\mathcal{H}}_{\mathrm{I}}t/\hbar] = \exp\left[(\tilde{g}\hat{a}^\dagger\hat{b}^\dagger - \tilde{g}^*\hat{a}\hat{b})\right], \tag{2.11}$$

which we recognize as the two-mode squeezing operator [50]. We note that this operator either creates or annihilates photons pair-wise from each mode, thus generating a bipartite entangled state with strong correlations between the two modes.

To see this more directly let us apply the squeezing operator to the initially empty signal and idler modes $|0\rangle_s|0\rangle_i$

$$|\Psi_{\text{TMSV}}\rangle = \hat{S}(\tilde{g})|0\rangle_s|0\rangle_i = e^{\tilde{g}\hat{a}^\dagger\hat{b}^\dagger - \tilde{g}^*\hat{a}\hat{b}}|0\rangle_s|0\rangle_i. \tag{2.12}$$

Writing $\tilde{g} = ge^{i\theta}$, θ can be interpreted as the angle at which the states are squeezed in the quadrature space. We will assume $\theta = 0$. Using the disentangling theorem for the $SU(1,1)$ Lie algebra [51, 52]

$$e^{\tilde{g}\hat{a}^\dagger\hat{b}^\dagger - \tilde{g}^*\hat{a}\hat{b}} = e^{\tanh(g)\hat{a}^\dagger\hat{b}^\dagger} e^{\frac{1}{2}\ln\left(\frac{1}{\cosh^2(g)}\right)(\hat{a}^\dagger\hat{a}+\hat{b}^\dagger\hat{b}+1)} e^{-\tanh(g)\hat{a}\hat{b}}, \tag{2.13}$$

we can rewrite the equation for the TMSV as

$$|\Psi_{\text{TMSV}}\rangle = \frac{1}{\cosh(g)} \sum_{n=0}^{\infty} \tanh^n(g)|n\rangle_s|n\rangle_i. \tag{2.14}$$

We observe that only paired states occur in the superposition and the average photon number in each mode is the same:

$$\langle\hat{n}_s\rangle = \langle\hat{n}_i\rangle = \sinh^2(g). \tag{2.15}$$

Interestingly, if each mode is considered independently, the probability of finding n photons in a single mode follows a thermal distribution, radiating with temperature $T = \frac{\hbar\omega}{2k_{\text{B}}\ln(\coth g)}$, where k_{B} is the Boltzmann constant and ω corresponds to either ω_i for the idler mode or ω_s for the signal mode. In other terms, the statistics are super-Poissonian, which means that the variance $\langle(\Delta\hat{n}_{s,i})^2\rangle = \sinh^2(g)\cosh^2(g)$ is larger than the mean $\langle\hat{n}_{s,i}\rangle$ for each of the modes (as the cosh function is always greater than or equal to 1).

Still, the state exhibits strong photon number correlations, which are manifested by the linear correlation coefficient, defined as [49]

$$J(\hat{n}_s, \hat{n}_i) = \frac{\text{cov}(\hat{n}_s, \hat{n}_i)}{\langle(\Delta\hat{n}_s)^2\rangle^{1/2}\langle(\Delta\hat{n}_i)^2\rangle^{1/2}}, \tag{2.16}$$

where the covariance of the photon numbers is defined as $\text{cov}(\hat{n}_s, \hat{n}_i) = \langle\hat{n}_s\hat{n}_i\rangle - \langle\hat{n}_s\rangle\langle\hat{n}_i\rangle$, and takes its maximal value for the TMSV state:

$$J(\hat{n}_s, \hat{n}_i) = 1. \tag{2.17}$$

In a more compact form Eq. 2.14 can be written as

$$|\Psi_{\text{TMSV}}\rangle = \sum_{n=0}^{\infty} \sqrt{\lambda_n}|n\rangle_s|n\rangle_i, \tag{2.18}$$

where $\sqrt{\lambda_n} = \frac{\tanh^n(g)}{\cosh(g)}$. Plotting the probability λ_n of detecting n photons in one of the modes (Fig. 2.6) we see that it decreases exponentially with the vacuum and single-photon pairs as the most probable states. However, the probabilities follow a geometric progression with common ratio $\frac{\lambda_{n+1}}{\lambda_n} = \tanh^2(g)$, therefore the SPDC produces a considerable amount of multi-photon events. The amount increases with the parametric gain g and thus SPDC is a natural source of multiphoton bipartite entangled states.

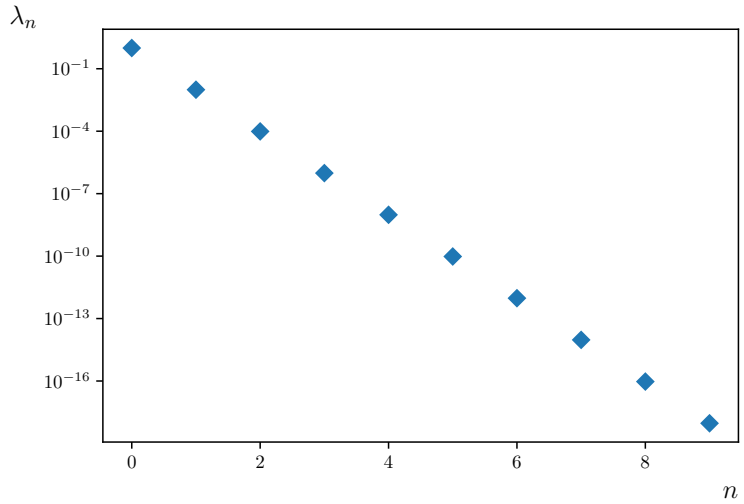

Figure 2.6: Probability of obtaining different numbers of photons in a heralded mode of the two-mode squeezed vacuum via a photon-number-resolving measurement. The most probable events are the vacuum and single-photon pairs but multiphoton occurences should not be neglected. Here, the probability was calculated for parametric gain $g = 0.1$.

2.3 Integrated quantum photonics

Photonic sources, detectors or any other optical element must also exist in an integrated form in order to have technological scalability and miniaturization necessary for real-life applications. An integrated quantum optical chip will be characterized by its density of optical components, propagation and coupling losses and the ability and speed of active reconfiguration [10].

The most popular materials for realizing integrated quantum photonics are glass [53], lithium niobate [54] and silicon [55]. Each of them posseses different advantages. In glass it is possible to write 3D interferometric networks of waveguides using a femtosecond laser [56]. Lithium niobate is well known from classical integrated photonics due to its excellent electro-optical and nonlinear optical properties and ease of fabrication. It offers efficiency and high stability [57]. Silicon-based optical chips on the other hand promise very high density of optical components and even smaller chip size than the other materials, low loss and compatibility with CMOS microelectronics [58].

The integrated technology allows both detectors and sources to be embedded on an optical chip. The integration of sources is already advanced, e.g. a highly-efficient integrated SPDC source in the telecom range has been demonstrated in Ref. [59]. In fact, integrated sources offer better spatial confinement, which enables both high brightness and high heralding efficiency [60]. This is different to bulk SPDC where these two characteristics are usually achieved in different modes [61]. The integration of detectors poses more difficulties. Despite that a couple of works demonstrated the possibility of integrating TES detectors [62, 63] with efficiencies reaching as high as 88%.

There are still challenges to be overcome in the field of integrated quantum photonics. These are coupling losses between disparate elements and between on-chip and off-chip components, waveguide roughness and absorption by the material. Conversely, the complexity of integrated devices, as quantified by the number of interferometers on chip and the number of added active phase and spectral controls, increases really quickly. In fact, it is observed to undergo Moore's law of exponential growth with time [10].

To summarise, state-of-the-art devices enable realistic generation and detection of multiphoton states, and therefore protocols based on multiphoton entanglement can be feasible and should be worth considering.

Chapter 3

Mathematical methods

This chapter explains some mathematical concepts and transformations common in quantum optics that will be used in the subsequent chapters. The aim is to familiarize the Reader with the terminology and provide derivations of some results which will be assumed later.

3.1 Kravchuk polynomials and functions

In this section we will introduce the Kravchuk polynomials and functions since they enable a concise description of some phenomena in quantum optics, as we will see in the later chapters.

Kravchuk polynomials of degree k, $K_k(x;p,N)$ were introduced by Ukrainian mathematician Mikhail Kravchuk as a generalization to the Hermite polynomials [64]. They are defined over a real variable $x \in \mathcal{R}$ and are parametrised by a real positive number p, such that $0 \leq p \leq 1$. A finite number of these polynomials, $N+1$, is known to form an orthogonal set with respect to the binomial distribution [65]. For $N \to \infty$ the Kravchuk polynomials reduce to Hermite polynomials $H_n(x)$ [66].

The Kravchuk polynomials according to Koekoek and Swarttouw [67] are equivalent to Gauss' hypergeometric series [66] which we formally introduce in Subsection 3.1.1

$$K_k(x;p,N) = {}_2F_1(-k,-x;-N;\frac{1}{p}). \tag{3.1}$$

This allows us to define the Kravchuk functions $\phi_k^{(p)}(n-N/2,N)$ in the following way

$$\phi_k^{(p)}(n-N/2,N) = (-1)^k \sqrt{\binom{N}{n}\binom{N}{k} p^{k+n}(1-p)^{N-k-n}} K_k(n;p,N), \tag{3.2}$$

where $k,n = 0,\ldots,N$. These functions satisfy discrete orthonormality and completeness relations

$$\sum_{n=0}^{N} \phi_k^{(p)}(n-n/2,N)\phi_l^{(p)}(n-N/2,N) = \delta_{k,l} \qquad \text{(orthonormality)}, \tag{3.3}$$

$$\sum_{k=0}^{N} \phi_k^{(p)}(n-N/2,N)\phi_k^{(p)}(n'-N/2,N) = \delta_{n,n'} \qquad \text{(completeness)}, \tag{3.4}$$

and thus form a basis of an $(N+1)$-dimensional vector space.

Similarly to the Kravchuk polynomials, the Kravchuk functions can be interpreted as the finite analogues of the continuous Hermite-Gauss functions $H_n(x)\exp(-x^2/2)$ which are familiar from the harmonic oscillator wave functions. This is equivalent to saying that Kravchuk functions are eigenstates of truncated harmonic oscillators.

It has been found that only for $p = 1/2$, the Kravchuk functions have definite parity, that is

$$\phi_k^{(1/2)}(n - N/2, N) = (-1)^k \phi_k^{(1/2)}(N/2 - n, N). \tag{3.5}$$

Therefore, we will focus on this more interesting case of *symmetric* Kravchuk functions and omit p in our notation from now on. The symmetric Kravchuk functions simplify to the following form

$$\phi_k(n - N/2, N) = (-1)^k \sqrt{\frac{1}{2^N}\binom{N}{n}\binom{N}{k}}\, {}_2F_1(-k, -n; -N; 2). \tag{3.6}$$

Inheriting the symmetry of the hypergeometric function with respect to its first two parameters, ${}_2F_1(a, b; c; z) = {}_2F_1(b, a; c; z)$, the Kravchuk function has also the following symmetry

$$\phi_k(n - N/2, N) = (-1)^{n+k} \phi_n(k - N/2, N). \tag{3.7}$$

This property is often referred to as *self-duality* [65].

3.1.1 The Gauss' hypergeometric function

Since the Gauss' hypergeometric function has been mentioned in the previous section, we will just summarise a few definitions here.

As can be found in Ref. [66], the hypergeometric function is defined by the Gauss series

$${}_2F_1[a, b; c; z] = \sum_{n=0}^{\infty} \frac{(a)^n (b)^n}{(c)^n} \frac{z^n}{n!}, \tag{3.8}$$

for $|z| < 1$ and where $(q)^n$ is the rising factorial related to the falling factorial by this simple formula

$$(-q)^n = (-1)^n (q)_n = (-1)^n \binom{q}{n} n!. \tag{3.9}$$

The Gauss series converges to a finite value if at least one of the two arguments a or b is a nonpositive integer. We will consider the case where all three arguments a, b and c are nonpositive, whereby the series reduces to

$$\begin{aligned} {}_2F_1[-a, -b; -c; z] &= \sum_{n=0}^{\infty} \frac{(-a)^n (-b)^n}{(-c)^n} \frac{z^n}{n!} \\ &= \sum_{n=0}^{\min(a,b)} (-z)^n \frac{\binom{a}{n}\binom{b}{n}}{\binom{c}{n}}, \end{aligned} \tag{3.10}$$

as the terms for which $n > a, b$ will not contribute to the sum (they will be zero).

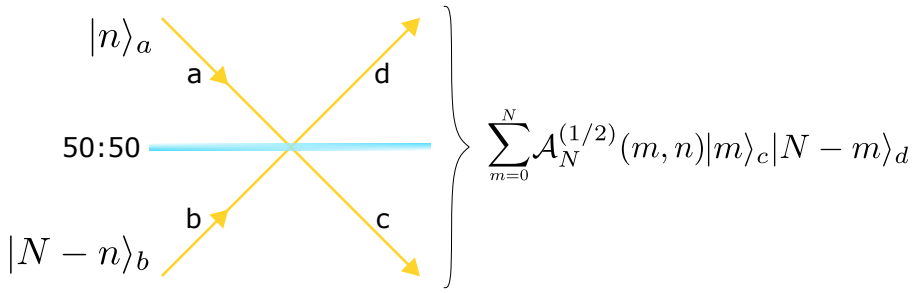

Figure 3.1: A schematic explanation of the operating principle of a (balanced) beam splitter. n and $N-n$ photons enter the beam splitter at the two output modes and an entangled state is created at the output with m and $N-m$ photons exiting with probability amplitude $\mathcal{A}_N^{(1/2)}(m,n)$.

3.2 Quantum optical interferometers

As mentioned in the previous chapter, photons offer many advantages for performing quantum information processing tasks thanks to the ease with which they can be manipulated by simple optical elements. Here, we focus on simple passive linear-optical devices which conserve energy and can thus be described by a unitary transformation of annihilation operators

$$a_m^{\text{out}} = \mathcal{U}_{mn} a_n^{\text{in}}, \tag{3.11}$$

where $\mathcal{U}$ is a unitary matrix, the indices denote a basis of orthogonal modes and the Einstein summation convention is assumed.

Two optical elements which will be used in our two selected protocols in the later chapters, satisfy the above equation. These are the beam splitter and the phase shifter.

3.2.1 The beam splitter

The theory of beam splitters has been develped mostly by Zeilinger [68] and Fearn & Loudon [69]. The beam splitter coherently transforms two input spatial modes a and b into two output spatial modes c and d. Below, we will derive this transformation and show that the probability distribution at the output of a beam splitter can be represented using Kravchuk functions.

We start with the beam splitter Hamiltonian which takes the form:

$$\mathcal{H}_{\text{BS}} = \frac{i}{2}(a^\dagger b e^{-i\varphi} - a b^\dagger e^{i\varphi}), \tag{3.12}$$

where a and b are annihilation operators of the two input modes to the beam splitter, and φ is a phase delay between the transmitted and reflected modes.

The associated unitary to this Hamiltonian is $\mathcal{U}_{\text{BS}} = \exp(-i\mathcal{H}_{\text{BS}}\theta)$, where $\theta = 2\arcsin(\sqrt{r})$ with r the reflectivity of the beam splitter, $0 \leq r \leq 1$.

We will consider the most general case of N photons distributed between the two input modes a and b. Let us assume that n photons are in mode a and therefore $N-n$ photons are in mode b, see Fig. 3.1. The input state can then be written as follows

$$|n\rangle_a|N-n\rangle_b = \frac{(a^\dagger)^n}{\sqrt{n!}} \frac{(b^\dagger)^{N-n}}{\sqrt{(N-n)!}} |0\rangle_a|0\rangle_b. \tag{3.13}$$

In the Heisenberg picture, the operator a evolves according to

$$a(\theta) = \mathcal{U}_{\mathrm{BS}}^{\dagger} a \mathcal{U}_{\mathrm{BS}}. \tag{3.14}$$

which is a solution to the Heisenberg's equation of motion

$$\frac{\mathrm{d}a(\theta)}{\mathrm{d}\theta} = i[\mathcal{H}_{\mathrm{BS}}, a(\theta)]. \tag{3.15}$$

The same equation can be constructed for $b(\theta)$

$$\frac{\mathrm{d}b(\theta)}{\mathrm{d}\theta} = i[\mathcal{H}_{\mathrm{BS}}, b(\theta)]. \tag{3.16}$$

Inserting $\mathcal{H}_{\mathrm{BS}}$ from Eq. (3.12) and using $[a(\theta), a(\theta)^{\dagger}] = [b(\theta), b(\theta)^{\dagger}] = 1$, we obtain

$$\frac{\mathrm{d}a(\theta)}{\mathrm{d}\theta} = \frac{e^{-i\varphi}}{2} b(\theta), \quad \frac{\mathrm{d}b(\theta)}{\mathrm{d}\theta} = -\frac{e^{i\varphi}}{2} a(\theta). \tag{3.17}$$

By taking the second derivative of the above equations we end up with a standard harmonic oscillator equation for both $a(\theta)$ and $b(\theta)$

$$\frac{\mathrm{d}^2 a(\theta)}{\mathrm{d}\theta^2} = -\frac{1}{4} a(\theta), \tag{3.18}$$

$$\frac{\mathrm{d}^2 b(\theta)}{\mathrm{d}\theta^2} = -\frac{1}{4} b(\theta). \tag{3.19}$$

which, assuming the initial conditions $a(0) = a$, $b(0) = b$, has the solutions

$$a(\theta) = a\cos(\tfrac{\theta}{2}) + be^{-i\varphi}\sin(\tfrac{\theta}{2}), \tag{3.20}$$

$$b(\theta) = -ae^{i\varphi}\sin(\tfrac{\theta}{2}) + b\cos(\tfrac{\theta}{2}). \tag{3.21}$$

This can be written in a matrix form where we also rename modes $a(\theta), b(\theta)$ with the output modes c and d, respectively

$$\begin{pmatrix} c \\ d \end{pmatrix} = \begin{pmatrix} \cos(\frac{\theta}{2}) & e^{-i\varphi}\sin(\frac{\theta}{2}) \\ -e^{i\varphi}\sin(\frac{\theta}{2}) & \cos(\frac{\theta}{2}) \end{pmatrix} \begin{pmatrix} a \\ b \end{pmatrix}, \tag{3.22}$$

with the inverse transformation being

$$\begin{pmatrix} a \\ b \end{pmatrix} = \begin{pmatrix} \cos(\frac{\theta}{2}) & -e^{-i\varphi}\sin(\frac{\theta}{2}) \\ e^{i\varphi}\sin(\frac{\theta}{2}) & \cos(\frac{\theta}{2}) \end{pmatrix} \begin{pmatrix} c \\ d \end{pmatrix}. \tag{3.23}$$

In terms of the reflectivity of the beam splitter, this reads

$$\begin{pmatrix} a \\ b \end{pmatrix} = \begin{pmatrix} \sqrt{1-r} & -e^{-i\varphi}\sqrt{r} \\ e^{i\varphi}\sqrt{r} & \sqrt{1-r} \end{pmatrix} \begin{pmatrix} c \\ d \end{pmatrix}. \tag{3.24}$$

It turns out that knowing how a and b evolve, we can evolve a^n or b^n. This is because $\mathcal{U}_{\mathrm{BS}}$ is a unitary operator, $\mathcal{U}_{\mathrm{BS}}\mathcal{U}_{\mathrm{BS}}^{\dagger} = 1$, and therefore

$$\begin{aligned} \mathcal{U}_{\mathrm{BS}}^{\dagger} a^n \mathcal{U}_{\mathrm{BS}} &= \mathcal{U}_{\mathrm{BS}}^{\dagger} a (\mathcal{U}_{\mathrm{BS}}\mathcal{U}_{\mathrm{BS}}^{\dagger}) a (\mathcal{U}_{\mathrm{BS}}\mathcal{U}_{\mathrm{BS}}^{\dagger}) a \ldots (\mathcal{U}_{\mathrm{BS}}\mathcal{U}_{\mathrm{BS}}^{\dagger}) a \mathcal{U}_{\mathrm{BS}} \\ &= (\mathcal{U}_{\mathrm{BS}}^{\dagger} a \mathcal{U}_{\mathrm{BS}}) \ldots (\mathcal{U}_{\mathrm{BS}}^{\dagger} a \mathcal{U}_{\mathrm{BS}}) \\ &= (\mathcal{U}_{\mathrm{BS}}^{\dagger} a \mathcal{U}_{\mathrm{BS}})^n. \end{aligned} \tag{3.25}$$

Let us now substitute the expressions for $a(t)$ and $b(t)$ into Eq. (3.13)

$$|n\rangle_a|N-n\rangle_b = \frac{1}{\sqrt{n!(N-n)!}}\left[\sqrt{1-r}c^\dagger - e^{i\varphi}\sqrt{r}d^\dagger\right]^n\left[e^{-i\varphi}\sqrt{r}c^\dagger + \sqrt{1-r}d^\dagger\right]^{N-n}|0\rangle_a|0\rangle_b. \tag{3.26}$$

Because the operators c and d commute, we can use the binomial theorem $(x+y)^n = \sum_{i=0}^{n}\binom{n}{i}x^i y^{n-i}$ to expand the terms in brackets

$$\begin{aligned}|n\rangle_a|N-n\rangle_b = \frac{1}{\sqrt{n!(N-n)!}}\sum_{p=0}^{n}\binom{n}{p}\left[\sqrt{1-r}c^\dagger\right]^p\left[-e^{i\varphi}\sqrt{r}d^\dagger\right]^{n-p}\\ \times\sum_{q=0}^{N-n}\binom{N-n}{q}\left[e^{-i\varphi}\sqrt{r}c^\dagger\right]^q\left[\sqrt{1-r}d^\dagger\right]^{N-n-q}|0\rangle_a|0\rangle_b.\end{aligned} \tag{3.27}$$

The operators c and d cannot act on the state $|0\rangle_a|0\rangle_b$. It has to be first transformed by the beam splitter operator $\mathcal{U}_{\rm BS}$ into $|0\rangle_c|0\rangle_d$. Let us apply $\mathcal{U}_{\rm BS}$ to the state in Eq. 3.27

$$\begin{aligned}\mathcal{U}_{\rm BS}|n\rangle_a|N-n\rangle_b &= \frac{1}{\sqrt{n!(N-n)!}}\sum_{p=0}^{n}\binom{n}{p}\left[\sqrt{1-r}c^\dagger\right]^p\left[-e^{i\varphi}\sqrt{r}d^\dagger\right]^{n-p}\\ &\quad\times\sum_{q=0}^{N-n}\binom{N-n}{q}\left[e^{-i\varphi}\sqrt{r}c^\dagger\right]^q\left[\sqrt{1-r}d^\dagger\right]^{N-n-q}\mathcal{U}_{\rm BS}|0\rangle_a|0\rangle_b\\ &= \frac{1}{\sqrt{n!(N-n)!}}\sum_{p=0}^{n}\binom{n}{p}\left[\sqrt{1-r}c^\dagger\right]^p\left[-e^{i\varphi}\sqrt{r}d^\dagger\right]^{n-p}\\ &\quad\times\sum_{q=0}^{N-n}\binom{N-n}{q}\left[e^{-i\varphi}\sqrt{r}c^\dagger\right]^q\left[\sqrt{1-r}d^\dagger\right]^{N-n-q}|0\rangle_c|0\rangle_d\\ &= \frac{1}{\sqrt{n!(N-n)!}}(-1)^n e^{in\varphi}\sqrt{r^n(1-r)^{N-n}}\\ &\quad\times\sum_{p=0}^{n}\sum_{q=0}^{N-n}\binom{n}{p}\binom{N-n}{q}(-1)^p e^{-i\varphi(p+q)}\sqrt{\left(\tfrac{1-r}{r}\right)^{p-q}(p+q)!(N-p-q)!}\\ &\quad\times|p+q\rangle_c|N-p-q\rangle_d.\end{aligned} \tag{3.28}$$

We replace the sum for q with $k = p+q$

$$\sum_{p=0}^{n}\sum_{q=0}^{N-n}\binom{n}{p}\binom{N-n}{q}\cdots = \sum_{p=0}^{n}\sum_{k=p}^{N-n+p}\binom{n}{p}\binom{N-n}{k-p}\cdots \tag{3.29}$$

We notice the second term is zero when $k < p$. Therefore, the lower limit can be safely extended to $k = 0$. We also note that $p \le n$, and thus $N-n+p \le N$. When k is above this limit, $k-p > N-n$ and the second term is zero, so we can increase the upper limit to $k = N$. This allows us to change the order of the summations as the second sum no

longer depends on p

$$\mathcal{U}_{\mathrm{BS}}|n\rangle_a|N-n\rangle_b = \frac{1}{\sqrt{n!(N-n)!}}(-1)^n e^{in\varphi}\sqrt{r^n(1-r)^{N-n}} \times \sum_{k=0}^{N}\sum_{p=0}^{n}\binom{n}{p}\binom{N-n}{k-p}(-1)^p e^{-ik\varphi}\sqrt{\left(\tfrac{1-r}{r}\right)^{2p-k}k!(N-k)!}|k\rangle_c|N-k\rangle_d. \tag{3.30}$$

The amplitude of detecting $m, N-m$ photons behind the beam splitter is then

$$\begin{aligned}
\mathcal{A}_N^{(r)}(m,n) &= \langle m|_c\langle N-m|_d\,\mathcal{U}_{\mathrm{BS}}|n\rangle_c|N-n\rangle_d \\
&= \frac{1}{\sqrt{n!(N-n)!}}(-1)^n e^{in\varphi}\sqrt{r^n(1-r)^{N-n}} \\
&\quad\times\sum_{k=0}^{N}\sum_{p=0}^{n}\binom{n}{p}\binom{N-n}{k-p}(-1)^p e^{-ik\varphi}\sqrt{\left(\tfrac{1-r}{r}\right)^{2p-k}k!(N-k)!}\,\delta_{m,k} \\
&= \frac{1}{\sqrt{n!(N-n)!}}(-1)^n e^{in\varphi}\sqrt{r^n(1-r)^{N-n}} \\
&\quad\times\sum_{p=0}^{n}\binom{n}{p}\binom{N-n}{m-p}(-1)^p e^{-im\varphi}\sqrt{\left(\tfrac{1-r}{r}\right)^{2p-m}m!(N-m)!} \\
&= (-1)^n e^{i(n-m)\varphi}\sqrt{\frac{\binom{N}{n}}{\binom{N}{m}}r^{n+m}(1-r)^{N-n-m}}\sum_{p=0}^{n}\binom{n}{p}\binom{N-n}{m-p}\left(1-\tfrac{1}{r}\right)^p.
\end{aligned} \tag{3.31}$$

We can now apply the formalism we have developed in section 3.1 to simplify the formula for the beam splitter amplitude even further. Let us consider the last sum in Eq. 3.31, which we label Σ. The term $\left(1-\frac{1}{r}\right)^p$ can be expanded using the binomial theorem

$$\left(1-\tfrac{1}{r}\right)^p = \sum_{i=0}^{p}\binom{p}{i}\left(-\frac{1}{r}\right)^i, \tag{3.32}$$

so that the sum looks like

$$\Sigma = \sum_{p=0}^{n}\binom{n}{p}\binom{N-n}{m-p}\sum_{i=0}^{p}\binom{p}{i}\left(-\frac{1}{r}\right)^i. \tag{3.33}$$

We notice that when $p \geq m$, $\binom{N-n}{m-p}$ is zero and when $i \geq p$, the binomial $\binom{p}{i}$ is also zero. Also $n \geq p$, or the first binomial would be zero. These allow us to extend the limits in the second summation to $p = m$ and to increase the upper and lower limits in the first summation to $m \in \langle i, m\rangle$, as the terms which are zero will not contribute to the sum. With this trick it becomes possible to swap the order of the summations

$$\Sigma = \sum_{i=0}^{m}\left(-\frac{1}{r}\right)^i\sum_{p=i}^{m}\binom{n}{p}\binom{N-n}{m-p}\binom{p}{i}. \tag{3.34}$$

Another term can be taken out of the second summation by using the identity $\binom{n}{p}\binom{p}{i} = \binom{n}{i}\binom{n-i}{p-i}$

$$\Sigma = \sum_{i=0}^{m}\left(-\frac{1}{r}\right)^i\binom{n}{i}\sum_{p=i}^{m}\binom{N-n}{m-p}\binom{n-i}{p-i}. \tag{3.35}$$

Relabelling next the summation index $p \to m - p$

$$\Sigma = \sum_{i=0}^{m} \Big(-\frac{1}{r}\Big)^i \binom{n}{i} \sum_{p=0}^{m-i} \binom{N-n}{p} \binom{n-i}{m-p-i}. \tag{3.36}$$

The summation can now be evaluated by the Chu-Vandermonde identity [70] $\sum_{b=0}^{d} \binom{a}{b}\binom{c-a}{d-b} = \binom{c}{d}$, where $a = N - n, b = p, c = N - i$ and $d = m - i$, wherupon it simplifies to

$$\Sigma = \sum_{i=0}^{m} \Big(-\frac{1}{r}\Big)^i \binom{n}{i} \binom{N-i}{m-i}. \tag{3.37}$$

Finally, we note that $\binom{N-i}{m-i} = \frac{\binom{N}{m}\binom{m}{i}}{\binom{N}{i}}$ which takes us to

$$\begin{aligned} \Sigma &= \binom{N}{m} \sum_{i=0}^{m} \Big(-\frac{1}{r}\Big)^i \frac{\binom{n}{i}\binom{m}{i}}{\binom{N}{i}} \\ &= \binom{N}{m} {}_2F_1[-n, -m; -N; \tfrac{1}{r}]. \end{aligned} \tag{3.38}$$

where we recognised the formula for the hypergeometric function derived in Eq. 3.10.

Substituting Eq. 3.38 into Eq. 3.31, we obtain

$$\mathcal{A}_N^{(r)}(m,n) = (-1)^n e^{i(n-m)\varphi} \sqrt{\binom{N}{n}\binom{N}{m} r^{n+m}(1-r)^{N-n-m}} \, {}_2F_1[-n, -m; -N; \tfrac{1}{r}]. \tag{3.39}$$

For $r = 1/2$ we recover Eq. 3.6

$$\begin{aligned} \mathcal{A}_N^{(1/2)}(m,n) &= (-1)^n e^{i(n-m)\varphi} \sqrt{\frac{1}{2^N}\binom{N}{n}\binom{N}{m}} \, {}_2F_1[-n, -m; -N; 2] \\ &= e^{i(n-m)\varphi} \phi_n(m - \tfrac{N}{2}, N). \end{aligned} \tag{3.40}$$

This way we have shown that for a 50:50 beam splitter the probability amplitude $\mathcal{A}_N^{(1/2)}(m,n)$ can be expressed in terms of the Kravchuk function $\phi_n(m - \frac{N}{2}, N)$, where N is the total number of photons (which is conserved), $n, N - n$ are the numbers of photons input to the beam splitter and $m, N - m$ are the numbers output from the beam splitter (see also Fig. 3.1).

3.2.2 Hong-Ou-Mandel interference

As a simple example of the beam splitter transformation we will consider two photons injected simultaneously to the two input ports of a 50:50 beam splitter. The incident state is $|1\rangle_a|1\rangle_b$ and upon the beam splitter transformation it becomes

$$|1\rangle_a|1\rangle_b \xrightarrow{\text{BS}} \mathcal{A}_2^{(1/2)}(0,1)|0\rangle_c|2\rangle_d + \mathcal{A}_2^{(1/2)}(1,1)|1\rangle_c|1\rangle_d + \mathcal{A}_2^{(1/2)}(2,1)|2\rangle_c|0\rangle_d, \tag{3.41}$$

where $\mathcal{A}_2^{(1/2)}(m,n)$ is defined in Eq. 3.40. Table 3.1 shows the values for the amplitudes for each term in Eq. 3.41 assuming the reflected photons acquire a phase shift of $\varphi = -\frac{\pi}{2}$. The resulting state is thus

$$|\Psi_{\text{BS}}\rangle = \frac{i}{\sqrt{2}}(|0\rangle_c|2\rangle_d + |2\rangle_c|0\rangle_d). \tag{3.42}$$

m	$\mathcal{A}_2^{(1/2)}(m,1)$
0	$\frac{i}{\sqrt{2}}$
1	0
2	$\frac{i}{\sqrt{2}}$

Table 3.1: Probability amplitudes for a $N = 2$ photon state and $\varphi = -\frac{\pi}{2}$.

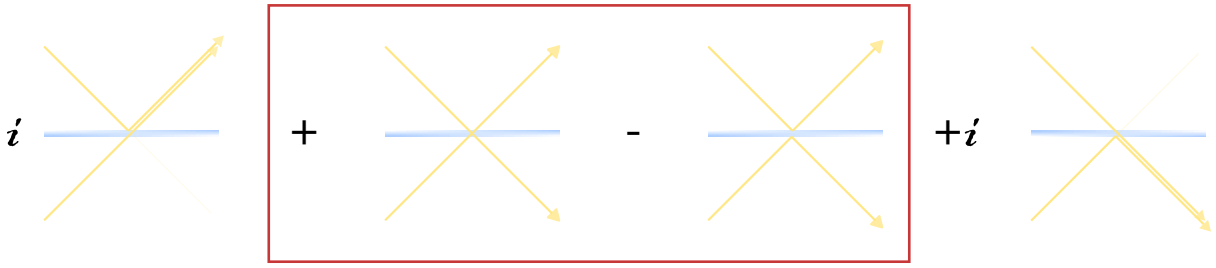

Figure 3.2: When two photons meet at the beam splitter there are four possible outcomes of how they emerge. However, if the photons are indistinguishable, the processes where both photons are reflected or both are transmitted (marked by the red box) interfere destructively. As a result both photons always leave the beam splitter together.

Apparently, the two photons always emerge together in the same output port. This effect is in fact a result of the destructive interference of the two processes where either both photons are transmitted or both are reflected. Fig. 3.2 demonstrates this effect graphically. The photons must, however, be indistinguishable in all of their degrees of freedom for this to happen. An experimental demonstration of this effect is famously known as the Hong-Ou-Mandel (HOM) effect [71].

In the original HOM experiment, the time separation between the two photons striking a beam splitter was measured. The position of the beam splitter would be changed causing a slight time delay between the times the photons fell onto the beam splitter. Time resolving measurements reveal that the photons reflect or transmit independently of each other causing the detectors which stand behind the beam splitter to click within a short time of each other. A coincidence between the two output ports could then be observed with rate [49]

$$R_{\text{coin}} \sim \left[1 - e^{-\left(\frac{\tau_a - \tau_b}{\tau_{\text{corr}}}\right)^2}\right], \tag{3.43}$$

where $c\tau_a$ and $c\tau_b$ are the distances the two photons travel from the source to the beam splitter and τ_{corr} is the correlation time between the two photons. The data from the original paper [71] is shown in Fig. 3.3 . As we can see, for $\tau_a - \tau_b = 0$ we have $R_{\text{coin}} = 0$, while for $|\tau_a - \tau_b| \gg \tau_{\text{corr}}$, R_{coin} rises to a maximum.

In summary, when the photons arrived at the beam splitter simultaneously or within a time shorter than the correlation time (which is on the order of a few nanoseconds for photons), no coincident counts were observed and the coincidence rate made a characteristic 'dip', now known as the HOM dip. It should be stressed that the origin of the interference is the temporal indistinguishability of the two photons rather than the fact that the photons arrive at the beam splitter at the same time, as has been demonstrated in Ref. [72]. Thus, by reproducing the HOM interference effect an experimentalist can estimate the degree of indistinguishability of their photons.

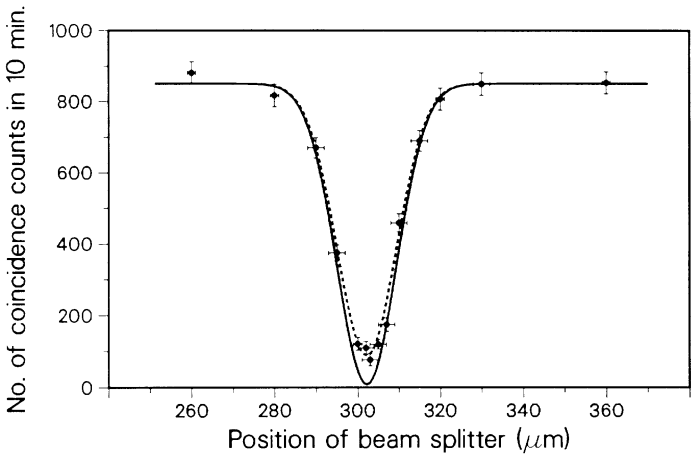

Figure 3.3: Data taken from Ref. [71]. The measured number of coincidences as a function of the beam splitter displacement $c(\tau_a - \tau_b)$. The count does not go to zero exactly for the experimental data as the beams cannot overlap perfectly at the beam splitter.

3.2.3 Multiphoton HOM

Generalizing the two-photon interference on a beam splitter to multi-photon states, we observe a similar behaviour - it turns out that when equal numbers of photons enter the beam splitter at each port, all odd-photon-number components disappear at the output. In quantum metrology, such output from the beam splitter is called the Holland-Burnett state [73].

Let us consider a general N-photon state, $|n\rangle_a|N-n\rangle_b$, entering the beam splitter

$$|n\rangle_a|N-n\rangle_b \xrightarrow{\text{BS}} \sum_{m=0}^{N} \mathcal{A}_N^{(1/2)}(m,n)|m\rangle_c|N-m\rangle_d. \tag{3.44}$$

Fig. 3.4 and 3.5 depict photon number distributions $|\mathcal{A}_N^{(1/2)}(m,n)|^2$ for $N=4$ and $N=10$, respectively. We observe that indeed for $n=2$ and $n=5$, respectively, the output states are missing odd-photon-number components and live in a reduced Hilbert space of dimension $\frac{N}{2}$. This will have implications on the amount of entanglement and achievable quantum Fisher information available through these states, as will be explained in subsequent chapters.

Looking at Eq. 3.42 and 3.44 we observe quantum correlations between the two output modes to the beam splitter. The state in Eq. 3.42 in particular is a 2-photon N00N state which is a maximally entangled state [74, 75]. Thus the beam splitter is an entangling device for Fock state inputs and plays a crucial role in creating and manipulating various multiphoton entangled states [2].

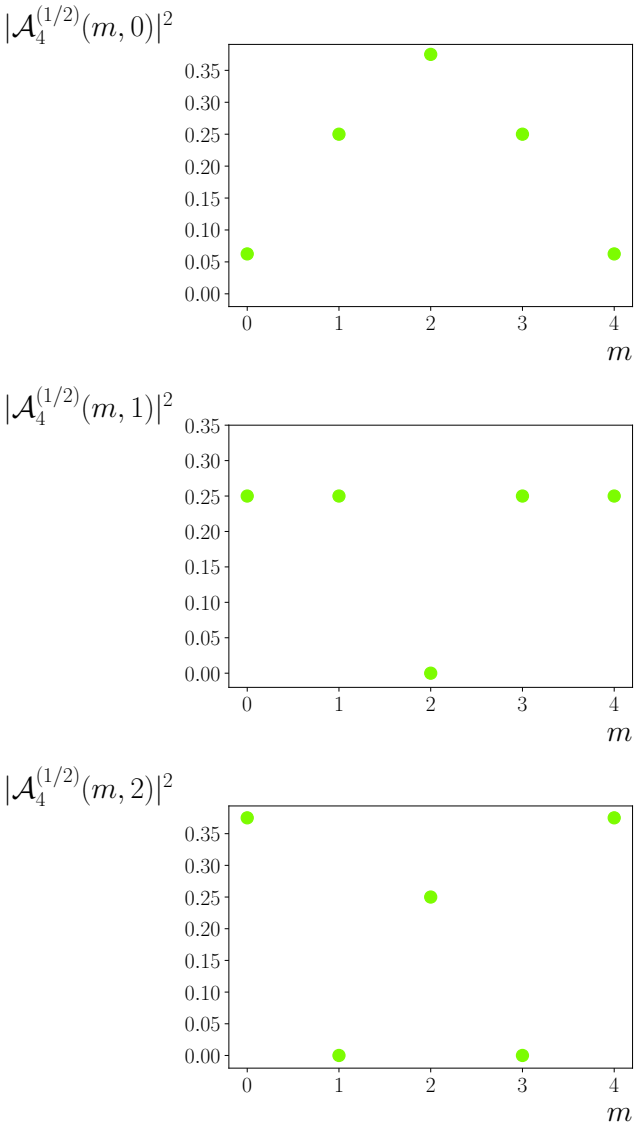

Figure 3.4: Photon number distributions $|\mathcal{A}_N(m,n)|^2$ computed for $N = 4$ and $m = 0, 1, 2$. Note that according to Eq. 3.5, $|\mathcal{A}_N(m,n)|^2 = |\mathcal{A}_N(N-m,n)|^2$.

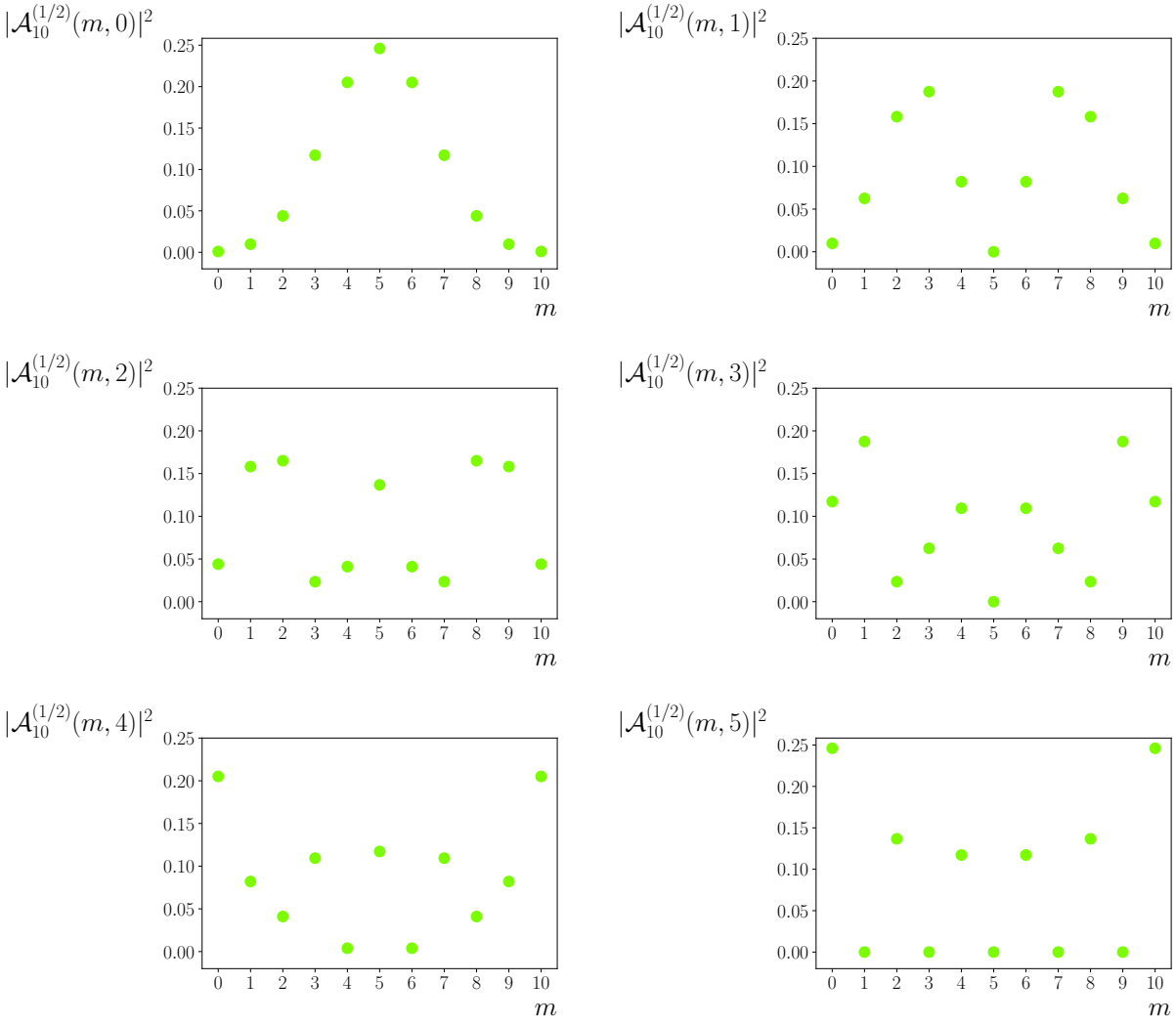

Figure 3.5: Photon number distributions $|\mathcal{A}_N(m,n)|^2$ computed for $N = 10$ and $m = 0,\ldots,5$. Note that according to Eq. 3.5, $|\mathcal{A}_N(m,n)|^2 = |\mathcal{A}_N(N-m,n)|^2$.

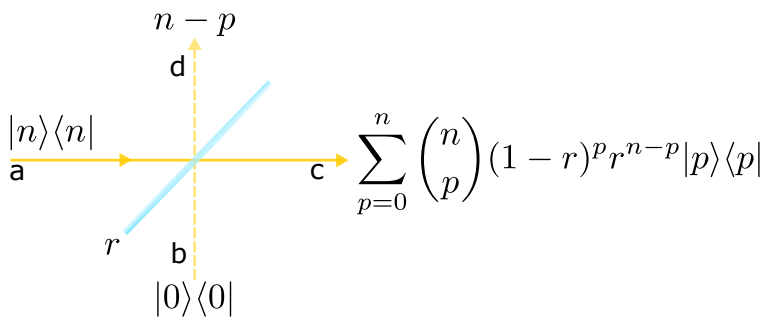

Figure 3.6: Losses are modelled by inserting a beam splitter of reflectivity r into the pathway of the photons. Photons in mode a are assumed to interfere with vacuum in mode b. The reflected photons in mode d are traced out and photons in mode c represent the transmitted mode with a reduced number of photons which follows a Bernoulli transformation.

3.2.4 Modelling losses

A beam splitter can also be useful in modelling photon losses. In many quantum photonic scenarios, one must consider the effect of photon losses in order to realistically model the behaviour of a new system. These losses can be modelled well by inserting a beam splitter into the pathway of the photons, where the reflectivity r of the beam splitter quantifies the amount of losses. The reflected mode can then be traced out and the transmitted mode with a reduced number of photons is left, see Fig. 3.6. Below, we shall calculate how the probability of finding a certain number of photons in a given mode is modified. We modify Eq. 3.30 so that n photons travel in mode a and 0 photons are present in mode b

$$\mathcal{U}_{\mathrm{BS}}|n\rangle_a|0\rangle_b = \frac{1}{\sqrt{n!}}(-1)^n e^{in\varphi}\sqrt{r^n}\sum_{p=0}^{n}\binom{n}{p}(-1)^p e^{-ip\varphi}\sqrt{\left(\frac{1-r}{r}\right)^p p!(n-p)!}|p\rangle_c|n-p\rangle_d. \tag{3.45}$$

The resulting density matrix is then

$$\begin{aligned}\mathcal{U}_{\mathrm{BS}}|n,0\rangle\langle n,0|\mathcal{U}_{\mathrm{BS}}^\dagger = {}& \frac{1}{\sqrt{n!}}(-1)^n e^{in\varphi}\sqrt{r^n}\sum_{p=0}^{n}\binom{n}{p}(-1)^p e^{-ip\varphi}\sqrt{\left(\frac{1-r}{r}\right)^p p!(n-p)!}\\ &\times\frac{1}{\sqrt{n!}}(-1)^n e^{-in\varphi}\sqrt{r^n}\sum_{q=0}^{n}\binom{n}{q}(-1)^q e^{iq\varphi}\sqrt{\left(\frac{1-r}{r}\right)^q q!(n-q)!}\\ &\times|p,n-p\rangle\langle q,n-q|\\ ={}&\frac{1}{n!}r^n\sum_{p=0}^{n}\sum_{q=0}^{n}\binom{n}{p}\binom{n}{q}(-1)^{p+q}e^{-i(p-q)\varphi}\sqrt{\left(\tfrac{1-r}{r}\right)^{p+q}p!q!(n-p)!(n-q)!}\\ &\times|p,n-p\rangle\langle q,n-q|.\end{aligned} \tag{3.46}$$

Tracing over the reflected mode d, we find that $p=q$ and hence

$$\mathrm{Tr}_d\left\{\mathcal{U}_{\mathrm{BS}}|n,0\rangle\langle n,0|\mathcal{U}_{\mathrm{BS}}^\dagger\right\} = \sum_{p=0}^{n}\binom{n}{p}(1-r)^p r^{n-p}|p\rangle\langle p|, \tag{3.47}$$

which is the final expression for a mode suffering from transmission losses of size r. This kind of transformation is known in the literautre as the Bernoulli transformation [76, 77].

The density matrix formalism is essential as losses reduce the purity of a quantum state and states become mixed.

3.2.5 The Mach-Zehnder interferometer

From two 50:50 beam spitters and another passive linear-optical device - the phase shifter - one can build a Mach-Zehnder interferometer. The phase shifter may be represented by a unitary operator $e^{i\hat{n}\theta}$, where $\hat{n}$ is the photon number operator and θ is the relative phase shift between the two interferometer arms. This is a useful interferometer as it can replace a universal tunable beam splitter, which will be shown below. The variable reflectivity r is governed by the relative phase shift θ applied by the phase sensitive element, $\theta = 2\arcsin(\sqrt{r})$. See Fig. 3.7 for a schematic diagram of the Mach-Zehnder interferometer.

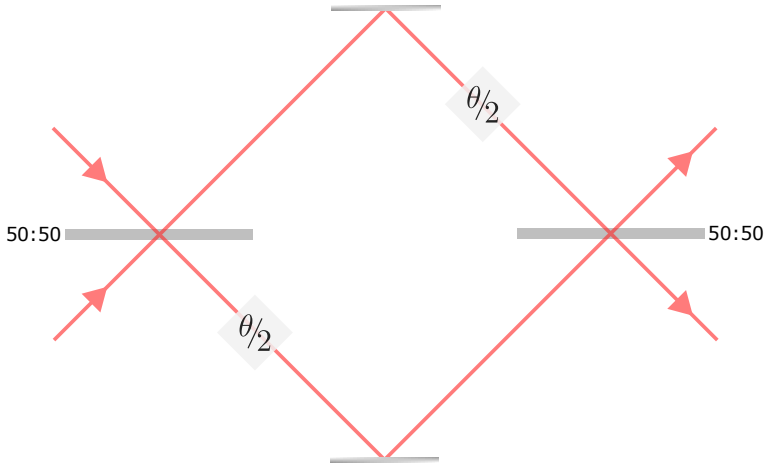

Figure 3.7: The Mach-Zehnder interferometer consists of two balanced beam splitters and phase shifters which apply a relative phase shift θ between the two arms. This setup can replace a universal tunable beam splitter with reflectivity $r = \sin^2(\frac{\theta}{2})$.

For a 50:50 beam splitter, the transformation matrix in Eq. 3.24 takes the following form

$$\mathcal{U}_{\mathrm{BS}}^{(r=1/2)} = \begin{pmatrix} \frac{1}{\sqrt{2}} & -\frac{e^{-i\varphi}}{\sqrt{2}} \\ \frac{e^{i\varphi}}{\sqrt{2}} & \frac{1}{\sqrt{2}} \end{pmatrix}, \tag{3.48}$$

and the unitary operator for the phase shifter can be represented as

$$\mathcal{U}_{\theta} = \begin{pmatrix} e^{i\theta/2} & 0 \\ 0 & e^{-i\theta/2} \end{pmatrix}. \tag{3.49}$$

Then, the unitary operator for the Mach-Zehnder interferometer takes the form

$$\mathcal{U}_{\mathrm{MZI}} = \mathcal{U}_{\mathrm{BS}}\,\mathcal{U}_{\theta}\,\mathcal{U}_{\mathrm{BS}}^{\dagger} \tag{3.50}$$

$$= \begin{pmatrix} \frac{1}{\sqrt{2}} & -\frac{e^{-i\varphi}}{\sqrt{2}} \\ \frac{e^{i\varphi}}{\sqrt{2}} & \frac{1}{\sqrt{2}} \end{pmatrix} \begin{pmatrix} e^{i\theta/2} & 0 \\ 0 & e^{-i\theta/2} \end{pmatrix} \begin{pmatrix} \frac{1}{\sqrt{2}} & \frac{e^{-i\varphi}}{\sqrt{2}} \\ -\frac{e^{i\varphi}}{\sqrt{2}} & \frac{1}{\sqrt{2}} \end{pmatrix} \tag{3.51}$$

$$= \begin{pmatrix} \cos(\frac{\theta}{2}) & ie^{-i\varphi}\sin(\frac{\theta}{2}) \\ ie^{i\varphi}\sin(\frac{\theta}{2}) & \cos(\frac{\theta}{2}) \end{pmatrix}, \tag{3.52}$$

which is just a rotated version of the matrix in Eq. 3.23 representing a beam splitter operation with reflectivity $r = \sin^2(\frac{\theta}{2})$.

Chapter 4

Entanglement distribution

Having introduced all the necessary tools in the previous chapter, we procede to demonstrate the applications of multi-photon bipartite entangled states. In this chapter we will explain how multi-photon entanglement can be distributed in a way that is resource-efficient and well-matched with the hardware of quantum photonics and, in addition, offers quadratic improvement in scaling with distance compared to schemes based on Bell pairs. Our analysis focuses in particular on scenarios which could be useful in quantum communications.

4.1 State of the art

Quantum communications is a field which looks into different ways of transferring quantum states from one place to another [5] in order to send information much more efficiently than permitted by classical communication channels. This advantage is possible by using entanglement which provides non-local correlations between different parties. The challenge, however, is to extend the distance between the communicating locations to a global scale despite losses in the transmitting channels which spoil entanglement. The classical solution of simply amplifying the signal is impossible for quantum signals due to the no-cloning theorem [78] and alternative remedies need to be found. A popular option is to use quantum repeaters [79] but the disadvantage of this approach is the necessity of numerous intermediate stations, quantum memories and multiple two-photon Bell pairs, a resource that is often created non-deterministically. Despite rapid advances in the field [80, 81, 82, 83, 84, 85, 86, 87, 88, 89], experimental realizations of quantum repeaters currently show deterioration with distance which is insufficient for most quantum communications applications [90].

Another possibility for global quantum communications is to use satellites to distribute two-photon Bell pairs, which is advantageous thanks to photons travelling the majority of the distance in free space and thus experiencing less loss than in atmospheric links or optical fibres, while connecting arbitrarily distant locations. This approach has also seen much progress recently [91, 92, 93, 94, 95, 96, 97, 98, 99, 100, 101, 90, 102, 103]. Still, losses continue to be detrimental, with typically only approximately 1 in 10^6 of produced Bell pairs surviving the trip and being detected on the ground [97].

From the discussion above, we observe that the majority of the research effort to date concentrated on the distribution of two-photon Bell pairs. In this chapter, we want to bring multi-photon entanglement back into the spotlight and present it as a competitor to the single-photon technology.

4.2 Proposal for the entanglement distribution protocol

We propose a protocol that uses multi-photon bipartite entanglement and photon-number-resolving (PNR) detectors to establish long-distance near-maximal entanglement distribution. We show that it is robust to high transmission losses which, remarkably, deteriorate only its efficiency, but not the amount of generated entanglement, a feature until now seen only in protocols based on Bell pairs. The protocol has the potential to outperform other methods of entanglement distribution which have transmission rates scaling as $O(\eta)$, where η is the channel transmittance. This is particularly true in high loss scenarios, for example satellite-based Earth-space channels and long fibre networks.

The protocol, shown schematically in Fig. 4.1, starts with Alice and Bob holding an SPDC source each. The source generates one copy of the TMSV state, as given in Eq. (2.18), so that the total input state is

$$\begin{aligned} |\Psi_{\text{in}}\rangle &= |\Psi_{\text{TMSV}}\rangle^{\otimes 2} \\ &= \sum_{n,n'=0}^{\infty} \sqrt{\lambda_n \lambda_{n'}} |n\rangle_{a_1} |n\rangle_{a_2} \otimes |n'\rangle_{b_1} |n'\rangle_{b_2}. \end{aligned} \tag{4.1}$$

The idler beams from each TMSV state, which we call a_2 and b_2 for Alice and Bob respectively, are sent to Charlie at a distant location. Charlie interferes the two incoming beams on a balanced $(50:50)$ beam splitter and then detects them with PNR detectors. Since initially modes a_1 and a_2, and b_1 and b_2 are entangled, and the beam splitter is an entangling device as we discussed in Section 3.2.3, the signal modes a_1 and b_1 become entangled after the measurement.

Assuming for the time being there are no losses in any of the modes, we infer that detection of σ photons in total in the entangling measurement means that σ photons were distributed between the two idler beams entering the BS and thus that the total number of photons, S, in the output state shared by Alice and Bob is $S = \sigma$. From Eq. (3.40), the probability amplitude of detecting k and $\sigma - k$ photons behind the beam splitter is equal to

$$\begin{aligned} \mathcal{A}_{\sigma}^{(1/2)}(k,n) &= \langle k|_{a_2} \langle \sigma - k|_{b_2} \, \mathcal{U}_{\text{BS}} |n\rangle_{a_2} |\sigma - n\rangle_{b_2} \\ &= e^{i(n-k)\varphi} \phi_n(k - \tfrac{\sigma}{2}, \sigma), \end{aligned} \tag{4.2}$$

which for $\varphi = -\frac{\pi}{2}$ becomes

$$\mathcal{A}_{\sigma}^{(1/2)}(k,n) = i^{k-n} \phi_n(k - \tfrac{\sigma}{2}, \sigma). \tag{4.3}$$

The output state in our protocol is therefore

$$\begin{aligned} |\Psi_{\text{out}}^{(k,\sigma)}\rangle &= \mathcal{N} \langle k, \sigma - k | \mathcal{U}_{\text{BS}} | \Psi_{\text{TMSV}} \rangle^{\otimes 2} \\ &= \mathcal{N} \sum_{n,n'=0}^{\infty} \sqrt{\lambda_n \lambda_{n'}} |n, n'\rangle_{a_1,b_1} \langle k, \sigma - k | \mathcal{U}_{\text{BS}} | n, m \rangle_{a_2,b_2}, \end{aligned} \tag{4.4}$$

where $\mathcal{N}$ is the normalization. Since $n + n' = \sigma$ must hold true, the sum over n' is redundant and the summation over n becomes upper bounded

$$|\Psi_{\text{out}}^{(k,\sigma)}\rangle = \sum_{n=0}^{\sigma} \mathcal{A}_{\sigma}(k,n) \, |n, \sigma - n\rangle_{a_1,b_1} . \tag{4.5}$$

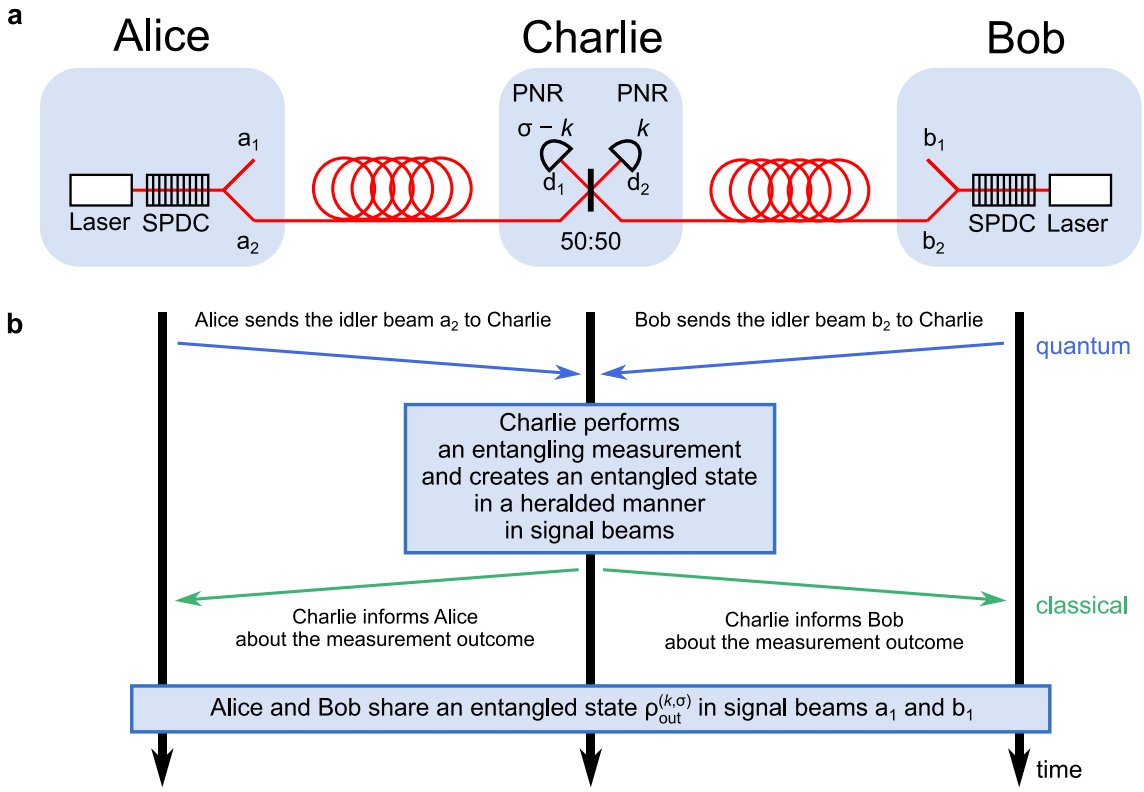

Figure 4.1: Distribution of multi-photon bipartite entanglement. An explanation of the protocol as shown by **a)** a schematic of the setup and **b)** a sequence diagram. Alice and Bob locally generate a photon-number entangled two-mode squeezed vacuum state each, obtained by spontaneous parametric down-conversion (SPDC) – the most ubiquitous source of quantum light. They send their idler modes a_2 and b_2 to a remote station Charlie, who interferes them on a 50:50 beam splitter (BS) and performs a photon-number-resolving (PNR) detection on the BS output modes d_1 and d_2. This is an entangling measurement by which Charlie creates the heralded mixed state $\rho_{\text{out}}^{(k,\sigma)}$ (or, in the lossless case, the pure state $|\Psi_{\text{out}}^{(k,S=\sigma)}\rangle$) in Alice and Bob's signal modes a_1 and b_1. The state and the amount of shared entanglement is parametrised by the outcomes of Charlie's measurement, k and $\sigma - k$. In general, this entanglement is multi-photon, with $S \geq \sigma$ ($S = \sigma$ for a pure state) photons in total distributed between Alice and Bob. After Charlie informs the parties classically of the measurement outcome, Alice and Bob know which state $\rho_{\text{out}}^{(k,\sigma)}$ they possess and may employ it for quantum applications.

In the above formula, we have dropped the (1/2) superscript for better clarity as we will only use this notation for 50:50 beam splitters. We now see that $|\Psi_{\text{out}}^{(k,\sigma)}\rangle$ lives in a Hilbert space of dimension $(\sigma+1)$ and is parametrized by the entangling measurement readouts k and $\sigma-k$ which define its photon number statistics. The probability of detecting n photons in mode a_1 (and $\sigma-n$ in mode b_1) is $|\mathcal{A}_\sigma(k,n)|^2 = |\phi_k(n-\frac{\sigma}{2},\sigma)|^2$. Example photon number distributions of this form were given earlier in Section 3.2.3.

It is worth noting that this protocol can also be realised in a delayed-choice scheme. Then, the measurements taken by Alice and Bob on the signal modes a_1 and b_1 precede the ones performed on the idler modes a_2 and b_2 at the remote station. By the no-signalling principle [104], the photon-number statistics observed by Alice and Bob are again determined by $|\mathcal{A}_\sigma(k,n)|^2$.

4.2.1 Entanglement measure: logarithmic negativity

To quantify the amount of entanglement in the output state of the protocol we take the logarithmic negativity of the state $|\Psi_{\text{out}}^{(k,\sigma)}\rangle$. We chose this entanglement measure because it is easily computable and gives an upper bound to the distillable entanglement, which reflects the maximal number of Bell states that can be extracted [105, 106, 107]. For a state given by the density operator, here $\rho = |\Psi_{\text{out}}^{(k,\sigma)}\rangle\langle\Psi_{\text{out}}^{(k,\sigma)}|$, the logarithmic negativity is defined as

$$E_{\mathcal{N}} = \log_2||\rho^\Gamma||_1, \tag{4.6}$$

where Γ denotes the partial transpose operation and $||\rho^\Gamma||_1$ is the trace norm of ρ^Γ. The density matrix and its partial transform after inserting Eq. (4.5) are given by

$$\begin{aligned}
\rho_{\text{out}}^{(k,\sigma)} &= \sum_{n,m=0}^{\sigma} \mathcal{A}_\sigma(k,n)\mathcal{A}_\sigma^*(k,m)\,|n,\sigma-n\rangle\langle m,\sigma-m|\,, \\
\left(\rho_{\text{out}}^{(k,\sigma)}\right)^{\Gamma_2} &= \sum_{n,m=0}^{\sigma} \mathcal{A}_\sigma(k,n)\mathcal{A}_\sigma^*(k,m)\,|n,\sigma-m\rangle\langle m,\sigma-n|\,.
\end{aligned} \tag{4.7}$$

To find the trace norm, defined as $||\rho||_1 = \text{Tr}\sqrt{\rho^\dagger\rho}$, we first need to find

$$\begin{aligned}
\left(\left(\rho_{\text{out}}^{(k,\sigma)}\right)^{\Gamma_2}\right)^\dagger \cdot \left(\rho_{\text{out}}^{(k,\sigma)}\right)^{\Gamma_2} &= \sum_{n,m=0}^{\sigma} \mathcal{A}_\sigma^*(k,n)\mathcal{A}_\sigma(k,m)\,|m,\sigma-n\rangle\langle n,\sigma-m| \\
&\quad \otimes \sum_{n',m'=0}^{\sigma} \mathcal{A}_\sigma(k,n')\mathcal{A}_\sigma^*(k,m')\,|n',\sigma-m'\rangle\langle m',\sigma-n'| \\
&= \sum_{n,n',m,m'=0}^{\sigma} \delta_{mm'}\delta_{nn'}\mathcal{A}_\sigma^*(k,n)\mathcal{A}_\sigma(k,m)\mathcal{A}_\sigma(k,n')\mathcal{A}_\sigma^*(k,m') \\
&\quad \times |m,\sigma-n\rangle\langle m',\sigma-n'| \\
&= \sum_{n,m=0}^{\sigma} \left|\mathcal{A}_\sigma(k,n)\right|^2\left|\mathcal{A}_\sigma(k,m)\right|^2 |m,\sigma-n\rangle\langle m,\sigma-n| \\
&= \left(\sum_{m=0}^{\sigma}\left|\mathcal{A}_\sigma(k,m)\right|^2 |m\rangle\langle m|\right) \otimes \left(\sum_{n=0}^{\sigma}\left|\mathcal{A}_\sigma(k,n)\right|^2 |\sigma-n\rangle\langle\sigma-n|\right),
\end{aligned}$$

where in the second step δ_{ij} denotes the Kronecker delta equal to 1 for $i = j$ and 0 otherwise. The operator $\left(\left(\rho_{\text{out}}^{(k,\sigma)}\right)^{\Gamma_2}\right)^{\dagger} \cdot \left(\rho_{\text{out}}^{(k,\sigma)}\right)^{\Gamma_2}$ is diagonal and therefore, taking its square root will be equivalent to taking the square root of its eigenvalues

$$\sqrt{\left(\left(\rho_{\text{out}}^{(k,\sigma)}\right)^{\Gamma_2}\right)^{\dagger} \cdot \left(\rho_{\text{out}}^{(k,\sigma)}\right)^{\Gamma_2}} = \left(\sum_{m=0}^{\sigma} \left|\mathcal{A}_\sigma(k,m)\right| |m\rangle\langle m|\right) \otimes \left(\sum_{n=0}^{\sigma} \left|\mathcal{A}_\sigma(k,n)\right| |\sigma-n\rangle\langle\sigma-n\right).$$

It remains to calculate the trace of the expression above

$$\begin{aligned}\left\|\left(\rho_{\text{out}}^{(k,\sigma)}\right)^{\Gamma_2}\right\|_1 &= \sum_{a,b=0}^{\sigma} \left(\sum_{m=0}^{\sigma} \left|\mathcal{A}_\sigma(k,m)\right| \langle a|m\rangle \langle m|a\rangle\right) \left(\sum_{n=0}^{\sigma} \left|\mathcal{A}_\sigma(k,n)\right| \langle b|\sigma-n\rangle \langle\sigma-n|b\rangle\right) \\ &= \left(\sum_{n=0}^{\sigma} \left|\mathcal{A}_\sigma(k,n)\right|\right)^2.\end{aligned}$$

Finally, inserting the above formula for the trace norm of $\rho_{\text{out}}^{(k,\sigma)}$ into Eq. (4.6), we obtain

$$E_{\mathcal{N}}\left(\rho_{\text{out}}^{(k,\sigma)}\right) = 2\log_2\left(\sum_{n=0}^{\sigma} |\mathcal{A}_\sigma(k,n)|\right) = 2\log_2\left(\sum_{n=0}^{\sigma} \left|\phi_n\left(k-\frac{\sigma}{2},\sigma\right)\right|\right). \tag{4.8}$$

We observe that the readouts k and $\sigma-k$ not only uniquely define the state $|\Psi_{\text{out}}^{(k,\sigma)}\rangle$, but also the amount of entanglement in it. The maximum amount of entanglement which can be created in a Hilbert space of dimension $(\sigma+1)$ is $E_{\mathcal{N}_{\max}} = \log_2(\sigma+1)$. Our protocol allows one to achieve values close to this maximum, as shown in the lossless case for $\sigma = 4$ in Fig. 4.2, with the maximal value $E_{\mathcal{N}_{\max}} \approx 2.3$. The decrease in entanglement for $k = \frac{\sigma}{2}$ results from the multiphoton HOM effect, whereupon all odd photon-number components disappear (see photon number statistics in the last subfigure of Fig. 3.4). This leads to an effective reduction of the Hilbert space dimension to $(\frac{\sigma}{2}+1)$ and thus the maximal entanglement, $\log_2(\frac{\sigma}{2}+1)$ or ≈ 1.6 at $\sigma = 4$. For comparison, Bell states have logarithmic negativity, $E_{\mathcal{N}_{\text{Bell}}} = 1$, which can be calculated following the steps above for a Bell pair $|\Psi_{\text{Bell}}\rangle = \frac{1}{\sqrt{2}}(|00\rangle + |11\rangle)$. This is the same as we obtain for $\sigma = 1$, that is $|\Psi_{\text{out}}^{(k,1)}\rangle = \frac{1}{\sqrt{2}}(|01\rangle \pm i|10\rangle)$ where the pm sign is for the two cases $k = 0$ or $k = 1$.

4.2.2 Protocol efficiency

It is instructive to know how often we may expect to distribute the output state $|\Psi_{\text{out}}^{(k,\sigma)}\rangle$, i.e. the probability of Charlie measuring $k, \sigma-k$, in ideal circumstances. To do that we start with finding the state just after modes a_2 and b_2 interfere on the beam splitter

$$\begin{aligned}|\Psi_{\text{BS}}\rangle &= \sum_{n,m=0}^{\infty} \sqrt{\lambda_n\,\lambda_m}\, |n,m\rangle_{a_1,b_1}\, \mathcal{U}_{\text{BS}}\, |n,m\rangle_{a_2,b_2}\,, \\ \rho_{\text{BS}} = |\Psi_{\text{BS}}\rangle\langle\Psi_{\text{BS}}| &= \sum_{n,m,p,q=0}^{\infty} \sqrt{\lambda_n\,\lambda_m\,\lambda_p\,\lambda_q}\, |n,m\rangle\langle p,q|_{a_1,b_1} \otimes \mathcal{U}_{\text{BS}}\, |n,m\rangle\langle p,q|_{a_2,b_2}\, \mathcal{U}_{\text{BS}}^{\dagger}.\end{aligned} \tag{4.9}$$

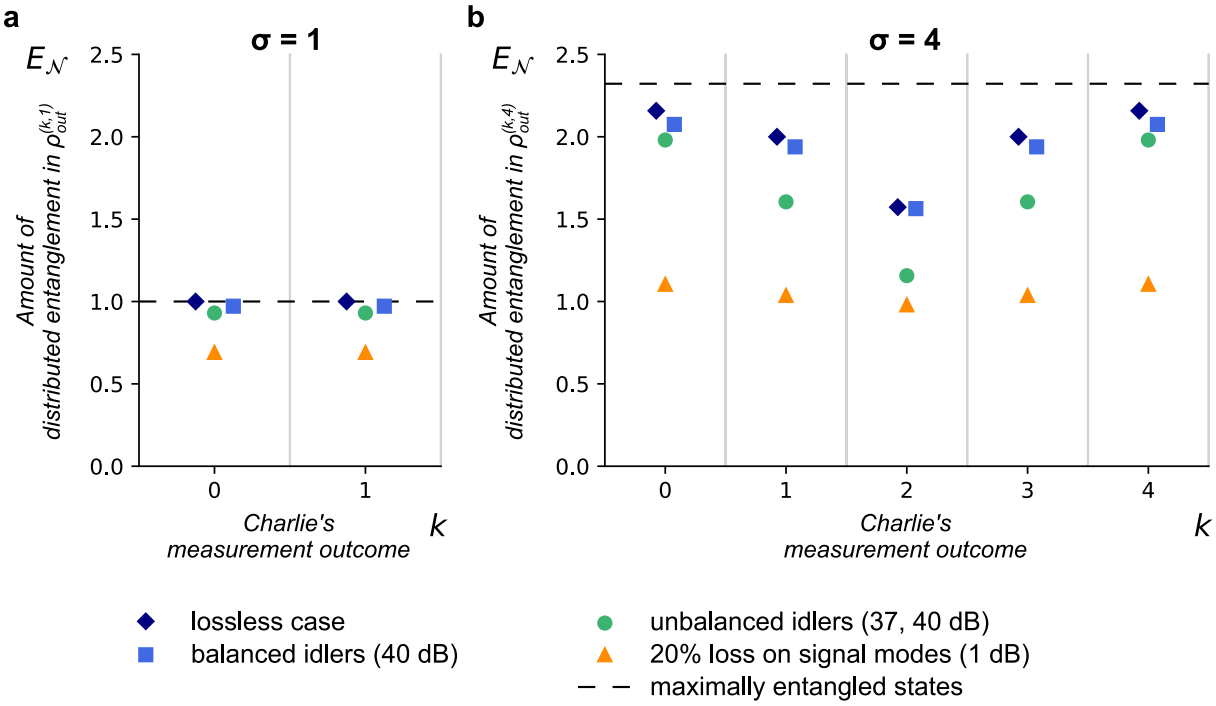

Figure 4.2: The amount of distributed entanglement in the shared state $\rho_{\text{out}}^{(k,\sigma)}$ as a function of Charlie's measurement outcome $k, \sigma - k$. The entanglement is quantified by the value of the logarithmic negativity $E_\mathcal{N}$ and is calculated for $g = 0.1$ and **a)** $\sigma = 1$ and **b)** $\sigma = 4$ photons detected in total by Charlie. The value of $E_\mathcal{N} = \log_2(\sigma + 1)$ for the maximally entangled state possible with the same number of photons is shown by the dashed black line. The dark blue diamonds depict the lossless case (Eq. 4.8). At $k = \sigma/2$, as a result of the multi-photon Hong–Ou–Mandel (HOM) effect, all odd photon-number components disappear, halving the basis and reducing the maximal entanglement to $\log_2(\sigma/2 + 1)$. This is reflected by the dip at $k = 2$. The blue squares represent the numerically computed values for a system where 40 dB losses were experienced by the photons in the idler modes a_2 and b_2. It is remarkable that these values match almost exactly the ideal case. This is one of the two main results of this work. For comparison, the results for two other scenarios of losses in the system are also shown. The green circles indicate the situation where the photons in the idler modes a_2 and b_2 experience different losses: 37 dB in one mode and 40 dB in the other (50% higher attenuation in one arm). The orange triangles illustrate the situation where a small amount of losses (20%) are present in the signal modes a_1 and b_1 only. Losses in signal modes are detrimental to the amount of distributed entanglement but can be overcome using the delayed-choice scheme. All non-ideal cases were computed for 50% detection efficiency at the PNR detectors. Vertical grid lines separate the photon-number bins.

We then observe that the probability of measuring $k, \sigma - k$ after the beam splitter will be independent of the number of photons in the signal modes a_1, b_1. Thus, we trace out these modes to find the reduced density matrix for the idler modes a_2, b_2

$$\rho_{a_2,b_2} = \mathrm{Tr}_{a_1,b_1}\left\{\rho_{\mathrm{out}}\right\} = \sum_{n,m=0}^{\infty} \lambda_n \, \lambda_m U_{\mathrm{BS}} \left|n,m\right\rangle \left\langle n,m\right|_{a_2,b_2} U_{\mathrm{BS}}^{\dagger}. \tag{4.10}$$

The probability of detecting $|k, \sigma - k\rangle$ by Charlie equals

$$\begin{aligned} p_{(k,\sigma)} &= \mathrm{Tr}\left\{\left|k,\sigma-k\right\rangle \left\langle k,\sigma-k\right| \rho_{a_2,b_2}\right\} \\ &= \sum_{n,m=0}^{\infty} \lambda_n \, \lambda_m \left\langle k,\sigma-k\right| U_{\mathrm{BS}} \left|n,m\right\rangle \left\langle n,m\right|_{a_2,b_2} U_{\mathrm{BS}}^{\dagger} \left|k,\sigma-k\right\rangle . \end{aligned} \tag{4.11}$$

The beam splitter interaction is particle number conserving, therefore $\sigma = n + m$. In addition, $\lambda_a \lambda_b = \frac{\lambda_{a+b}}{\cosh^2 g}$. According to Eq. (4.2), $\langle k, \sigma - k| U_{\mathrm{BS}} |n, m\rangle = \mathcal{A}_{\sigma}(k, n)$ which leads to the following expression for the probability

$$p_{(k,\sigma)} = \sum_{n=0}^{\infty} \lambda_n \, \lambda_{\sigma-n} \left|\mathcal{A}_{\sigma}(k,n)\right|^2 = \frac{\lambda_{\sigma}}{\cosh^2 g} \sum_{n=0}^{\infty} \left|\mathcal{A}_{\sigma}(k,n)\right|^2 = \frac{\lambda_{\sigma}}{\cosh^2 g}. \tag{4.12}$$

This probability depends solely on the parametric gain g and σ. Since there are $\sigma + 1$ values of k, the probability to generate an arbitrary σ photon state is $(\sigma + 1)p_{(k,\sigma)}$.

The success rate of obtaining a particular total photon number σ is then calculated from multiplying $(\sigma + 1)p_{(k,\sigma)}$ by the repetition rate of the pump, f_{rep}. For example, assuming $g = 0.1$ and $f_{\mathrm{rep}} = 80$ MHz, we would observe events having $\sigma = 4$ photons in total with frequency 3.82 Hz and events having $\sigma = 1$ with frequency 1.56 MHz.

4.3 Protocol's operation in lossy conditions

In reality, the protocol will be subject to losses in photon transmission and device imperfections. Depending on the application of our protocol, the losses may vary from 0.2 dB/km for optical fibres to approximately 40 dB for a ground-to-satellite channel [108]. As far as the PNR devices are concerned, the best PNR detectors are the TESs as discussed in Section 2.1.3 but their maximum efficiency could drop to 50–60% (by 2–3 dB) if one included uncorrelated background counts and inefficient coupling.

One of the most promising realisations of quantum communications across large distances is to use an Earth-space channel between a satellite and the ground. We will therefore focus on the relevant numbers for this application. Along with the ideal transmission cases, Fig. 4.2 shows the numerical results for scenarios in the analysis of Earth-space quantum communications which include high losses. The first case is that of balanced idler modes (blue squares), each of which assumes losses of 40 dB (equivalent to $r_{a_2,b_2} = 99.99\%$). The idler modes are the highest source of loss, yet the distributed entanglement seems unaffected by them. Our protocol is remarkably tolerant to losses in these modes. Even though exactly symmetric losses may seem uncommon, in practice losses may always be made more symmetric by using a reference pulse to estimate the losses and introducing small arbitrary losses to correct the asymmetry.

If, however, some small asymmetries still remain, we show that the protocol remains robust in the presence of asymmetry. In our analysis we consider the case where one

channel has half as much transmittance as the other, which corresponds to 37, 40 dB losses in modes a_2 and b_2, respectively (equivalent to $r_{a_2} = 99.98\%$, $r_{b_2} = 99.99\%$). Another useful metric for the unbalanced losses is the relative transmittance $\epsilon = \frac{1-r_{b_2}}{1-r_{a_2}}$ with $\epsilon = 0.5$ in our case of interest. The results for this scenario are shown by the green circles in Fig. 4.2. We observe that significant amount of entanglement remains even with large asymmetry. This robustness to asymmetry in the transmitting channels ensures the feasibility of our proposal.

For completeness, we also include in Fig. 4.2 the case of losses in signal modes a_1 and b_1. These are shown by orange triangles. Since photons in these modes would not travel over long distances but would be measured locally in the laboratory by Alice and Bob as soon as they are created, we chose to include much smaller losses of 1 dB (equivalent to $r_{a_2,b_1} = 20\%$). We see that the most significant reduction of entanglement quality is due to signal mode losses. However, they can be reduced by applying a delayed-choice scheme to our protocol, where Alice and Bob's measurement precede Charlie's. In all of these three cases, losses at the detectors were set to a realistic value of $r_{d_1,d_2} = 50\%$.

We predict to be able to distribute near-maximally entangled states with arbitrarily large losses in the transmitting channels, whether it is an Earth-space channel or a long optical fibre. Moreover, our protocol's design is well-matched with the hardware of quantum photonics. These results were achieved with only natural sources of quantum light and existing PNR detectors. The real experimental parameters have been taken into account in all our simulations.

In the subsections below, we will back up our numerical results with analytic derivations and an extended numerical analysis.

4.3.1 Distribution over symmetric channels

In this subsection we will look at losses which appear only in the idler modes a_2, b_2 and which are considered equal, $r_a = r_b = r$. We note that the state shared by Alice and Bob will no longer be the pure state $|\Psi_{\text{out}}^{(k,\sigma)}\rangle$, but a mixed state $\rho_{\text{out}}^{(k,\sigma)}$ derived below.

A model to include losses in the transmitted channels was presented in Subsection 3.2.4 where additional beam splitters were inserted into the pathways of the photons. A mode containing n photons will reduce to

$$|n\rangle\langle n| \to \sum_{p=0}^{n} \binom{n}{p} r^p (1-r)^{n-p} |n-p\rangle\langle n-p|, \tag{4.13}$$

where we have used Eq. (3.47) but relabelled $p \to n-p$ so that p denotes the number of photons lost rather than transmitted.

Applying this procedure to the idler modes of the input state $|\Psi_{\text{in}}\rangle$ and correcting for the fact that the density matrix is non-diagonal [109] leads to the following input density

operator

$$\begin{aligned}\rho_{\text{in}} = &\sum_{n,n',m,m'=0}^{\infty} \sqrt{\lambda_n\,\lambda_{n'}\,\lambda_m\,\lambda_{m'}} \sum_{p=0}^{\min(n,n')} \sqrt{\binom{n}{p}\binom{n'}{p}\,(1-r)^{n+n'-2p}\,r^{2p}} \\ &\times \sum_{q=0}^{\min(m,m')} \sqrt{\binom{m}{q}\binom{m'}{q}\,(1-r)^{m+m'-2q}\,r^{2q}} \\ &\times |n,m\rangle\,\langle n',m'|_{a_1,b_1} \otimes |n-p,m-q\rangle\,\langle n'-p,m'-q|_{a_2,b_2} \\ = &\sum_{n,n',m,m'=0}^{\infty} \sqrt{\lambda_n\,\lambda_{n'}\,\lambda_m\,\lambda_{m'}} \\ &\times \sum_{p=0}^{\min(n,n')} \sum_{q=0}^{\min(m,m')} \sqrt{\binom{n}{p}\binom{n'}{p}\binom{m}{q}\binom{m'}{q}\,(1-r)^{n+n'+m+m'-2p-2q}\,r^{2p+2q}} \\ &\times |n,m\rangle\,\langle n',m'|_{a_1,b_1} \otimes |n-p,m-q\rangle\,\langle n'-p,m'-q|_{a_2,b_2}\,.\end{aligned} \tag{4.14}$$

After the idler modes interfere on the beam splitter and are projected onto $|k,\sigma-k\rangle_{d_2,d_1}$, the total photon number in the idler modes is known (assuming the beam splitter itself and detection is lossless) and equals $\sigma = n+m-p-q$, where n and m are the numbers of photons generated by Alice and Bob, respectively, and p and q are the numbers of photons lost on the way to Charlie. This results in the creation of the following state

$$\begin{aligned}\rho_{\text{out}}^{(k,\sigma)} = &\tilde{\mathcal{N}}^2 \sum_{n,n',m,m'=0}^{\infty} \sqrt{\lambda_n\,\lambda_{n'}\,\lambda_m\,\lambda_{m'}}\,|n,m\rangle\,\langle n',m'|_{a_1,b_1} \\ &\times \sum_{p=0}^{\min(n,n')} \sum_{q=0}^{\min(m,m')} \sqrt{\binom{n}{p}\binom{n'}{p}\binom{m}{q}\binom{m'}{q}}(1-r)^{\sigma}\,r^{\frac{n+n'}{2}+\frac{m+m'}{2}-\sigma} \\ &\times \mathcal{A}_\sigma(k,n-p)\,\mathcal{A}_\sigma^*(k,n'-p)\,\delta_{\sigma,n+m-p-q}\,\delta_{\sigma,n'+m'-p-q} \\ = &\tilde{\mathcal{N}}^2 \sum_{n,n',m,m'=0}^{\infty} r^{-\sigma}\sqrt{r^n\lambda_n\,r^{n'}\lambda_{n'}\,r^m\lambda_m\,r^{m'}\lambda_{m'}}\,|n,m\rangle\,\langle n',m'|_{a_1,b_1} \\ &\times \sum_{p=0}^{\min(n,n')} \sum_{q=0}^{\min(m,m')} \sqrt{\binom{n}{p}\binom{n'}{p}\binom{m}{q}\binom{m'}{q}} \\ &\times \mathcal{A}_\sigma(k,n-p)\,\mathcal{A}_\sigma^*(k,n'-p)\,\delta_{\sigma,n+m-p-q}\,\delta_{\sigma,n'+m'-p-q}, \\ = &\tilde{\mathcal{N}}^2 \sum_{n,n',m,m'=0}^{\infty} r^{-\sigma}\sqrt{r^n\lambda_n\,r^{n'}\lambda_{n'}\,r^m\lambda_m\,r^{m'}\lambda_{m'}}\,|n,m\rangle\,\langle n',m'|_{a_1,b_1} \\ &\times \sum_{p=\max(0,n-\sigma,n'-\sigma)}^{\min(n+m-\sigma,n,n')} \sqrt{\binom{n}{p}\binom{n'}{p}\binom{m}{S-\sigma-p}\binom{m'}{S-\sigma-p}} \\ &\times \mathcal{A}_\sigma(k,n-p)\,\mathcal{A}_\sigma^*(k,n'-p),\end{aligned} \tag{4.15}$$

where in the second step we have absorbed $(1-r)^\sigma$ into the normalization $\tilde{\mathcal{N}}^2$ and in the third the delta functions allowed us to remove the sum over q. The normalizations is

given by

$$\frac{1}{\tilde{\mathcal{N}}^2} = \sum_{n,m=0}^{\infty} \lambda_n \lambda_m r^{n+m-\sigma} \sum_{p=\max(0,n-\sigma)}^{\min(n,n+m-\sigma)} \binom{n}{p} \binom{m}{n+m-\sigma-p} \left|\mathcal{A}_\sigma(k, n-p)\right|^2 . \tag{4.16}$$

Since the signal modes a_1, b_1 are assumed to be lossless, in principle the total number of photons in these modes could be infinite. Nevertheless, we will label it as $S = n + m = n' + m'$. It then follows that $n, n', m, m' \leq S$ and $\sigma = S - p - q$ while S takes the values from σ up to infinity. Replacing m with $S - n$ and m' with $S - n'$ the state takes the form

$$\begin{aligned}\rho_{\text{out}}^{(k,\sigma)} = \tilde{\mathcal{N}}^2 \sum_{S=\sigma}^{\infty} \sum_{n,n'=0}^{S} r^{-\sigma} \sqrt{r^n \lambda_n \, r^{n'} \lambda_{n'} \, r^{S-n} \lambda_{S-n} \, r^{S-n'} \lambda_{S-n'}} \left|n, S-n\right\rangle \left\langle n', S-n'\right|_{a_1,b_1} \\ \times \sum_{p=\max(0,n-\sigma,n'-\sigma)}^{\min(S-\sigma,n,n')} \sqrt{\binom{n}{p}\binom{n'}{p}\binom{S-n}{S-\sigma-p}\binom{S-n'}{S-\sigma-p}} \\ \times \mathcal{A}_\sigma(k, n-p) \, \mathcal{A}_\sigma^*(k, n'-p).\end{aligned} \tag{4.17}$$

We also notice that $\lambda_n \lambda_{S-n} = \frac{\lambda_S}{\cosh^2 g}$ which allows us to simplify Eq. (4.17) to

$$\begin{aligned}\rho_{\text{out}}^{(k,\sigma)} = \tilde{\mathcal{N}}^2 \sum_{S=\sigma}^{\infty} r^{S-\sigma} \, \lambda_S \sum_{n,n'=0}^{S} \left|n, S-n\right\rangle \left\langle n', S-n'\right|_{a_1,b_1} \\ \times \sum_{p=\max(0,n-\sigma,n'-\sigma)}^{\min(S-\sigma,n,n')} \sqrt{\binom{n}{p}\binom{n'}{p}\binom{S-n}{S-\sigma-p}\binom{S-n'}{S-\sigma-p}} \\ \times \mathcal{A}_\sigma(k, n-p) \, \left(\mathcal{A}_\sigma^*(k, n'-p)\right),\end{aligned} \tag{4.18}$$

where once again the constant factor $\frac{1}{\cosh^2 g}$ has been absorbed by the normalization

$$\frac{1}{\tilde{\mathcal{N}}^2} = \sum_{S=\sigma}^{\infty} r^{S-\sigma} \lambda_S \sum_{n=0}^{S} \sum_{p=\max(0,n-\sigma)}^{\min(S-\sigma,n)} \binom{n}{p} \binom{S-n}{S-\sigma-p} \left|\mathcal{A}_\sigma(k, n-p)\right|^2 . \tag{4.19}$$

It is then possible to extract from Eq. (4.18) an internal density matrix with fixed S

$$\begin{aligned}\rho_{\text{int}}^{(\sigma,k,S)} = \tilde{\mathcal{N}}_{\text{int}}^2 \sum_{n,n'=0}^{S} \left|n, S-n\right\rangle \left\langle n', S-n'\right|_{a_1,b_1} \times \\ \times \sum_{p=\max(0,n-\sigma,n'-\sigma)}^{\min(S-\sigma,n,n')} \sqrt{\binom{n}{p}\binom{n'}{p}\binom{S-n}{S-\sigma-p}\binom{S-n'}{S-\sigma-p}} \times \\ \times \mathcal{A}_\sigma(k, n-p) \, \left(\mathcal{A}_\sigma^*(k, n'-p)\right),\end{aligned}$$

with

$$\frac{1}{\tilde{\mathcal{N}}_{\text{int}}^2} = \sum_{n=0}^{S} \sum_{p=\max(0,n-\sigma)}^{\min(S-\sigma,n)} \binom{n}{p} \binom{S-n}{S-\sigma-p} \left|\mathcal{A}_\sigma(k, n-p)\right|^2 . \tag{4.20}$$

By shifting the summation index to $p \to n - p$ (which means p is now the number of photons which have survived the trip), the above equation turns into

$$\begin{aligned}\frac{1}{\tilde{\mathcal{N}}_{\text{int}}^2} &= \sum_{n=0}^{S} \sum_{p=\max(0,n+\sigma-S)}^{\min(\sigma,n)} \binom{n}{n-p}\binom{S-n}{S-\sigma-n+p}\left|\mathcal{A}_\sigma(k,p)\right|^2 \\ &= \sum_{p=\max(0,n+\sigma-S)}^{\min(\sigma,n)} \left|\mathcal{A}_\sigma(k,p)\right|^2 \sum_{n=0}^{S} \binom{n}{p}\binom{S-n}{\sigma-p} \\ &= \binom{S+1}{\sigma+1}.\end{aligned} \tag{4.21}$$

This result was achieved as follows. The Chu-Vandermonde identity $\sum_{n=0}^{S}\binom{n}{p}\binom{S-n}{\sigma-p} = \binom{S+1}{\sigma+1}$ is valid as long as $0 \le p \le \sigma \le S$ which is satisfied in our case. We then used the fact that the probabilities $|\mathcal{A}_\sigma(k,p)|^2$ must sum to one, $\sum_{p=\max(0,n+\sigma-S)}^{\min(\sigma,n)}|\mathcal{A}_\sigma(k,p)|^2 = 1$.

For $S = \sigma$, $\rho_{\text{int}}^{(\sigma,k,S)}$ reproduces the density operator for the lossless case

$$\begin{aligned}\rho_{\text{int}}^{(\sigma,k,\sigma)} = &\sum_{n,n'=0}^{\sigma} |n,\sigma-n\rangle\langle n',\sigma-n'|_{a_1,b_1} \\ &\times \sum_{p=\max(0,n-\sigma,n'-\sigma)}^{\min(\sigma-\sigma,n,n')} \sqrt{\binom{n}{p}\binom{n'}{p}\binom{\sigma-n}{\sigma-\sigma-p}\binom{\sigma-n'}{\sigma-\sigma-p}} \\ &\times \mathcal{A}_\sigma(k,n-p)\,\mathcal{A}_\sigma^*(k,n'-p) \\ = &\sum_{n,n'=0}^{\sigma} \mathcal{A}_\sigma(k,n)\,\mathcal{A}_\sigma^*(k,n')\ |n,\sigma-n\rangle\langle n',\sigma-n'|_{a_1,b_1} \\ = &\ |\Psi_{\text{out}}^{(k,\sigma)}\rangle\langle\Psi_{\text{out}}^{(k,\sigma)}|,\end{aligned} \tag{4.22}$$

as expected. Eq. (4.18) can now be rewritten as

$$\rho_{\text{out}}^{(k,\sigma)} = \tilde{\mathcal{N}}^2 \sum_{S=\sigma}^{\infty} \frac{r^{S-\sigma}\lambda_S}{\tilde{\mathcal{N}}_{\text{int}}^2}\,\rho_{\text{int}}^{(\sigma,k,S)} = \tilde{\mathcal{N}}^2 \sum_{S=\sigma}^{\infty} \chi_{\sigma,S}\,\rho_{\text{int}}^{(\sigma,k,S)}, \tag{4.23}$$

where $\chi_{\sigma,S} = r^{S-\sigma}\,\lambda_S\binom{S+1}{\sigma+1}$. As a consequence the normalization in Eq. (4.19) also simplifies

$$\frac{1}{\tilde{\mathcal{N}}^2} = \sum_{S=\sigma}^{\infty} r^{S-\sigma}\lambda_S\binom{S+1}{\sigma+1} = \frac{\lambda_\sigma}{(1-r\tanh^2 g)^{\sigma+2}}, \tag{4.24}$$

where we have used the identity $\sum_{S=\sigma}^{\infty} x^S\binom{S+1}{\sigma+1} = (1-x)^{-\sigma-2}x^\sigma$.

The final expression for the density operator in the case of symmetric losses in the idler modes is

$$\rho_{\text{out}}^{(k,\sigma)} = \sum_{S=\sigma}^{\infty} p_{S|\sigma}\,\rho_{\text{int}}^{(\sigma,k,S)}, \tag{4.25}$$

where $p_{S|\sigma}$ is the probability to obtain S photons, given an outcome of $|k,\sigma-k\rangle$ was obtained at the remote station. We note that Alice and Bob know σ after Charlie communicates the measurement outcome, but none of them knows S exactly, except that it

is given by the probability distribution $p_{S|\sigma}$. The probability quantifies the contribution of $\rho_{\text{int}}^{(\sigma,k,S)}$ to the final density operator and is given in its full form below

$$p_{S|\sigma} = \tilde{\mathcal{N}}^2 \chi_{\sigma,S} = (r \tanh^2 g)^{S-\sigma} (1 - r \tanh^2 g)^{\sigma+2} \binom{S+1}{\sigma+1}. \tag{4.26}$$

Provided we are in the limit $r \tanh^2 g \ll 1$, the term $(r \tanh^2 g)^{S-\sigma}$ decreases with S more rapidly than $\binom{S+1}{\sigma+1}$ increases, so that $p_{S|\sigma}$ is largest for $S = \sigma$ and rapidly decreases, as is shown in Fig. 4.3. This means that the primary component of the mixed state is $\rho_{\text{int}}^{(\sigma,k,\sigma)}$, which is identical to the lossless state $|\Psi_{\text{out}}^{(k,\sigma)}\rangle \langle\Psi_{\text{out}}^{(k,\sigma)}|$, as has been shown in Eq. (4.22). Provided that the gain g stays within the non-depletion regime, $g^2 \ll 1$, the limit $r \tanh^2(g) \ll 1$ holds even as $r \to 1$, so that the output state is largely unchanged $\rho_{\text{out}}^{(k,\sigma)} \approx |\Psi_{\text{out}}^{(k,\sigma)}\rangle \langle\Psi_{\text{out}}^{(k,\sigma)}|$ and the entanglement of the final states remains high even in the presence of arbitrarily high losses in the idler modes. This is reminiscent of a $g^{(2)}$ correlation function measurement, which is known to be immune to losses [110].

A more thorough analysis confirms these findings further. Fig. 4.4 shows the results of numerical computations of the logarithmic negativity for the state $\rho_{\text{out}}^{(k,\sigma)}$. We have analysed the effect of idler losses ranging from 0 to 100% in steps of 10. In this figure losses are also given in dB found by applying the formula $-10 \log_{10}(1 - r)$. Indeed, the decrease of the logarithmic negativity representing the amount of distributed entanglement with increasing losses in the idler modes is almost imperceptible.

Although it would be too involving to include imperfect detection in our derivations of the state $\rho_{\text{out}}^{(k,\sigma)}$, it is quite straightforward to add losses in our numerical programme. We considered two scenarios: 95% typical for a TES device [18] and 60% in case the efficiency dropped due to unusually high uncorrelated background counts or inefficient coupling, which might be the case for detection in space. As we see in Fig. 4.5, the results are very similar to those in Fig. 4.4. Therefore, imperfect detection does not significantly affect the efficiency of the protocol, as it is a minor addition compared to the already large idler losses (5-40 dB).

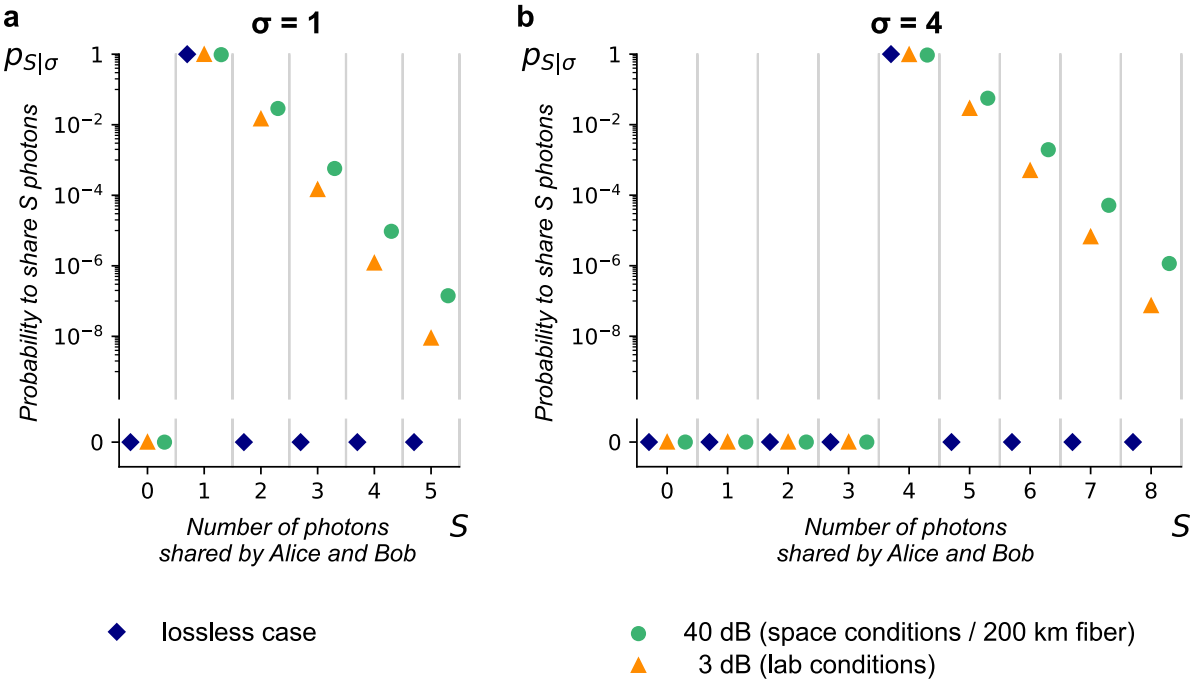

Figure 4.3: The figure shows the multi-photon character of the state $\rho_{\text{out}}^{(k,\sigma)}$ shared by Alice and Bob. The probability, $p_{S|\sigma}$, that Alice and Bob share S total photons given **a)** $\sigma = 1$ and **b)** $\sigma = 4$ photons were measured by Charlie, plotted for a realistic value of parametric gain, $g = 0.1$. The blue diamonds depict the case of lossless idler modes ($r = 0$), here S is always equal to σ because the signal and idler modes have equal photon numbers and Charlie's entangling measurement is photon number preserving. The orange triangles depict idler losses of 3 dB ($r = 0.5$), as might be present in lab conditions, while green circles depict 40 dB ($r = 0.9999$), as in an Earth-space channel or 200 km of optical fibre. Idler losses introduce higher-order contributions $S > \sigma$ but the primary component and lower-bound is still $S = \sigma$ since, in the absence of dark counts and background photons, Charlie cannot measure more photons than were sent to him in Alice and Bob's idler modes. Losses in the signal modes may introduce components $S < \sigma$ but these can be significantly reduced by using a delayed-choice scheme where Alice and Bob's measurements precede that of Charlie. Vertical grid lines separate the photon-number bins.

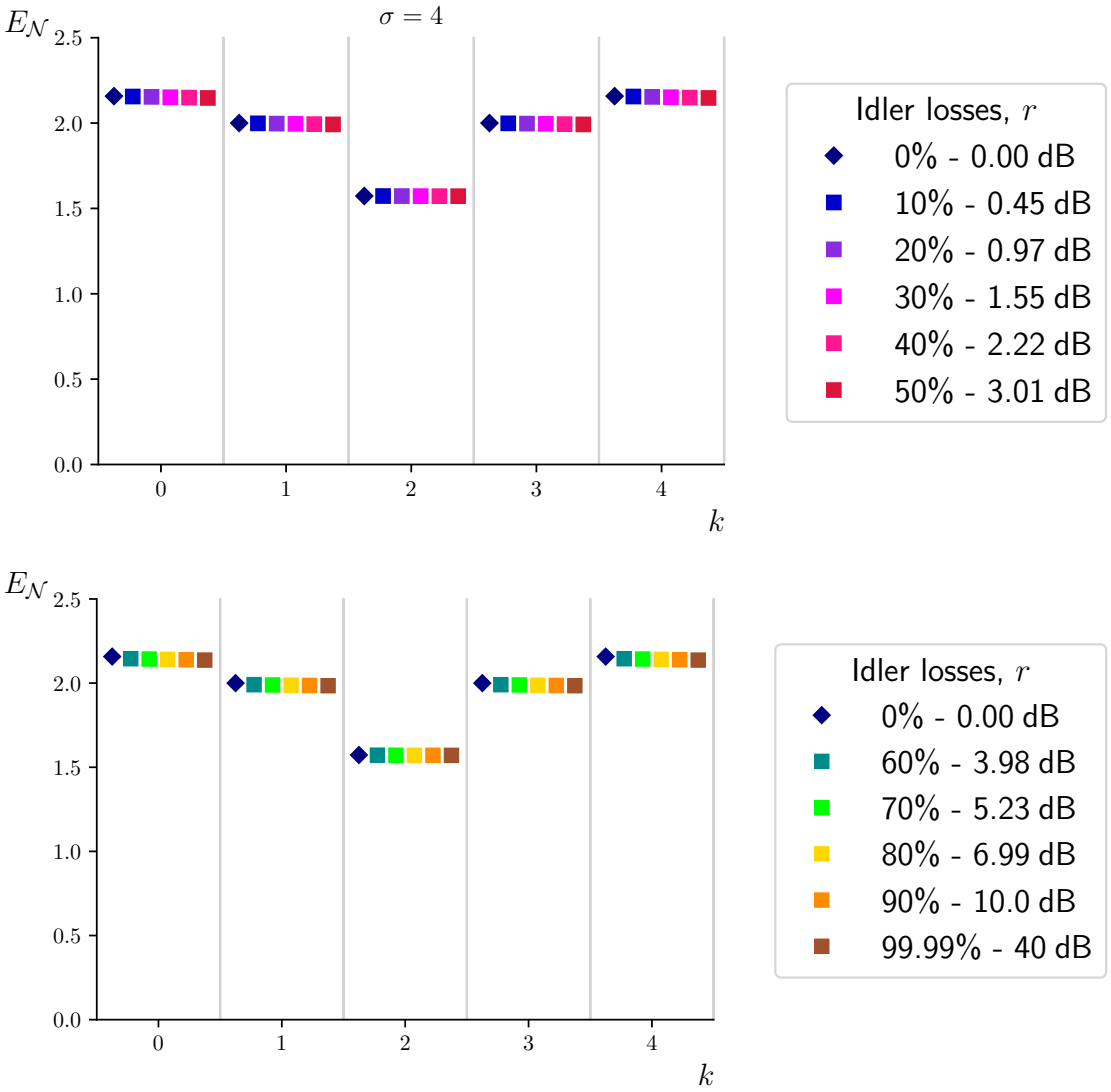

Figure 4.4: Logarithmic negativity $E_{\mathcal{N}}$ of the output state $\rho_{\text{out}}^{(k,\sigma)}$, given in Eq. (4.18), as a function of Charlie's measurement outcomes $k, \sigma - k$. The results were computed for $g = 0.1$ and $\sigma = 4$ assuming symmetric losses r in idler modes a_2 and b_2 with losses in the remaining modes and at the detectors set to zero. The losses vary from 0% (ideal case) to 99.99% (split between the upper and the lower figure) which is equivalent to 40 dB. We observe that the amount of entanglement shared between Alice and Bob is nearly unchanged by even the highest losses.

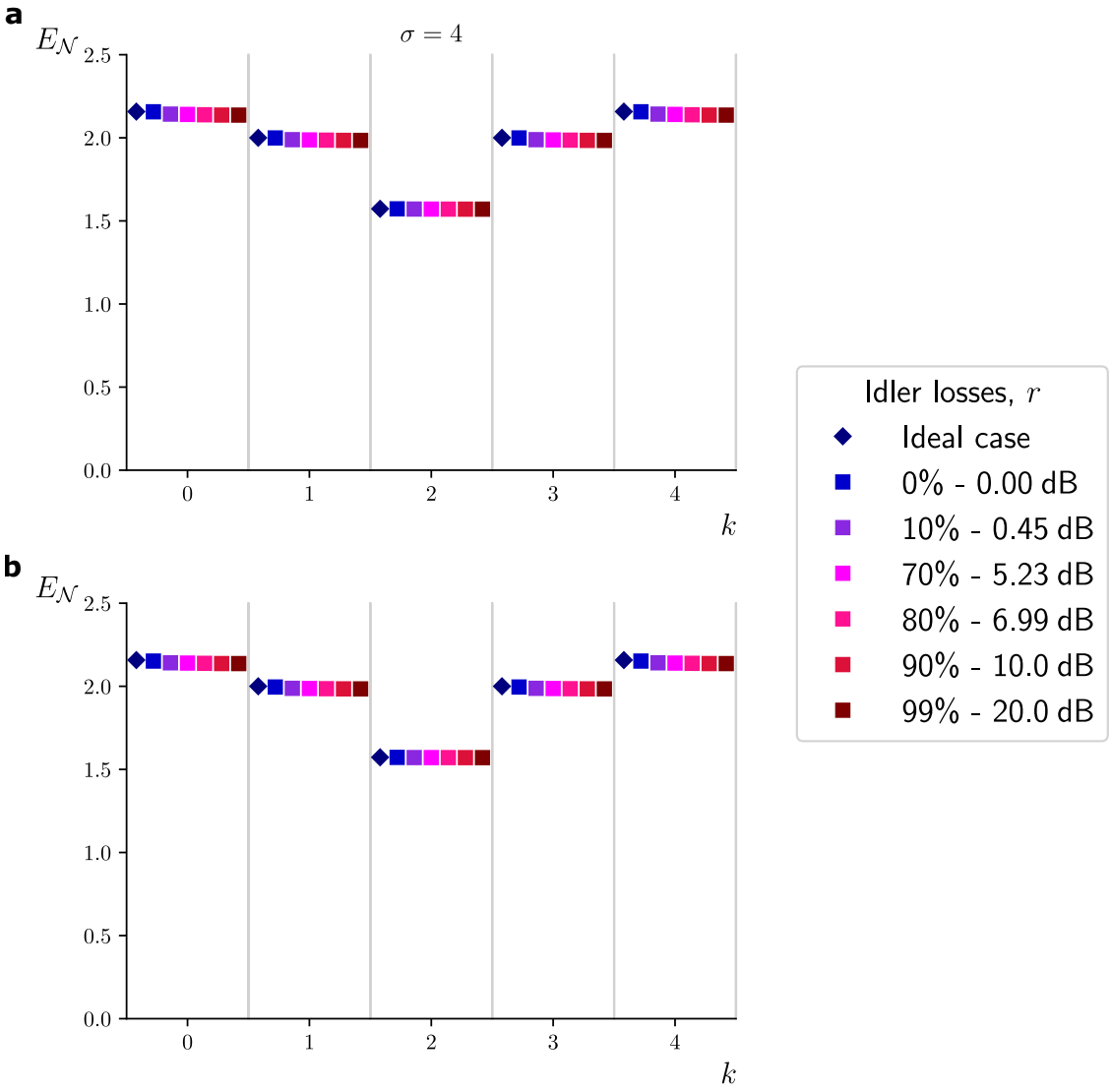

Figure 4.5: Logarithmic negativity $E_{\mathcal{N}}$ of the output state $\rho_{\text{out}}^{(k,\sigma)}$ as a function of Charlie's measurement outcome $k, \sigma - k$. The results were computed for $g = 0.1$ and $\sigma = 4$ assuming symmetric losses r in idler modes a_2 and b_2 and losses at the detectors located behind the beam splitter set to **a)** $r_d = 5\%$ and **b)** $r_d = 40\%$. The losses at signal modes were set to zero, $r_s = 0$. The ideal case correponds to no losses, that is $r = r_s = r_d = 0$. The losses in the idler modes varied from 0% to 99%, always with imperfect detection. We observe there is a negligible difference in the amount of shared entanglement in those cases compared to the ideal case. We conclude the protocol maintains its quality even with imperfect detectors.

4.4 Distribution over asymmetric channels

In a real experimental setting, losses in the two transmitting channels corresponding to the idler modes will never be perfectly equal. In principle, the channel with fewer losses could have some losses artificially added to balance the channels but it would be interesting to see how the asymmetry of losses influences the operation of our protocol.

To simplify the derivations, we consider first the case when Bob's idler mode b_2 is lossless ($r_b = 0, t_b = 1$). We will then define Alice's idler mode transmittance, t_a as a fraction of Bob's transmittance, $t_a = \epsilon t_b = \epsilon$. As in the previous section, the input density operator, now given by

$$\begin{aligned}\rho_{\text{in}} = \sum_{n,n',m,m'=0}^{\infty} \sqrt{\lambda_n\,\lambda_{n'}\,\lambda_m\,\lambda_{m'}} \sum_{p=0}^{\min(n,n')} \sqrt{\binom{n}{p}\binom{n'}{p}(1-r_a)^{n+n'-2p}\,r_a^{2p}} \\ \times \sum_{q=0}^{\min(m,m')} \sqrt{\binom{m}{q}\binom{m'}{q}(1-r_b)^{m+m'-2q}\,r_b^{2q}} \\ \times |n,m\rangle\langle n',m'|_{a_1,b_1} \otimes |n-p,m-q\rangle\langle n'-p,m'-q|_{a_2,b_2}\,,\end{aligned} \tag{4.27}$$

is modified by the protocol and the inclusion of losses modelled by the extra beam splitters into

$$\begin{aligned}\rho_{\text{out}}^{(k,\sigma)} &= \tilde{\mathcal{N}}^2 \sum_{n,n',m,m'=0}^{\infty} \sqrt{\lambda_n\,\lambda_{n'}\,\lambda_m\,\lambda_{m'}}\,|n,m\rangle\langle n',m'|_{a_1,b_1} \\ &\quad\times \sum_{p=0}^{\min(n,n')} \sum_{q=0}^{\min(m,m')} \sqrt{\binom{n}{p}\binom{n'}{p}t_a^{n+n'-2p}(1-t_a)^{2p}}\sqrt{\binom{m}{q}\binom{m'}{q}t_b^{m+m'-2q}(1-t_b)^{2q}} \\ &\quad\times \mathcal{A}_\sigma(k,n-p)\,\left(\mathcal{A}_\sigma(k,n'-p)\right)^*\,\delta_{\sigma,n+m-p-q}\,\delta_{\sigma,n'+m'-p-q} \\ &= \tilde{\mathcal{N}}^2 \sum_{n,n',m,m'=0}^{\infty} \sqrt{\lambda_n\,\lambda_{n'}\,\lambda_m\,\lambda_{m'}}\,|n,m\rangle\langle n',m'|_{a_1,b_1} \\ &\quad\times \sum_{p=0}^{\min(n,n')} \sqrt{\binom{n}{p}\binom{n'}{p}\epsilon^{n+n'-2p}(1-\epsilon)^{2p}} \\ &\quad\times \mathcal{A}_\sigma(k,n-p)\,\left(\mathcal{A}_\sigma(k,n'-p)\right)^*\,\delta_{\sigma,n+m-p}\,\delta_{\sigma,n'+m'-p},\end{aligned} \tag{4.28}$$

where we could remove the sum over q, as only the $q = 0$ term would contribute to the sum for $t_b = 1$.

The Kronecker delta functions allows us to set $m = S - n, m' = S - n'$ and replace the sum over m, m' with a single sum over S. They also tell us that $p = S - \sigma$, so that the sum over p can also be removed. Thus, the density matrix takes the following form

$$\begin{aligned}\rho_{\text{out}}^{(k,\sigma)} = \tilde{\mathcal{N}}^2 \sum_{S=\sigma}^{\infty} \sum_{n,n'=S-\sigma}^{S} \sqrt{\lambda_n\,\lambda_{n'}\,\lambda_{S-n}\,\lambda_{S-n'}}\,|n,S-n\rangle\langle n',S-n'|_{a_1,b_1} \\ \times \sqrt{\binom{n}{S-\sigma}\binom{n'}{S-\sigma}\epsilon^{n+n'+2(\sigma-S)}(1-\epsilon)^{2(S-\sigma)}} \\ \times \mathcal{A}_\sigma(k,n-S+\sigma)\,\left(\mathcal{A}_\sigma(k,n'-S+\sigma)\right)^*.\end{aligned} \tag{4.29}$$

Again, we notice that $\lambda_n\lambda_{S-n} = \frac{\lambda_S}{\cosh^2 g}$, and absorb $\frac{1}{\cosh^2 g}$ into $\tilde{\mathcal{N}}^2$

$$\begin{aligned}\rho_{\text{out}}^{(k,\sigma)} = \tilde{\mathcal{N}}^2 \sum_{S=\sigma}^{\infty} \lambda_S \left(\frac{1-\epsilon}{\epsilon}\right)^{S-\sigma} \sum_{n,n'=S-\sigma}^{S} \epsilon^{\frac{n+n'}{2}} |n, S-n\rangle \langle n', S-n'|_{a_1,b_1} \\ \times \sqrt{\binom{n}{S-\sigma}\binom{n'}{S-\sigma}} \mathcal{A}_\sigma(k, n-S+\sigma) \left(\mathcal{A}_\sigma(k, n'-S+\sigma)\right)^*,\end{aligned} \tag{4.30}$$

where the normalization factor equals

$$\frac{1}{\tilde{\mathcal{N}}^2} = \sum_{S=\sigma}^{\infty} \lambda_S \left(\frac{1-\epsilon}{\epsilon}\right)^{S-\sigma} \sum_{n=S-\sigma}^{S} \epsilon^n \binom{n}{S-\sigma} \left|\mathcal{A}_\sigma(k, n-S+\sigma)\right|^2. \tag{4.31}$$

We notice that, unlike in Eq. (4.23), it is impossible to decompose the matrix into ϵ-independent components. Instead, we obtain

$$\rho_{\text{out}}^{(k,\sigma)} = \tilde{\mathcal{N}}^2 \sum_{S=\sigma}^{\infty} \chi_{\sigma,S}(\epsilon) \rho_{\text{int}}^{(\sigma,k,S)}(\epsilon), \tag{4.32}$$

where $\chi_{\sigma,S}(\epsilon) = \frac{\lambda_S}{\tilde{\mathcal{N}}(\epsilon)^2}\left(\frac{1-\epsilon}{\epsilon}\right)^{S-\sigma}$ and the density matrix components are

$$\begin{aligned}\rho_{\text{int}}^{(\sigma,k,S)}(\epsilon) = \tilde{\mathcal{N}}(\epsilon)^2 \sum_{n,n'=S-\sigma}^{S} \epsilon^{\frac{n+n'}{2}} |n, S-n\rangle \langle n', S-n'|_{a_1,b_1} \\ \times \sqrt{\binom{n}{S-\sigma}\binom{n'}{S-\sigma}} \mathcal{A}_\sigma(k, n-S+\sigma) \left(\mathcal{A}_\sigma(k, n'-S+\sigma)\right)^*,\end{aligned} \tag{4.33}$$

with

$$\frac{1}{\tilde{\mathcal{N}}(\epsilon)^2} = \sum_{n=S-\sigma}^{S} \epsilon^n \binom{n}{S-\sigma} \left|\mathcal{A}_\sigma(k, n-S+\sigma)\right|^2. \tag{4.34}$$

We find that, similar to the case of symmetric losses, the probability $\tilde{\mathcal{N}}^2\chi_{\sigma,S}(\epsilon)$ is strongly peaked at $S=\sigma$ when $g^2 \ll 1$, so that $\rho_{\text{out}}^{(k,\sigma)} \approx \rho_{\text{int}}^{(\sigma,k,\sigma)}$. However $\rho_{\text{int}}^{(\sigma,k,\sigma)}$ is no longer equal to the lossless state $|\Psi_{\text{out}}^{(k,\sigma)}\rangle \langle\Psi_{\text{out}}^{(k,\sigma)}|$ but is instead given by $\rho_{\text{int}}^{(\sigma,k,\sigma)} = |\Psi_\epsilon^{(k,\sigma)}\rangle \langle\Psi_\epsilon^{(k,\sigma)}|$ where

$$|\Psi_\epsilon^{(k,\sigma)}\rangle = \tilde{\mathcal{N}}(\epsilon)^2 \sum_{n=0}^{\sigma} \epsilon^{n/2} \mathcal{A}_\sigma(k,n) |n, \sigma-n\rangle. \tag{4.35}$$

Due to the asymmetry in transmission, Alice is more likely to lose photons than Bob and thus the symmetry $n \to \sigma - n$ of the state is broken. This is shown for the state $k=0$, $\sigma=4$ and $g=0.1$ in Fig. 4.6, where the probability for Alice, Bob to measure $n, \sigma-n$ photons is plotted for $\epsilon \in \{0, 0.33, 0.66, 1\}$. The suppression of high n states leads to an effective reduction of the Hilbert space dimension lowering the entanglement. This can also be shown analytically. Following the same steps as in Subsection 4.2.1, the logarithmic negativity of $|\Psi_\epsilon^{(k,\sigma)}\rangle$ is

$$E_{\mathcal{N}}(|\Psi_\epsilon^{(k,\sigma)}\rangle \langle\Psi_\epsilon^{(k,\sigma)}|) = 2\log_2\left(\frac{\sum_{n=0}^{\sigma} \epsilon^{n/2} \left|\mathcal{A}_\sigma(k,n)\right|}{\sqrt{\sum_{n=0}^{\sigma} \epsilon^n \left|\mathcal{A}_\sigma(k,n)\right|^2}}\right) = 2\log_2\left(\frac{\sum_{n=0}^{\sigma} \epsilon^{n/2} \left|\phi_n\left(k-\frac{\sigma}{2}, \sigma\right)\right|}{\sqrt{\sum_{n=0}^{\sigma} \epsilon^n \left|\phi_n\left(k-\frac{\sigma}{2}, \sigma\right)\right|^2}}\right). \tag{4.36}$$

It can be seen that the factor ϵ scales down the argument to the logarithm. The equation above also correctly reduces to Eq. (4.8) in the symmetric limit $\epsilon \to 1$, while in the limit of extreme asymmetry $\epsilon \to 0$ it becomes $E_{\mathcal{N}} = 0$, since the state reduces to the unentangled $|0, \sigma\rangle$. To back up the analytic derivations we computed the logarithmic

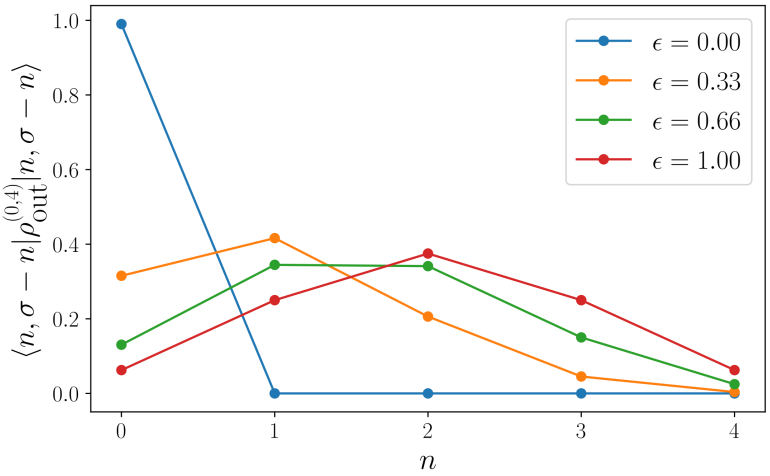

Figure 4.6: Given a state $\rho_{\text{out}}^{(0,4)}$ generated with asymmetric losses and $g = 0.1$, the probability for Alice, Bob to measure $n, \sigma - n$ photons is given by $\langle n, \sigma - n|\rho_{\text{out}}^{(k,\sigma)}|n, \sigma - n\rangle$ and plotted for $\epsilon \in \{0, 0.33, 0.66, 1\}$. Asymmetry in losses leads to asymmetry of the shared state, lowering entanglement. The probabilities sum to ~ 0.99 rather than one due to a small probability to detect $S \geq \sigma$ photons.

negativity for the full state given in Eq. (4.30) for various values of ϵ, while keeping Bob's mode ideal ($t_b = 100\%$). As before, we have taken $g = 0.1$ and displayed transmittances in percentages (%) in the following results. A representative figure showing the behaviour of logarithmic negativity as the transmittance of the idler modes is made progressively more unequal is shown in Fig. 4.7. We find that a small asymmetry $\epsilon \gtrsim 0.7$ has almost no effect but thereafter there is a significant reduction in the amount of shared entanglement.

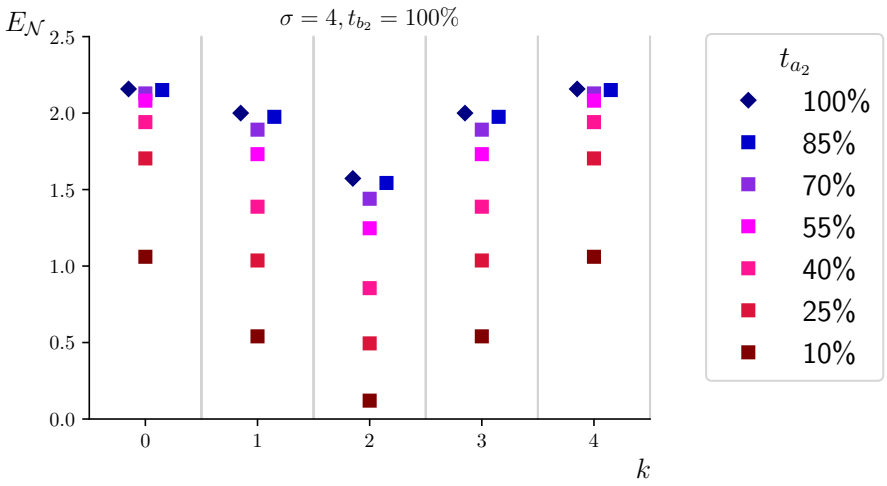

Figure 4.7: Logarithmic negativity $E_{\mathcal{N}}$ as a function of Charlie's measurement outcomes $k, \sigma - k$ computed for the state in Eq. (4.30) and $\sigma = 4$. For these results Bob's transmissivity in the idler modes was fixed and assumed to be lossless, while Alice's transmissivity varied from 100% (perfect symmetry) to 10% (equivalent to the relative transmittance of $\epsilon = 0.1$). We observe that the amount of entanglement shared between Alice and Bob is robust to small asymmetries ($\epsilon \gtrsim 0.7$).

Further analysis reveals that the entanglement is best preserved for the case where all photons emerge from the same output of the beam splitter, i.e. for $k = 0$ and $k = \sigma$. The entanglement deteriorates quickest when the outputs of the beam splitter are equally populated, $k = \sigma/2$. These results are shown in Fig. 4.8 where the dependence of the logarithmic negativity on ϵ is plotted for $\sigma = 4$. The numerically calculated values (points) match almost exactly the approximate analytical result (lines) calculated from Eq. (4.36). From these calculations it can be inferred that the protocol maintains its quality of output (up to 90% of the maximal value of entanglement) down to $\epsilon = 0.7$ for $k = 2$ and $\epsilon = 0.4$ for $k = 0$. Relative transmittance $\epsilon < 0.4$ is unlikely to occur in reality [100, 108] but in such a case artificial losses may always be introduced to balance the channels.

Finally, we numerically evaluate the effect of Bob's nonperfect transmissivity. The results for $\sigma = 4$ are shown in Fig. 4.10. We allow t_{b_2} to drop from 90% to 10% and for each value of t_{b_2}, t_{a_2} goes from 5% to t_{b_2} in steps of 5%. When the transmittances of the two idler modes are equal, the amount of entanglement is close to maximal, given by $\log_2(5) \approx 2.32$, which we expect in the light of the discussion in Subsection 4.3.1. As the symmetry is broken, entanglement decreases. In fact, Eq. (4.36) gives a very good analytical approximation even in this more general case, showing that the entanglement depends only on the relative transmittance $\epsilon = \frac{t_a}{t_b}$. This is verified numerically in Fig. 4.9 for $t_b = 65\%$.

We conclude that symmetric channels are not necessary to distribute near-maximally entangled states.

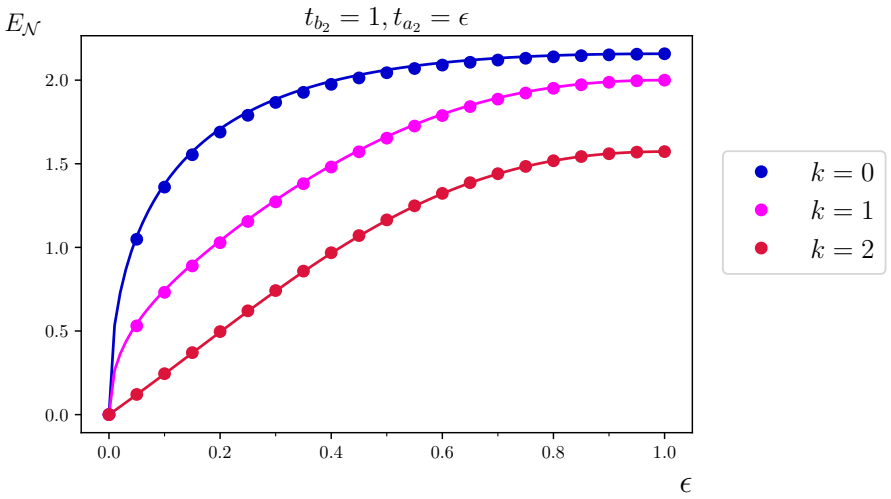

Figure 4.8: Dependence of the logarithmic negativity $E_{\mathcal{N}}$ shown in Fig. 4.7 on imbalance of losses in the two idler modes, $\epsilon = \frac{t_a}{t_b}$, for $g = 0.1$ and $\sigma = 4$. The points are the exactly calculated numerical results, while the solid lines are calculated from the analytical approximation Eq. (4.36). We note a good agreement between the numerical results and the analytical approximation.

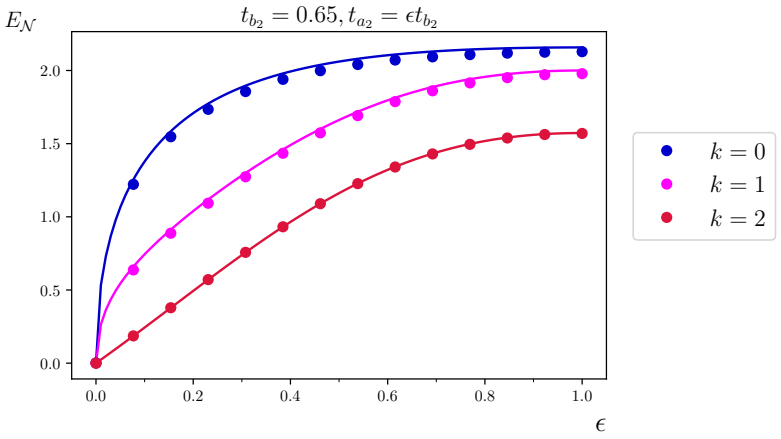

Figure 4.9: Dependence of logarithmic negativity $E_{\mathcal{N}}$ shown in Fig. 4.7 on imbalance of losses in the two idler modes, $\epsilon = \frac{t_a}{t_b}$, for $g = 0.1$, $\sigma = 4$ and $t_b = 65\%$. The points are the exactly calculated numerical results, while the solid lines are calculated from the analytical approximation Eq. (4.36). We note that the analytical approximation works even for the more general case when $t_b \neq 100\%$.

4.5 Losses in the signal modes

In contrast to the idler mode losses, losses in the signal modes a_1 and b_1 are critical since they spoil the generated entanglement, as can be seen in Fig. 4.11. There, idler losses were assumed lossless and only detection inefficiencies at Charlie's were taken into account. The reason for this sensitivity of the signal modes to losses is the lack of an entangling measurement.

To our benefit, losses in the signal modes may be significantly reduced by employing a delayed-choice scheme. In such a scheme, Alice and Bob perform their measurements immediately after generating the state ρ_{in} while the idler modes are still in flight. By the

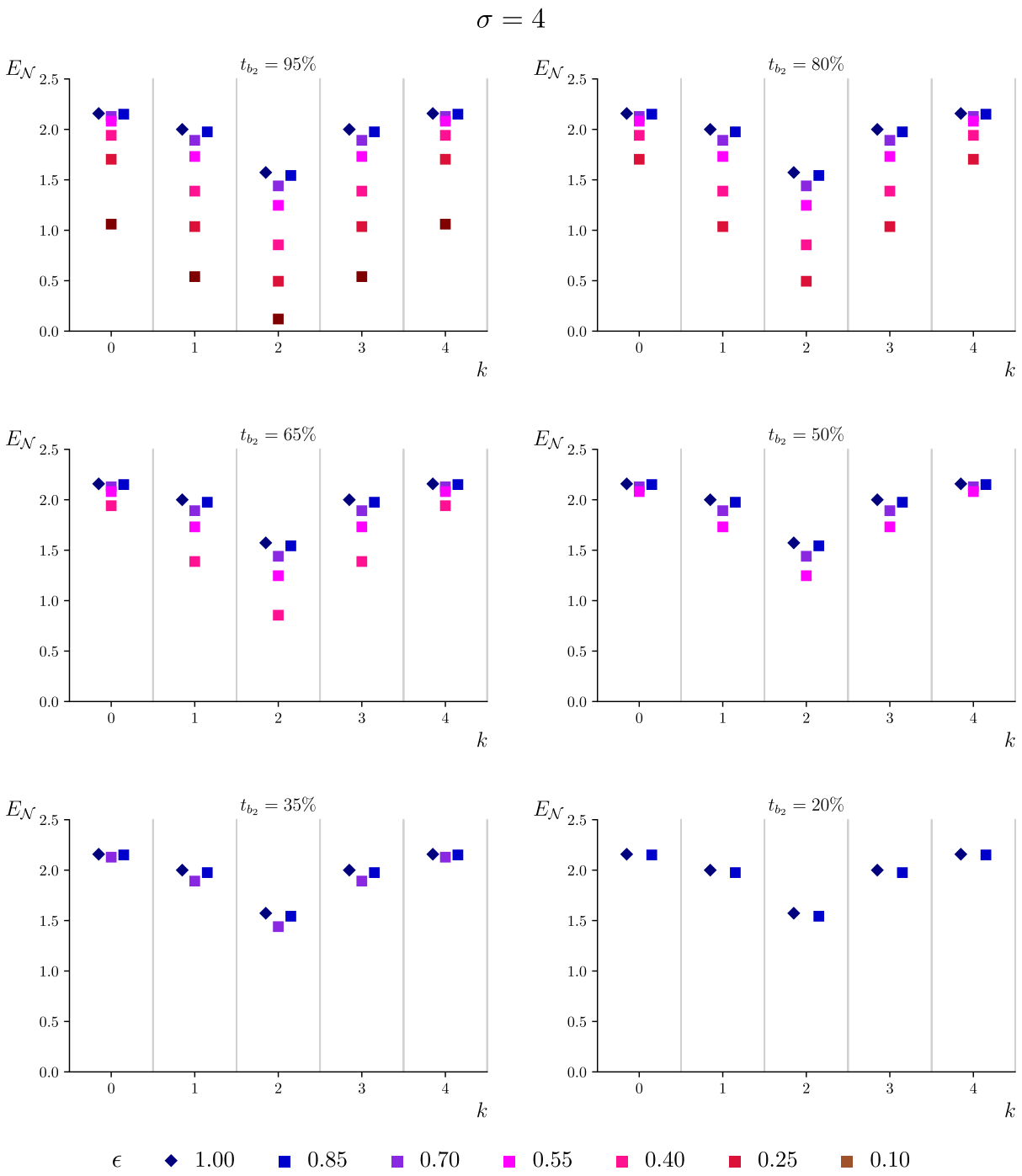

Figure 4.10: Logarithmic negativity $E_{\mathcal{N}}$ as a function of Charlie's measurement outcome $k, \sigma - k$. The results were computed for $g = 0.1$, $\sigma = 4$ and different pairs of transmittances of the idler modes as shown by the top label of each subfigure and the colour coding for ϵ. This is another demonstration that the entanglement shared between Alice and Bob is robust for small asymmetries ($\epsilon \gtrsim 0.7$) but this time for a wider range of Bob's transmissivities which vary between 95% and 20%.

no-signalling principle, all measurement outcomes are independent of this modification and the protocol maintains its properties.

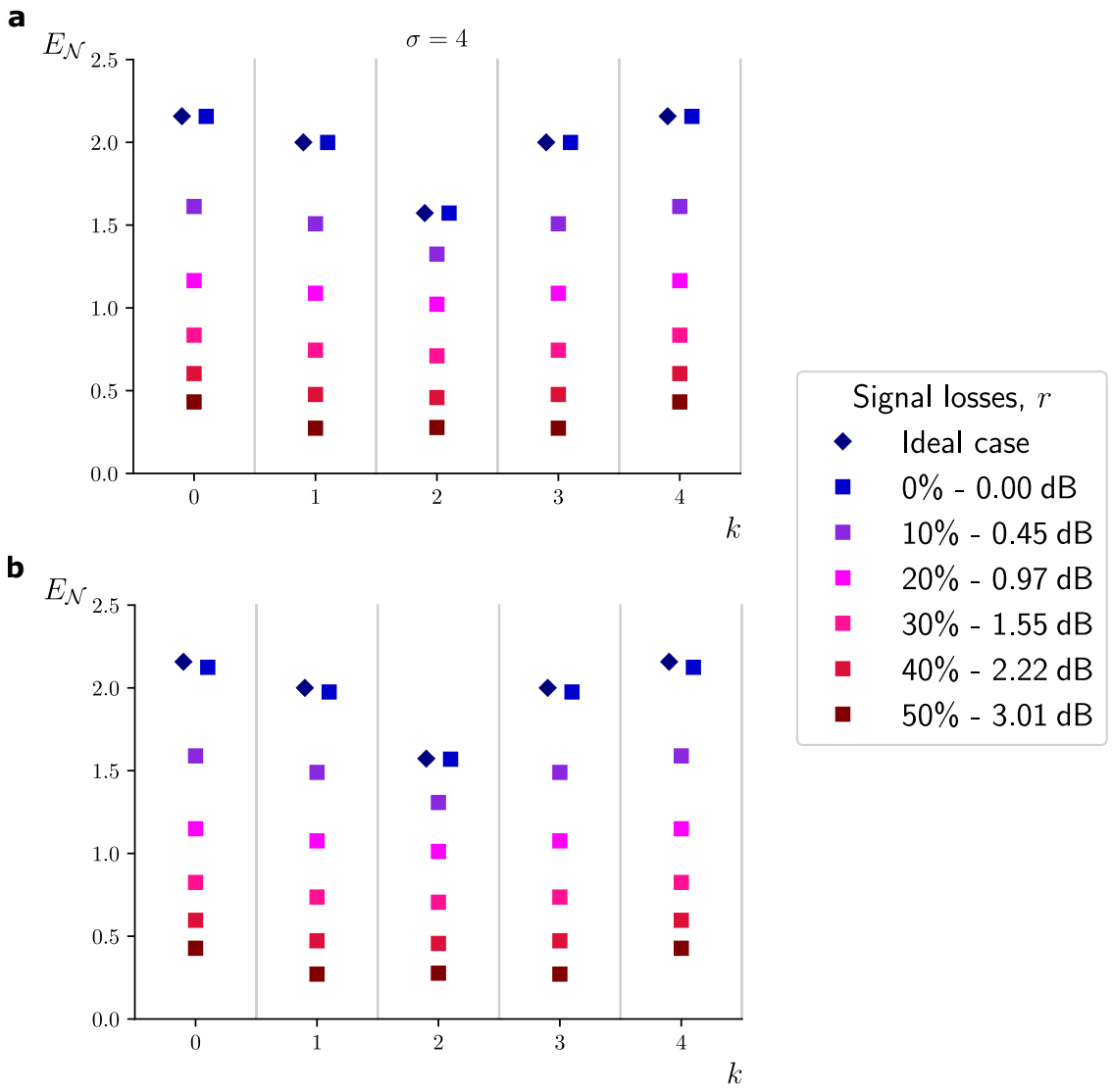

Figure 4.11: Logarithmic negativity $E_{\mathcal{N}}$ as a function of $k, \sigma - k$ computed for $g = 0.1$ and $\sigma = 4$ assuming symmetric losses in signal modes a_1 and b_1 and losses at the detectors located behind the beam splitter set to **a)** 5% and **b)** 40%. The losses at the idler modes are set to zero. We observe the amount of entanglement shared between Alice and Bob drops quickly in the presence of losses in the signal modes. However, this effect can be mitigated if the delayed choice scheme is employed.

4.6 Losses varying with time

It is also worth considering the effect of time fluctuations on the amount of entanglement shared by Alice and Bob. This is especially relevant in Earth-space quantum communications when photons travel through the atmosphere. The ever-changing atmospheric conditions, such as humidity and temperature, affect the transmissivity experienced by the travelling photons.

Ref. [108] discusses the difficulties in Earth-space communications and it establishes that losses in each transmitting mode will vary on the timescale of 10-100 ms for losses coming from atmospheric turbulence and 0.1-1 s for losses deriving from jitter in the telescopes. In comparison, a single pulse travelling towards a satellite on a low-Earth orbit will take approximately 3 ms to reach the satellite. Therefore fluctuations affect only the logarithmic negativity which is time-averaged over all successful transmission events representing the average amount of entanglement Alice and Bob share.

Let us assume that the transmittance of Alice's mode is fixed and Bob's has a normal distribution with variance 1 dB. We then generate 500 random values from that distribution and calculate the resulting logarithmic negativity. We repeat the process for different values of transmittance t_{a_2}. An example is shown in Fig. 4.12 for $\sigma = 4$ and typical atmospheric attenuation of 40 dB. It can be seen that the averaged value of logarithmic negativity is only 0.01-0.05 below the maximal value and the fluctuations do not have a significant impact on the performance of the distribution protocol.

4.7 Protocol success rate

In order to fairly compare our protocol against the state-of-the-art schemes, it is instructive to calculate its success rate. To start with, we follow a similar procedure as in Subsection 4.2.2 to find the efficiency in the presence of losses.

In the case of symmetric losses in the idler modes, the input state is as given in Eq. (4.14). The probability of measuring $k, \sigma - k$ is similarly given by

$$p_{(k,\sigma)} = \mathrm{Tr}_{a_1,b_1}\left\{\langle k, \sigma - k|_{a_2,b_2}\, \mathcal{U}_{\mathrm{BS}}\rho_{\mathrm{in}}\mathcal{U}_{\mathrm{BS}}^{\dagger}\, |k, \sigma - k\rangle_{a_2,b_2}\right\}. \tag{4.37}$$

The state inside the trace is in fact the output state $\rho_{\mathrm{out}}^{(k,\sigma)}$ (Eq. (4.23)). The trace of a density matrix is equivalent to its normalization constant. Therefore $\frac{1}{\tilde{\mathcal{N}}}$ from Eq.(4.24) (multiplied by the factor $\frac{(1-r)^{\sigma}}{\cosh^2 g}$ we absorbed during the derivation) gives the probability we are looking for

$$p_{(k,\sigma)} = \mathrm{Tr}_{a_1,b_1}\left\{\rho_{\mathrm{out}}^{(k,\sigma)}\right\} = \frac{1}{\tilde{\mathcal{N}}^2}\frac{(1-r)^{\sigma}}{\cosh^2 g} = \frac{\lambda_{\sigma}}{\cosh^2 g}\cdot\frac{(1-r)^{\sigma}}{(1-r\tanh^2 g)^{\sigma+2}} \tag{4.38}$$

which correctly reduces to Eq. (4.12) in the lossless case $r = 0$.

The protocol success rate is proportional to the probability of receiving at least one photon at the remote station, as then we are certain that Alice and Bob share entangled states, which may be multi-photon. The complement of that event is that no photons reach the satellite, equivalent to $\sigma = 0$. Setting $\sigma = 0$ in Eq. (4.38) we find

$$\begin{aligned} p_{(0,0)} &= \frac{1}{\cosh^4 g}\cdot\frac{1}{\left(1-r\tanh^2 g\right)^2} \\ &= \left(\frac{1-\tanh^2 g}{1-r\tanh^2 g}\right)^2. \end{aligned}$$

The equivalent expression in the case of asymmetric losses is calculated for ρ_{in} given

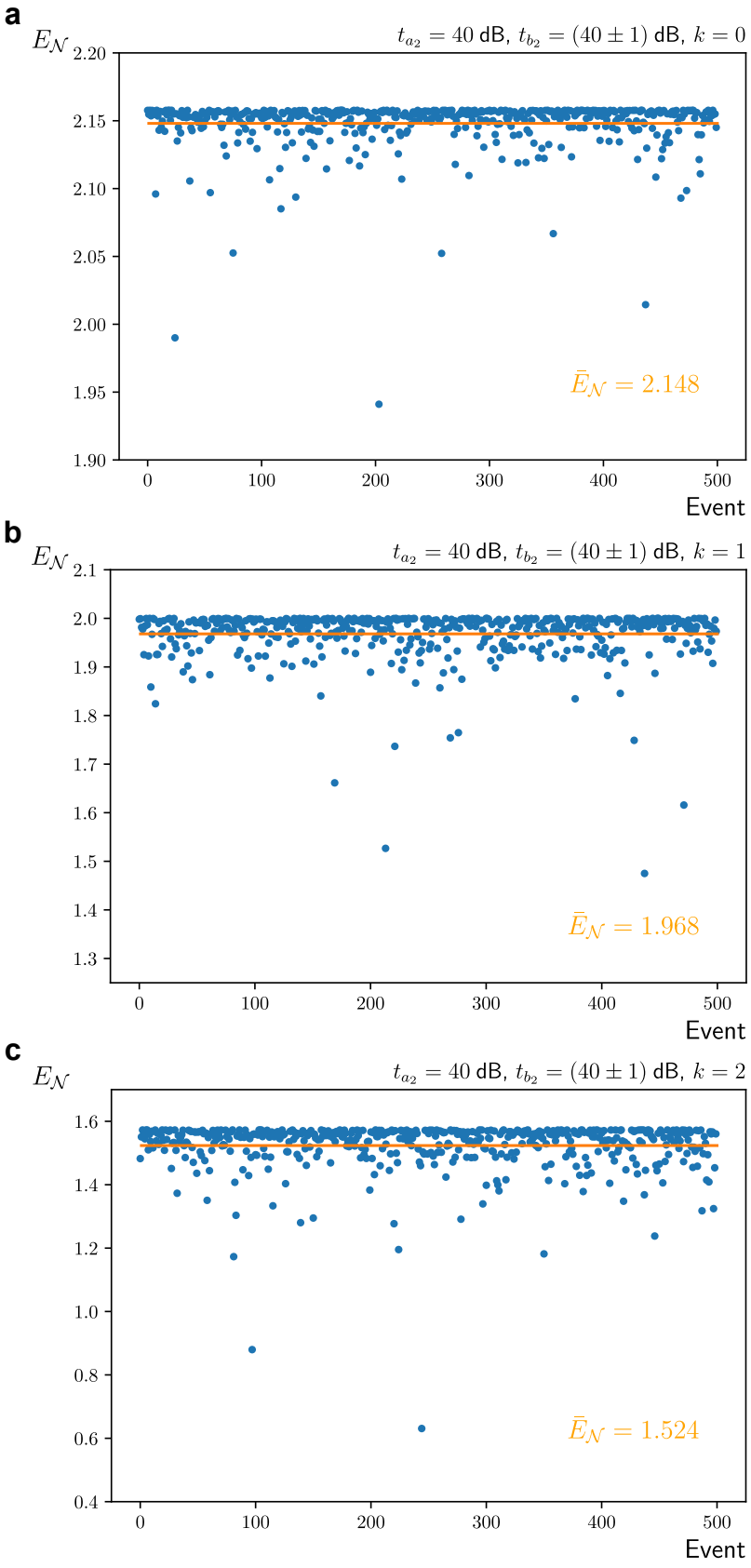

Figure 4.12: Randomly generated values of logarithmic negativity $E_{\mathcal{N}}$ for the state $\rho_{\text{out}}^{(k,\sigma)}$ in 500 events. The results were calculated for $g = 0.1, \sigma = 4$, Alice's idler mode transmissivity fixed to 40 dB and Bob's transmissivity at 40 dB with 1 dB variance. The subfigures show results for Charlie measuring **a)** $k = 0$, **b)** $k = 1$, and **c)** $k = 2$ at his station.

by Eq. (4.27) as follows

$$\begin{aligned} p_{(0,0)} &= \mathrm{Tr}_{a_1,b_1}\left\{ \langle 0,0|_{a_2,b_2}\, \rho_{\mathrm{in}}\, |0,0\rangle_{a_2,b_2} \right\} \\ &= \sum_{n,m=0}^{\infty} \lambda_n \lambda_m r_a^n r_b^m \\ &= \sum_{n=0}^{\infty} \lambda_n r_a^n \sum_{m=0}^{\infty} \lambda_m r_b^m \\ &= \frac{1}{\cosh^4 g} \cdot \frac{1}{1 - r_a \tanh^2 g} \cdot \frac{1}{1 - r_b \tanh^2 g}. \end{aligned} \tag{4.39}$$

The overall success rate is then $f_{\mathrm{rep}}(1 - p_{(0,0)})$. For a typical parametric gain ($g = 0.1$) and Earth-space losses ($r_a = r_b = 40\,\mathrm{dB}$) we obtain $1 - p_{(0,0)} = 2 \times 10^{-6}$. Assuming a pulse repetition rate of 80 MHz, our success rate would be 160 Hz, i.e. 160 entangled states generated per second.

Fig. 4.13 shows the dependence of the protocol efficiency on the idler losses (dashed lines) for three values of the parametric gain: $g = \{0.1, 0.2, 0.4\}$. We observe that the efficiency increases with the parametric gain g and decreases with the idler losses r. Investigating the dependence on transmission losses more closely, we see that it is proportional to the transmittance $t = 1 - r$ between Alice/Bob and Charlie. It is customary to instead use the transmittance $\eta = t^2$ of the summed distance from Alice to Bob [111], assuming that Charlie is approximately at the mid-point between them. In this context it is clear that our protocol's efficiency scales as $O(\sqrt{\eta})$. This should be contrasted to schemes where Charlie directly distributes Bell pairs to Alice and Bob [97, 100], which have efficiencies $O(\eta)$. The reason for the quadratic improvement is that only a single photon has to survive the trip between Alice/Bob and Charlie, since an entangled state is established even with $\sigma = 1$. In contrast, distributing a Bell pair requires two photons to survive the trip, therefore losses are more significant.

Fig. 4.13 depicts also the generated entanglement as a function of the idler losses for the same values of the parametric gain: $g = \{0.1, 0.2, 0.4\}$. Provided that $g^2 \ll 1$, which holds true for $g = 0.1$, the idler losses influence only the efficiency of the protocol without changing its principle of operation or the generated entanglement. This feature is characteristic to protocols based on two-photon Bell pair entanglement, and now we have shown it for all multi-photon schemes based on our set-up. If g is increased, the amount of entanglement decreases but not catastrophically, e.g. fo $g = 0.4$ the entanglement reduces to $\sim 60\%$ of the ideal value, with arbitrarily high idler losses. This reduction in entanglement occurs due to the presence of multi-photon components $S > \sigma$ demonstrating that even with a detection of $\sigma = 1$ at the remote station, the resulting state contains noticeable multi-photon components.

We conclude that there is a trade-off between the efficiency of the protocol and the generated entanglement. The efficiency can be improved by increasing g but at the cost of reducing the generated entanglement, as can be seen for $g = 0.2$ and $g = 0.4$.

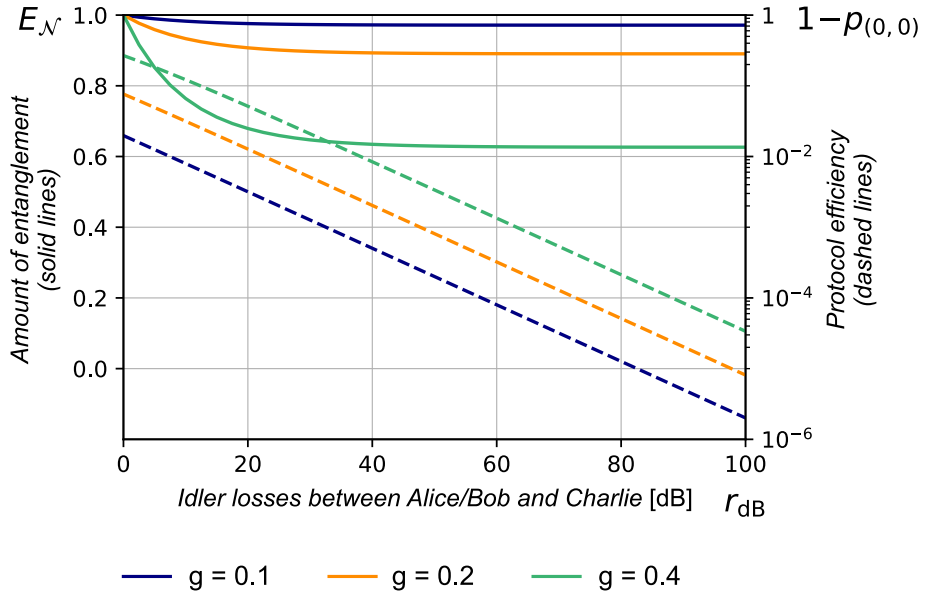

Figure 4.13: The performance of the entanglement distribution protocol is quantified by the amount of generated entanglement, as measured by the logarithmic negativity $E_{\mathcal{N}}$ (solid lines) and the protocol efficiency, $1 - p_{(0,0)}$ (dashed lines), plotted here for the example state $\rho_{\mathrm{out}}^{(0,1)}$. The idler losses between Alice/Bob and Charlie are expressed in dB, $r_{\mathrm{dB}} = -10 \log_{10}(1 - r)$. The protocol efficiency decreases gradually with idler losses, having the favourable scaling $O(\sqrt{\eta})$ where $\eta = (1 - r)^2$ is the effective transmittance between Alice and Bob. Charlie is assumed to be approximately at the mid-point between them. The amount of generated entanglement also decreases with idler losses, but quickly saturates to a finite value. Provided that the parametric gain g is at realistically low levels ($g^2 \ll 1$), this decrease is negligible and the protocol is robust to extremely high losses (blue lines, $g = 0.1$). Increasing the parametric gain (orange lines, $g = 0.2$ and green lines, $g = 0.4$) leads to an increase of protocol efficiency at the cost of reduced entanglement of the generated states.

4.8 Other factors in realising a feasible entanglement distribution protocol

The robustness to extreme losses of our protocol makes it ideal for deployment in a satellite-based quantum communications scheme where entanglement is distributed between two remote locations on Earth and employed for quantum key distribution. Our protocol has the potential to outperform state-of-the-art demonstrations based on the distribution of two-photon Bell pairs, such as those reported in Refs. [97] and [100]. There, an SPDC source pumped by a continuous wave laser generated space-borne Bell pairs at random times, which were next sent by a downlink channel to two stations on Earth separated by nearly 1200 km. The entanglement between the stations was verified by a CHSH Bell test under the fair sampling hypothesis. Moreover, only approximately two Bell pairs out of 5.9×10^6 reached the stations per second. The receiving stations had to be synchronised by the beacon laser and classical two-way communication between Alice and Bob was necessary to discard the cases when only one of the stations received a photon.

In contrast, in our protocol both Alice and Bob create locally a TMSV state. Their sources can be synchronised offline similarly to entanglement swapping schemes. A third party, Charlie, is located on a satellite and performs conditional state preparation. He acts as a central authority who broadcasts via a classical downlink if Alice and Bob share an entangled state. Thus direct communication between Alice and Bob is not required to generate the entanglement, although if the protocol was used for quantum key distribution, some one-way communication would still be necessary to perform information reconciliation. More importantly, in a satellite-based approach, the improved scaling $O(\sqrt{\eta})$ is significant. For example, in Ref. [100], two Bell pairs reach the ground stations per second, whereas for similar atmospheric losses (40 dB between ground and satellite, 80 dB summed losses) and $g = 0.1$ in our scenario, we estimate 160 successful entangled states to be generated per second.

This protocol, when applied to an Earth-space environment, is also original in that it uses an uplink rather than a downlink to send the quantum optical signals. Although downlinks have been shown to introduce less loss than uplinks [108], from an experimental point of view uplinks provide better control and flexibility of the quantum source when it is located on the ground rather than in space, and thus are the better choice to study global-scale quantum communications implementations [108]. Turbulence and background radiation affect uplinks more significantly, however, the pointing accuracy is a more consequential factor in our scheme, due to the necessity of time synchronisation of the ground sources. In this aspect uplinks have in fact been shown to be more precise [108].

Another matter to address in Earth-space quantum communications is the problem of phase stability. A phase damping channel causes the off-diagonal elements of the two-mode density matrix $\rho_{\text{out}}^{(k,\sigma)}$ to decay, lowering the entanglement. This effect is, however, mitigated by the delayed-choice scheme in which Alice and Bob measure the signal modes while the idler beams are still in flight. The idler beams are then projected onto Fock states and additional phase damping may be further reduced by using two reference pulses, one to measure the delay in arrival times of the two idler beams, and one to measure the rate of phase-shifting, as has been done in previous experiments [112, 113, 114].

4.9 Software

In this section we briefly mention the procedure used to calculate the logarithmic negativity of $\rho_{\text{out}}^{(k,\sigma)}$, which is the basis of all our calculations in this chapter. The software that we have developed and used was written in Python 3 using the NumPy package, which was employed for matrix algebra. The program performs operations described by the following algorithm

1. for both SPDC sources belonging to Alice and Bob, compute $\rho = |\Psi\rangle\langle\Psi|$ where, $|\Psi\rangle = \sum_{n=0}^{n_{\max}} \sqrt{\lambda_n}\,|n,n\rangle$, and $n_{\max}$ is a sum cutoff found by solving $\lambda_{n_{\max}}/\lambda_0 < 10^{-15}$ for a given g and 10^{-15} results from the precision of the numeric data type; usually $n_{\max} \geq 6$.

2. for all modes leaving the sources, add losses and then trace out unwanted modes, i.e. perform the following operation

$$\rho' = \text{Tr}_{3,4}\left\{U_{\text{BS}}^{(r_s)}\,U_{\text{BS}}^{(r_i)}\,|\Psi\rangle\langle\Psi|\left(U_{\text{BS}}^{(r_i)}\right)^{\dagger}\left(U_{\text{BS}}^{(r_s)}\right)^{\dagger}\right\},$$

   where r_s and r_i are losses in signal and idler modes, respectively,

3. construct the density operator matrix for $\rho_{\text{in}} = \rho' \otimes \rho'$,

4. apply the $50:50$ BS operation, $\rho_{\text{BS}} = U_{\text{BS}}\,\rho_{\text{in}}\,(U_{\text{BS}})^{\dagger}$,

5. add losses r_{d_1} and r_{d_2} to the modes leaving the BS

$$\rho_{\text{out}} = \text{Tr}_{5,6}\left\{U_{\text{BS}}^{(r_{d_1})}U_{\text{BS}}^{(r_{d_2})}\rho_{\text{BS}}\left(U_{\text{BS}}^{(r_{d_2})}\right)^{\dagger}\left(U_{\text{BS}}^{(r_{d_1})}\right)^{\dagger}\right\},$$

6. for all $k = 0,\ldots,S$ perform the following operations:

   (a) project ρ_{out} onto $|k,S-k\rangle$: $\rho_{\text{out}}^{(k,S)} = \langle k,S-k|\,\rho_{\text{out}}\,|k,S-k\rangle$ and renormalize the result,

   (b) compute partial transposition of $\rho_{\text{out}}^{(k,S)}$: $\left(\rho_{\text{out}}^{(k,S)}\right)^{\Gamma}$,

   (c) compute eigenvalues $\{\alpha_k\}$ of $\left(\rho_{\text{out}}^{(k,S)}\right)^{\Gamma}$ using routines built into the NumPy package,

   (d) compute the logarithmic negativity

$$E_{\mathcal{N}} = \log_2\left(1 + 2\sum_k \frac{|\alpha_k| - \alpha_k}{2}\right).$$

The advantage of the above algorithm is relatively fast operation at a cost of huge memory requirements because of the large size of the matrices. In the worst case, ρ_{out} contains $n_{\max}^8$ double-precision values (ca. 13 MB for $n_{\max} = 6$, 800 MB for $n_{\max} = 10$) and therefore, computations for $n_{\max}$ as large as 20 or 50 would be impossible. This has been solved by noticing that the matrix contains mostly zeros and that the sum of the number of photons in all modes cannot be simultaneously higher than $4n_{\max}$, which allowed us to apply denser packing. Once the final density operator matrix is computed, subsequent computations (step 6) of the algorithm can be performed for all interesting values of S and k.

4.10 Conclusions

We proposed an entanglement distribution protocol based on an optimal use of the existing integrated quantum optical components, namely SPDC sources and PNR detectors. An experiment in which our family of states was successfully produced has been reported in Ref. [115] manifesting the feasibility of our protocol.

We predict to be able to distribute near-maximally entangled states with arbitrarily large losses in the transmitting channels, whether it is an Earth-space channel or a long optical fibre. In particular, we have carefully studied the effect of imperfections that would be present within an actual Earth-space entanglement distribution implementation. We have considered idler losses, signal losses, detector inefficiencies, idler asymmetry, fluctuations of idler losses over time, time synchronisation errors and phase damping to ensure our protocol is feasible. We also discussed the pros and cons of using an uplink versus a downlink scenario. These realistic parameters allowed us to simulate the outcome of an entanglement distribution experiment which achieved a success rate of 160 Hz.

The distinctive features of our protocol include robustness to arbitrarily high transmission losses, ability of choosing the local dimension of the generated multi-photon entangled state and the state-of-the-art scaling $O(\sqrt{\eta})$ of efficiency with channel transmittance. We demonstrated that our protocol is capable of achieving a quadratic improvement in transmission rates compared to the distribution of polarization-entangled photon pairs, such as in the recently deployed Earth-space setup [100], regardless of transmission losses.

Further work [116, 117, 118] shows that the entanglement distributed with our protocol can be certified by Bell tests which have the potential to be loophole free, and may be directly used in well established QKD protocols. Generally, this could provide measurement-device-independent (MDI) levels of security, which may be upgraded to fully device-independent (DI) security if the Bell test was loophole-free.

Chapter 5

Quantum-enhanced interferometry

The entanglement distribution protocol described in the previous chapter can also be used to generate higher photon-number states which are useful for quantum metrology. They are the multi-photon generalised Holland-Burnett states [73] that we show allow near-optimal quantum-enhanced optical phase estimation in a lossy environment. This chapter is based on Ref. [119] and it also contains selected results from an experimental realisation of this idea carried out by my co-authors.

We will start with some background information on parameter estimation, then proceed to discuss the current state of the art and finally present the theoretical and experimental results of applying the entanglement distribution protocol to quantum-enhanced interferometry.

5.1 Background

Quantum metrology is a relatively new quantum technology which has emerged in the last two decades as a result of the second quantum revolution [120]. It has found a number of applications, in particular in optics, where it helps to enhance the performance of interferometers [121, 122], phase estimation [123], object detection and testing [124, 125], superresolution [126, 127] and spectroscopy [128]. Quantum enhanced schemes are particularly exciting when applied to optical interferometers, making them the most sensitive instruments we dispose of nowadays. In fact, quantum-enhanced optical interferometers enabled the long-awaited detection of gravitational waves in experiments such as GEO600 [129], LIGO [130] and VIRGO [131]. They also allow characterization of delicate photosensitive samples [132, 133, 134, 135].

Classically, interferometry is the observation of light intensity variations resulting from two (or more) waves overlapping and their relative phase changing, where light intensity is considered to be measureable with arbitrary precision. However, once semiclassical theory is considered, which implies a quantized measurement process, the absorption of light quanta becomes stochastic. The number of photons detected follows Poissonian or super-Poissonian statistics with standard deviation proportional to or larger than $\sqrt{\langle N\rangle}$ where $\langle N\rangle$ denotes the mean number of photons detected. This uncertainty is then carried onto the determination of the relative phase difference between the interferometer arms via $\Delta\phi \propto \frac{\Delta N}{\langle N\rangle} \geq \frac{1}{\sqrt{\langle N\rangle}}$. The equality holds for Poissonian light and is referred to as the shot noise.

In a fully quantum approach, light is described by a quantum state and exhibits non-classical effects such as entanglement or squeezing. Such states may follow sub-

Poissonian statistics where the photon-number fluctuations are reduced, also leading to reduced fluctuations of the relative phase. Thus the shot noise is not a fundamental bound and can be overcome with appropriately chosen states of light and measurement strategies. A fundamental bound is instead given by the so-called Heisenberg limit, which refers to the relative phase difference scaling with $\frac{1}{N}$. The tools to find the optimal setups are given by the classical [136] and quantum estimation theories [137, 138]. Their basics are reviewed below.

5.1.1 Classical parameter estimation

Classical parameter estimation looks into the most efficient ways of extracting information from a dataset collected in a non-deterministic process.

The dataset is an N-point set of independent identically distributed random variables, $\mathbf{x} = (x_1, x_2, \ldots, x_N)$, each distributed according to a common probability distribution function (PDF), $p_\phi(\mathbf{x}) = p_\phi(x_1) \ldots p_\phi(x_N)$, that depends on a parameter ϕ we wish to determine. The prediction of what the parameter ϕ is, based on the dataset $\mathbf{x}$, is given by a function called the *estimator* $\tilde{\phi}(\mathbf{x})$. The quality of the estimator can be quantified by the Mean Square Error (MSE) deviation of the estimator from the true value of the parameter ϕ

$$\Delta\tilde{\phi}(\mathbf{x}) = \left\langle \left(\tilde{\phi}(\mathbf{x}) - \phi\right)^2 \right\rangle = \int \mathrm{d}\mathbf{x}\, p_\phi(\mathbf{x}) \left(\tilde{\phi}(\mathbf{x}) - \phi\right)^2. \tag{5.1}$$

A desirable property of the estimator is that it is unbiased

$$\langle\tilde{\phi}\rangle = \int \mathrm{d}\mathbf{x}\, p_\phi(\mathbf{x})\tilde{\phi}(\mathbf{x}) = \phi, \tag{5.2}$$

which means that on average it will yield the true parameter value. This is equivalent to the condition that

$$\frac{\partial}{\partial\phi}\langle\tilde{\phi}\rangle = 1. \tag{5.3}$$

Ideally, we would want the estimator to be unbiased for all ϕ. However, this is not always the case and we must often contend with a locally unbiased estimator at a priorly known value ϕ_0. The local unbiasedness condition is easier to satisfy and takes the following modified form

$$\frac{\partial}{\partial\phi}\langle\tilde{\phi}\rangle\bigg|_{\phi=\phi_0} = 1. \tag{5.4}$$

Once the estimator is unbiased, it is possible to construct a so-called Cramér-Rao (CR) bound which lower-bounds the MSE

$$\Delta^2\tilde{\phi} \geq \frac{1}{\mathcal{F}}, \tag{5.5}$$

where $\mathcal{F}$ is the Fisher Information (FI) defined by these three equivalent formulas

$$\mathcal{F} = \int \mathrm{d}x \frac{1}{p_\phi(x)} \left(\frac{\partial p_\phi(x)}{\partial\phi}\right)^2 = \left\langle \left(\frac{\partial}{\partial\phi}\ln p_\phi(x)\right)^2 \right\rangle = -\left\langle \frac{\partial^2}{\partial\phi^2}\ln p_\phi(x) \right\rangle. \tag{5.6}$$

From the CR bound we establish that the bigger the FI, the better precision of estimating ϕ can be expected. In the literature, an estimator which saturates the CR bound is called *efficient.*

The FI has an important property. It is additive for product distributions such as $p_\phi(\mathbf{x})$, i.e. uncorrelated events. Let us consider a distribution $p_\phi(x_1, x_2) = p_\phi(x_1)p_\phi(x_2)$. Then, using the last expression in Eq. (5.6), we have

$$\begin{aligned}\mathcal{F}^{(1,2)} &= -\left\langle \frac{\partial^2}{\partial\phi^2} \ln p_\phi(x_1, x_2) \right\rangle = -\left\langle \frac{\partial^2}{\partial\phi^2} \ln \left(p_\phi(x_1)p_\phi(x_1)\right) \right\rangle = \\ &= -\left\langle \frac{\partial^2}{\partial\phi^2} \ln p_\phi(x_1) \right\rangle - \left\langle \frac{\partial^2}{\partial\phi^2} \ln p_\phi(x_2) \right\rangle = \mathcal{F}^{(1)} + \mathcal{F}^{(2)}.\end{aligned} \tag{5.7}$$

In particular, $\mathcal{F}^{(N)} = N\mathcal{F}$, where $\mathcal{F}$ is the FI for a single random variable.

5.1.2 Quantum parameter estimation

The quantum parameter estimation theory is constructed in a similar fashion to the classical one. Here, the parameter ϕ is encoded in the quantum state ρ_ϕ, which is measured repeatedly to yield, according to the Born rule, the probability density function $p_\phi(x) = \mathrm{Tr}\left\{\rho_\phi M^{(x)}\right\}$, where $M^{(x)}$ is either the standard von Neumann projective measurement or, more generally, a positive operator-valued measure (POVM) with outcome x. The estimation of the parameter based on the measurement outcome is given by an estimator function $\tilde{\phi}(x)$.

In order to find the most optimal solution regardless of the measurement scheme, it is useful to construct a lower bound of the MSE minimised over all conceivable measurements. This is given by the quantum Cramér-Rao (q-CR) bound which is a generalisation of the classical CR bound

$$\Delta^2\tilde{\phi} \geq \frac{1}{Q(\rho_\phi)}, \tag{5.8}$$

where Q is the quantum Fisher information (QFI)

$$Q(\rho_\phi) = \mathrm{Tr}\left\{\rho_\phi \Lambda(\rho_\phi)^2\right\}, \tag{5.9}$$

and $\Lambda(\rho_\phi)$ is the symmetric logarithmic derivative (SLD) defined implicitly for an arbitrary state via

$$\dot{\rho}_\phi = \frac{1}{2}\left(\rho_\phi\Lambda(\rho_\phi) + \Lambda(\rho_\phi)\rho_\phi\right), \tag{5.10}$$

where $\dot{\rho}_\phi = \frac{\mathrm{d}\rho_\phi}{\mathrm{d}\phi}$. A solution for the SLD can be obtained when working in the eigenbasis of the measured quantum state, $\rho_\phi = \sum_i \lambda_i(\phi)|e_i(\phi)\rangle\langle e_i(\phi)|$

$$\Lambda(\rho_\phi) = \sum_{i,j} \frac{2\langle e_i(\phi)|\dot{\rho}_\phi|e_j(\phi)\rangle}{\lambda_i(\phi) + \lambda_j(\phi)} |e_i(\phi)\rangle\langle e_j(\phi)|, \tag{5.11}$$

where the sum is taken over the terms with non-vanishing denominator.

For pure states, $\rho_\phi = |\Psi_\phi\rangle\langle\Psi_\phi|$ and the SLD becomes

$$\Lambda\left(|\Psi_\phi\rangle\right) = 2\left(|\dot{\Psi}_\phi\rangle\langle\Psi_\phi| + |\Psi_\phi\rangle\langle\dot{\Psi}_\phi|\right), \tag{5.12}$$

where we used the fact that $\frac{\mathrm{d}}{\mathrm{d}\phi}\left(|\Psi_\phi\rangle\langle\Psi_\phi|\right) = |\dot{\Psi}_\phi\rangle\langle\Psi_\phi| + |\Psi_\phi\rangle\langle\dot{\Psi}_\phi|$ and $|\dot{\Psi}_\phi\rangle = \frac{\mathrm{d}|\Psi_\phi\rangle}{\mathrm{d}\phi}$.

The QFI simplifies then to

$$\begin{aligned} Q\left(|\Psi_\phi\rangle\right) &= \mathrm{Tr}\left\{|\Psi_\phi\rangle\langle\Psi_\phi|\Lambda^2(|\Psi_\phi\rangle)\right\} \\ &= \langle\Psi_\phi|\Lambda^2(|\Psi_\phi\rangle)|\Psi_\phi\rangle \\ &= 4\left(\langle\Psi_\phi|\dot{\Psi}_\phi\rangle^2 + \langle\dot{\Psi}_\phi|\Psi_\phi\rangle^2 + \left|\langle\Psi_\phi|\dot{\Psi}_\phi\rangle\right|^2 + \langle\dot{\Psi}_\phi|\dot{\Psi}_\phi\rangle\right) \\ &= 4\left(\langle\dot{\Psi}_\phi|\dot{\Psi}_\phi\rangle - \left|\langle\dot{\Psi}_\phi|\Psi_\phi\rangle\right|^2\right), \end{aligned} \tag{5.13}$$

where in the last step we observed that $\langle\Psi_\phi|\dot{\Psi}_\phi\rangle^2 + \langle\dot{\Psi}_\phi|\Psi_\phi\rangle^2 + \left|\langle\Psi_\phi|\dot{\Psi}_\phi\rangle\right|^2 = -\left|\langle\dot{\Psi}_\phi|\Psi_\phi\rangle\right|^2$ since $\frac{\mathrm{d}}{\mathrm{d}\phi}\left(\langle\Psi_\phi|\Psi_\phi\rangle\right) = \langle\Psi_\phi|\dot{\Psi}_\phi\rangle + \langle\dot{\Psi}_\phi|\Psi_\phi\rangle = 0$.

Eq. (5.13) shows that the bigger the derivative $|\dot{\Psi}_\phi\rangle$, the higher the QFI and the more information is accessible in the state. However, the change in the state has to happen in the direction perpendicular to the state itself and this is why the component representing the change *in* the direction of the state reduces the total QFI.

As in the classical case, the QFI is additive and $Q^{(N)} = NQ$. Here, N could be the number of measurements taken or alternatively the number of copies of a single state, $\rho_\phi^{\otimes N}$.

QFI defines a metric in the space of quantum states which induces the so-called Bures distance [139]. The small change to the state as a result of an infinitesimal change of the parameter is equivalent to the state taking a path in the space of quantum states. The further apart the states are, the larger the QFI and hence the better distinguishability between the state before and after the phase shift.

It is also worth stressing that the QFI is independent of the chosen measurement strategy and therefore is a property of the state. As a result, the q-CR bound on the chosen parameter is fundamental and valid for arbitrary measurements and unbiased estimators. Therefore, the problem of saturating the q-CR bound is equivalent to finding the optimal measurement strategy which saturates the classical CR bound. This can be seen in what follows.

The POVM is the most general type of measurement with only two constraints, $M^{(x)} \geq 0, \int \mathrm{d}x M^{(x)} = \mathbb{1}$. From the corresponding probability density function $p_\phi(x) = \mathrm{Tr}\left\{\rho_\phi M^{(x)}\right\}$ we can calculate the associated classical FI

$$\begin{aligned} \mathcal{F} &= \int \mathrm{d}x \frac{1}{p_\phi(x)}\left(\frac{\partial p_\phi(x)}{\partial\phi}\right)^2 \\ &= \int \mathrm{d}x \frac{\left[\mathrm{Tr}\left\{\frac{\mathrm{d}\rho_\phi}{\mathrm{d}\phi}M^{(x)}\right\}\right]^2}{\mathrm{Tr}\left\{\rho_\phi M^{(x)}\right\}} \\ &= \int \mathrm{d}x \frac{\left[\mathrm{Tr}\left\{\frac{1}{2}\left(\rho_\phi\Lambda(\rho_\phi) + \Lambda(\rho_\phi)\rho_\phi\right)M^{(x)}\right\}\right]^2}{\mathrm{Tr}\left\{\rho_\phi M^{(x)}\right\}}. \end{aligned} \tag{5.14}$$

Since $\rho_\phi, \Lambda(\rho_\phi)$ and $M^{(x)}$ are all hermitian, we can use the identity $\mathrm{Tr}\left\{ABC + BAC\right\} = \mathrm{Tr}\left\{ABC + (ABC)^\dagger\right\} = 2\mathrm{Tr}\left\{\mathrm{Re}\{ABC\}\right\}$ for A, B, C hermitian. Eq. (5.14) then takes the form

$$\begin{aligned} \mathcal{F} &= \int \mathrm{d}x \frac{\left[\mathrm{Re}\left\{\mathrm{Tr}\left\{\rho_\phi\Lambda(\rho_\phi)M^{(x)}\right\}\right\}\right]^2}{\mathrm{Tr}\left\{\rho_\phi M^{(x)}\right\}} \\ &\leq \int \mathrm{d}x \frac{\left|\mathrm{Tr}\left\{\rho_\phi\Lambda(\rho_\phi)M^{(x)}\right\}\right|^2}{\mathrm{Tr}\left\{\rho_\phi M^{(x)}\right\}}, \end{aligned} \tag{5.15}$$

as the absolute value of a number will always be larger than or equal to its real part.

We now use the Cauchy-Schwarz inequality with respect to the Hilbert-Schmidt inner product $\left|\mathrm{Tr}\left\{AB^\dagger\right\}\right|^2 \leq \mathrm{Tr}\left(A^\dagger A\right)\mathrm{Tr}\left(B^\dagger B\right)$ to obtain, with $A = \sqrt{M^{(x)}}\sqrt{\rho_\phi}$ and $B = \sqrt{M^{(x)}}\Lambda(\rho_\phi)\sqrt{\rho_\phi}$,

$$\begin{aligned}
\mathcal{F} &\leq \int \mathrm{d}x \frac{\left|\mathrm{Tr}\left\{\sqrt{M^{(x)}}\sqrt{\rho_\phi}\sqrt{\rho_\phi}\Lambda(\rho_\phi)\sqrt{M^{(x)}}\right\}\right|^2}{\mathrm{Tr}\left\{\rho_\phi M^{(x)}\right\}} \\
&\leq \int \mathrm{d}x \frac{\mathrm{Tr}\left\{\sqrt{\rho_\phi}\sqrt{M^{(x)}}\sqrt{M^{(x)}}\sqrt{\rho_\phi}\right\}\mathrm{Tr}\left\{\sqrt{\rho_\phi}\Lambda(\rho_\phi)\sqrt{M^{(x)}}\sqrt{M^{(x)}}\Lambda(\rho_\phi)\sqrt{\rho_\phi}\right\}}{\mathrm{Tr}\left\{\rho_\phi M^{(x)}\right\}} \\
&= \int \mathrm{d}x \mathrm{Tr}\left\{\rho_\phi \Lambda(\rho_\phi) M^{(x)} \Lambda(\rho_\phi)\right\} \\
&= \mathrm{Tr}\left\{\rho_\phi \Lambda(\rho_\phi) \int \mathrm{d}x M^{(x)} \Lambda(\rho_\phi)\right\} \\
&= \mathrm{Tr}\left\{\rho_\phi \Lambda(\rho_\phi)^2\right\},
\end{aligned} \tag{5.16}$$

where in the last step we used the completeness property of the POVM.

We have therefore shown that

$$\mathcal{F} \leq Q, \tag{5.17}$$

and thus

$$\Delta^2\tilde{\phi} \geq \frac{1}{\mathcal{F}} \geq \frac{1}{Q}. \tag{5.18}$$

We can now infer that the best measurement strategy will lead to the classical FI coinciding with the QFI, $\mathcal{F} = Q$.

In the context of optical interferometry, the estimated parameter is often encoded by a unitary operator

$$\rho_\phi = \mathcal{U}_\phi \rho \mathcal{U}_\phi^\dagger, \tag{5.19}$$

where $\mathcal{U}_\phi = e^{-i\mathcal{H}\phi}$ with $\mathcal{H}$ the generating Hamiltonian. For pure states, $\rho = |\Psi\rangle\langle\Psi|$ and the QFI turns out to be proportional to the variance of the Hamiltonian, $\mathcal{H}$, with respect to the initial state

$$Q(|\Psi_\phi\rangle) = 4\Delta^2\mathcal{H} = 4\left(\langle\Psi|\mathcal{H}^2|\Psi\rangle - \langle\Psi|\mathcal{H}|\Psi\rangle^2\right). \tag{5.20}$$

which follows from Eq. (5.13) once $|\dot{\Psi}\rangle = -i\mathcal{H}|\Psi\rangle$ is substituted.

5.2 State of the art

We will now review the most recent findings in optical interferometry using definite photon-number states.

It is known that the best precision which scales with $1/N$ and thus reaches the Heisenberg limit is achieved by the highly entangled N00N states [140, 141, 142, 143, 144, 145, 146, 147, 148]. For these states $Q(\rho_{\mathrm{N00N}}) = N^2$ and hence $\Delta\tilde{\phi} \geq \frac{1}{N}$. Unfortunately, the N00N states are also vulnerable to decoherence, especially at large photon numbers. In practice, their enhanced sensitivity disappears in the presence of loss which may originate from interactions inside the interferometer (e.g. absorption in a sample) as well as external losses in the state preparation and detection [149]. Moreover, the difficulty in the

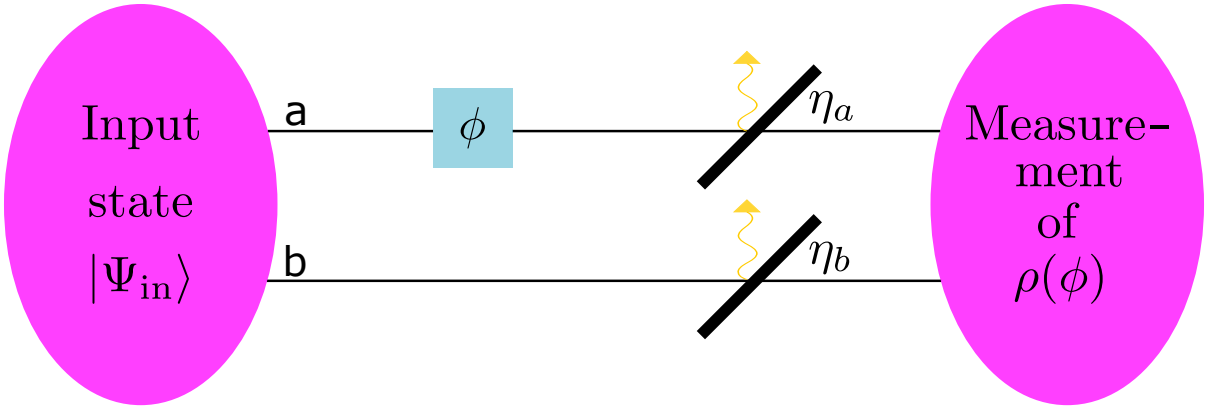

Figure 5.1: General optical interferometric scheme with two arms. Channel a acquires a phase ϕ relative to channel b. The two beam splitters represent photon losses.

preparation of N00N states increases dramatically with N. Only up to $N = 5$ states have been demonstrated experimentally so far [145].

Taking these facts into consideration, it is possible to engineer states that trade away sensitivity for loss-tolerance in order to achieve some advantage over classical limits even if Heisenberg scaling is no longer available [150, 151]. For example, squeezed light [152] and non-maximally entangled states such as Holland-Burnett states [73, 153, 154, 155, 156, 157, 158] can surpass classical limits despite some losses. In fact, squeezed light offers comparable performance to N00N states in loss-free scenarios and near-optimal performance in the presence of decoherence. However, these states are indefinite photon-numbered which makes them difficult to compare to in terms of the resources consumed – typically the number of photons in interferometry. The Holland-Burnett states are better, with $Q(\rho_{\text{HB}}) = N\left(\frac{N}{2}+1\right)$ and $\Delta\tilde{\phi} \geq \sqrt{\frac{2}{N(N+2)}}$, as they are definite photon-numbered. They quickly outperform N00N states as losses are added to the interferometer but at some point their performance also falls below the shot noise level.

In the next sections we will introduce novel probes which are more sensitive than both the Holland-Burnett and N00N states in the presence of loss and approximate the optimal performance for arbitrary losses once N00N states are no longer optimal.

5.3 Optimal states

A good reference point to the possible quantum enhancement a particular state can give, are the so-called optimal states. These states are the most general pure two-mode input states with definite photon number N [159]

$$|\Psi_{\text{opt}}\rangle = \sum_{n=0}^{N} \alpha_n |n\rangle_a |N-n\rangle_b, \tag{5.21}$$

whose coefficients α_n are optimised to yield the highest value of QFI and hence the best precision possible. A special case of these states are the N00N states which reach the Heisenberg limited precision in the lossless case and are given by $\alpha_n = 0$ for all $n \neq \{0, N\}$ and $|\alpha_0| = |\alpha_N| = \frac{1}{\sqrt{2}}$ in the representation above.

Eq. (5.21) also enables us to find states which are less sensitive but more robust in the presence of losses, representing a trade-off between precision and robustness. In the

most general interferometric scenario, the interferometer consists of two arms a and b and the channel a accumulates a phase ϕ relative to channel b. Both channels are subject to losses, which are modelled by beam splitters of transmissivity η_a and η_b for channels a and b respectively, and the output is measured by an arbitrary measurement. This setup is shown in Fig. 5.1.

The input state shown in Eq. (5.21) is modified by the losses according to

$$\begin{aligned}|n, N-n\rangle\langle n', N-n'| \to & \sum_{p=0}^{\min(n,n')} \sqrt{\binom{n}{p}\binom{n'}{p}\eta_a^{n+n'-2p}(1-\eta_a)^{2p}} \\ & \times \sum_{q=0}^{\min(N-n,N-n')} \sqrt{\binom{N-n}{q}\binom{N-n'}{q}\eta_b^{2N-n-n'-2q}(1-\eta_b)^{2q}} \\ & \times |n-p, N-n-q\rangle\langle n'-p, N-n'-q|,\end{aligned} \tag{5.22}$$

following the results of Section 3.2.4. Including the phase accumulation $|n, N-n\rangle \to e^{in\phi}|n, N-n\rangle$, the output density matrix takes the form

$$\rho(\phi) = \sum_j p_j |\Psi_j(\phi)\rangle\langle\Psi_j(\phi)|, \tag{5.23}$$

where

$$|\Psi_j(\phi)\rangle = \frac{1}{\sqrt{p_j}} \sum_{n=0}^{N} \alpha_n e^{in\phi} \sum_{p=0}^{n} \sum_{q=0}^{N-n} \sqrt{\mathcal{L}_{pq}^n}|n-p, N-n-q\rangle, \tag{5.24}$$

and $\mathcal{L}_{pq}^n = \binom{n}{p}\binom{N-n}{q}\eta_a^{n-p}(1-\eta_a)^p\eta_b^{N-n-q}(1-\eta_b)^q$ quantifies the reduction of the probability amplitude due to losses.

The states $|\Psi_j(\phi)\rangle$ are not necessarily orthogonal, but using the convexity of the QFI [159], it is possible to obtain an upper bound which takes the following form familiar from Eq. (5.20)

$$Q \leq \tilde{Q} = \sum_j p_j \Delta^2 \mathcal{H}_j, \tag{5.25}$$

where the variance on the Hamiltonian $\Delta^2\mathcal{H}_j$ is taken with respect to $|\Psi_j(\phi)\rangle$. The bound is reached when the spaces spanned by $\left\{|\Psi_j(\phi)\rangle, |\dot{\Psi}_j(\phi)\rangle\right\}$ and $\left\{|\Psi_i(\phi)\rangle, |\dot{\Psi}_i(\phi)\rangle\right\}$ are orthogonal for all $i \neq j$. In particular, $Q = \tilde{Q}$ for the N00N state and if losses are present in only one channel, that is when $\eta_b = 1$. From now onwards, however, we will look at the case when losses in both arms are equal, i.e. $\eta_a = \eta_b$. In this case the bound is not always tight, since the states $|\Psi_j(\phi)\rangle$ may not always be orthogonal. Physically, this can be interpreted as the lack of knowledge of how many photons were lost in a particular mode.

Letting $\eta_a = \eta_b = \eta$, the upper bound for the QFI of the optimal states has been found in Ref. [159] and is given by

$$\tilde{Q} = 4\left(\sum_{n=0}^{N} n^2 x_n - \sum_{p=0}^{N}\sum_{q=0}^{N-p} \frac{\left(\sum_{n=p}^{N-q} x_n n \mathcal{L}_{pq}^n\right)^2}{\sum_{n=p}^{N-q} x_n \mathcal{L}_{pq}^n}\right), \tag{5.26}$$

where $x_n = |\alpha_n|^2$ and $\mathcal{L}_{pq}^n$ simplifies to $\mathcal{L}_{pq}^n = \binom{n}{p}\binom{N-n}{q}\eta^{N-p-q}(1-\eta)^{p+q}$. The corresponding input state $\tilde{\rho}(\phi)$ is in fact not the optimal state, as the optimal state would

be given by the true QFI, Q. In other words, $Q(\tilde{\rho}(\phi)) \leq Q(\rho(\phi))$ holds true. However, from convexity we also have $Q(\rho(\phi)) \leq \tilde{Q}(\rho(\phi))$, but $\tilde{Q}(\tilde{\rho}(\phi))$ is the global maximum, so in fact $Q(\rho(\phi)) \leq \tilde{Q}(\tilde{\rho}(\phi))$. Therefore, the QFI of the true optimal state must lie in between $Q(\tilde{\rho}(\phi))$ and $\tilde{Q}(\tilde{\rho}(\phi))$, where the difference between the two is small compared to the difference between the shot noise limit and the Heisenberg limit [159].

We will mention here two more reference states which we will find useful to comparing our novel probes to. These are the the N00N state and the coherent state, which reproduces the shot noise limit when the interferometer is fed with a coherent state $|\alpha\rangle$ in one arm, where $|\alpha|^2 = N$, and vacuum in the other. The resulting QFI of such a state is then

$$Q_{\mathrm{SNL}} = \frac{4N\eta_a\eta_b}{\left(\sqrt{\eta_a} + \sqrt{\eta_b}\right)^2} = N\eta, \tag{5.27}$$

assuming $\eta_a = \eta_b = \eta$. In addition, the QFI of the N00N state, $\frac{1}{\sqrt{2}}\left(|N0\rangle + |0N\rangle\right)$, is given by

$$Q_{\mathrm{N00N}} = \frac{4N^2\eta_a^N\eta_b^N}{\left(\eta_a^{N/2} + \eta_b^{N/2}\right)^2} = N^2\eta^N, \tag{5.28}$$

once again assuming $\eta_a = \eta_b = \eta$. We acknowledge that Q_{N00N} leads to the Heisenberg scaling $\frac{1}{N}$, as was expected.

5.4 Generalised Holland-Burnett states

Our novel probes are a generalization of the typical Holland-Burnett (HB) state [73]. The typical HB state is created by inputting equally photon-numbered Fock (also known as twin-Fock) states onto a 50:50 beam splitter, while the generalized Holland-Burnett (gHB) state is created by allowing the initial Fock states to be unequal, see Fig. 5.2. Following Eq. (3.44), the gHB state which is created from $|h_1\rangle_a|h_2\rangle_b$, where $h_1 + h_2 = N$, can be written in the following form

$$|\Psi^{(\mathrm{gHB})}\rangle = \mathcal{U}_{\mathrm{BS}}|h_1\rangle_a|h_2\rangle_b = \sum_{n=0}^{N} \mathcal{A}_N^{(1/2)}(n, h_1)|n\rangle_c|N-n\rangle_d. \tag{5.29}$$

We recognize these states as the same states used in the previous chapter but this time the delayed choice scheme is applied.

The QFI of this pure state can be calculated using Eq. (5.20), where the Hamilonian is $\mathcal{H} = c^\dagger c$. The second term in Eq. (5.20) is given by:

$$\begin{aligned}
\langle\Psi|c^\dagger c|\Psi\rangle &= \langle h_1, h_2|\mathcal{U}_{\mathrm{BS}}^\dagger c^\dagger c\,\mathcal{U}_{\mathrm{BS}}|h_1, h_2\rangle \\
&= \langle h_1, h_2|\mathcal{U}_{\mathrm{BS}}^\dagger c^\dagger \mathcal{U}_{\mathrm{BS}}\,\mathcal{U}_{\mathrm{BS}}^\dagger c\,\mathcal{U}_{\mathrm{BS}}|h_1, h_2\rangle \\
&= \langle h_1, h_2|\left(\frac{a^\dagger + b^\dagger}{\sqrt{2}}\right)\left(\frac{a+b}{\sqrt{2}}\right)|h_1, h_2\rangle \\
&= \frac{1}{2}\langle h_1, h_2|a^\dagger a + b^\dagger b|h_1, h_2\rangle \\
&= \tfrac{1}{2}(h_1 + h_2),
\end{aligned} \tag{5.30}$$

where in the second line we used the fact that $\mathcal{U}_{\mathrm{BS}}$ is unitary and in the third line we transformed mode c to the input modes a and b. The first term in equation (5.20) is

a Creation of Holland-Burnett states.

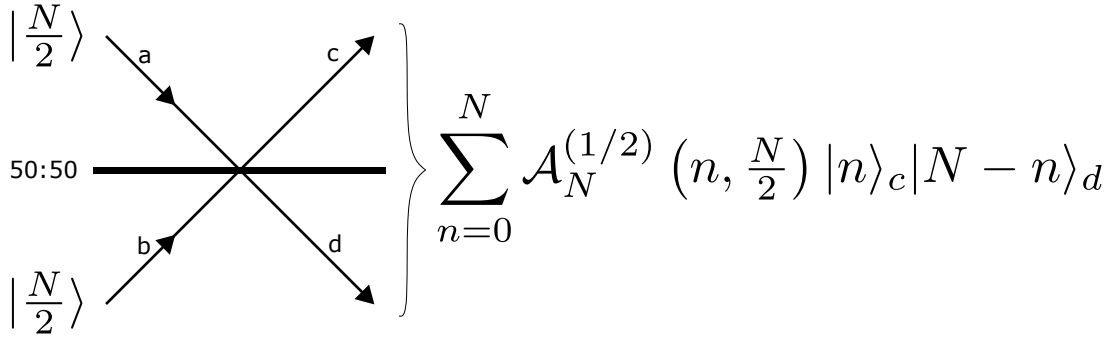

b Creation of generalised Holland-Burnett states.

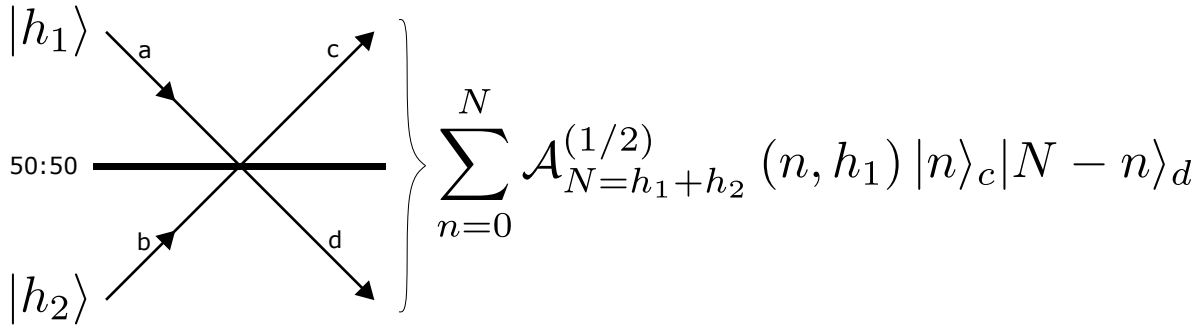

Figure 5.2: **a)** Holland-Burnett states are created by inputting equally photon-numbered Fock states onto a balanced beam splitter. **b)** for a generalised Holland-Burnett state we allow the initial Fock states to be unequal.

calculated in a similar manner:

$$\begin{aligned}
\langle\Psi|(c^\dagger c)^2|\Psi\rangle &= \langle h_1, h_2|\mathcal{U}_{\rm BS}^\dagger c^\dagger c c^\dagger c \mathcal{U}_{\rm BS}|h_1, h_2\rangle \\
&= \langle h_1, h_2|\left(\mathcal{U}_{\rm BS}^\dagger c^\dagger \mathcal{U}_{\rm BS}\mathcal{U}_{\rm BS}^\dagger c \mathcal{U}_{\rm BS}\right)^2|h_1, h_2\rangle \\
&= \langle h_1, h_2|\left[\left(\frac{a^\dagger + b^\dagger}{\sqrt{2}}\right)\left(\frac{a+b}{\sqrt{2}}\right)\right]^2|h_1, h_2\rangle \\
&= \frac{1}{4}\langle h_1, h_2|(a^\dagger + b^\dagger)(a+b)(a^\dagger + b^\dagger)(a+b)|h_1, h_2\rangle \\
&= \frac{1}{4}\langle h_1, h_2|a^\dagger a a^\dagger a + b^\dagger b b^\dagger b + 4a^\dagger a b^\dagger b + a^\dagger a + b^\dagger b|h_1, h_2\rangle \\
&= \tfrac{1}{4}(h_1^2 + h_2^2 + 4h_1h_2 + h_1 + h_2).
\end{aligned} \tag{5.31}$$

Therefore Q is given by

$$Q = \tfrac{1}{4}(h_1^2 + h_2^2 + 4h_1h_2 + h_1 + h_2) - \tfrac{1}{4}(h_1 + h_2)^2 = 2h_1h_2 + h_1 + h_2. \tag{5.32}$$

For a typical HB state, $h_1 = h_2 = \frac{N}{2}$, and Eq (5.32) simplifies to

$$Q = 2\frac{N}{2}\left(\frac{N}{2} + 1\right). \tag{5.33}$$

The gHB state can be created with the same kind of setup used in the entanglement distribution protocol in Chapter 4. The only difference is that heralding is used so that states of known photon number enter the beam splitter which is part of the Mach-Zehnder interferometer. The setup is shown in Fig. 5.3 with losses in all modes that leave the sources and in the modes just before the final detectors.

In the presence of losses, the gHB state in Eq. (5.29) becomes a mixed state $\rho_{\rm gHB}$. For the purpose of this study, we assume lossless heralded modes and equal transmissivity in the arms which go into the interferometer, $\eta_{s_1} = \eta_{s_2} = \eta_s$ in order to fairly compare with the optimal states.

Let us find the formula for the density operator representing the gHB state by following similar steps as in Subsection 4.3.1. We consider two copies of a TMSV and apply losses to the modes s_1 and s_2

$$\begin{aligned}
\rho = &\sum_{n,n',m,m'=0}^{\infty} \sqrt{\lambda_n\lambda_{n'}\lambda_m\lambda_{m'}}|n\rangle\langle n'|_{h_1}|m\rangle\langle m'|_{h_2} \\
&\times \sum_{p=0}^{\min(n,n')} \sqrt{\binom{n}{p}\binom{n'}{p}\eta_s^{n+n'-2p}\left(1-\eta_s\right)^{2p}}|n-p\rangle\langle n'-p|_{s_1} \\
&\times \sum_{q=0}^{\min(m,m')} \sqrt{\binom{m}{q}\binom{m'}{q}\eta_s^{m+m'-2q}\left(1-\eta_s\right)^{2q}}|m-q\rangle\langle m'-q|_{s_2},
\end{aligned} \tag{5.34}$$

which upon heralding of modes h_1 and h_2 reduce to

$$\begin{aligned}
\rho = &\lambda_{h_1}\lambda_{h_2}\sum_{p=0}^{h_1}\binom{h_1}{p}\eta_s^{h_1-p}\left(1-\eta_s\right)^p|h_1-p\rangle\langle h_1-p|_{s_1} \\
&\times \sum_{q=0}^{h_2}\binom{h_2}{q}\eta_s^{h_2-q}\left(1-\eta_s\right)^q|h_2-q\rangle\langle h_2-q|_{s_2}.
\end{aligned} \tag{5.35}$$

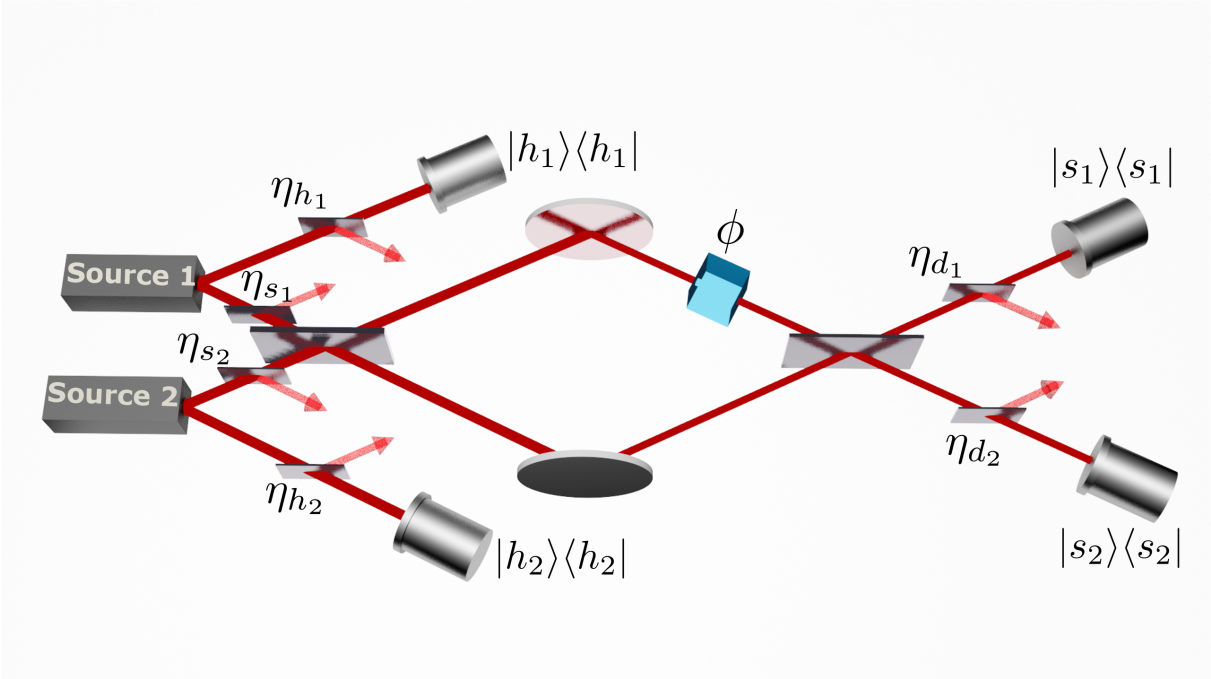

Figure 5.3: Setup for interferometry with generalised Holland-Burnett states. Two type-II parametric down-conversion sources each produce orthogonally-polarized pairs of beams that are separated using polarizing beam splitters. By measuring one of the beams from each source with a photon-number-resolving detector, we herald a pair of photon-number states $|h_1, h_2\rangle$. We inject this probe into an interferometer and perform photon counting at the output to estimate the unknown phase difference ϕ. Losses are modelled by placing fictitious beam splitters in all four modes before the interferometer and just before the signal detectors. Coefficients show the transmissivity of the beam splitters.

Putting the above state through a beam splitter and re-ordering the sums we arrive at

$$\rho_{\mathrm{gHB}}^{h_1+h_2=N} = \lambda_{h_1}\lambda_{h_2}\eta_s^N \sum_{p=0}^{h_1}\binom{h_1}{p}\left(\frac{1-\eta_s}{\eta_s}\right)^p \sum_{q=0}^{h_2}\binom{h_2}{q}\left(\frac{1-\eta_s}{\eta_s}\right)^q \times \sum_{k,k'=0}^{S(p,q)} \mathcal{A}_{S(p,q)}(k, h_1-p)\mathcal{A}^*_{S(p,q)}(k', h_1-p)|k, S(p,q)-k\rangle\langle k', S(p,q)-k'|, \tag{5.36}$$

where $S = N-p-q$ is the total number of photons found at the end of the interferometer.

5.5 Numerical results

Calculating the QFI of the state in Eq. (5.36) analytically is an intricate task, therefore we will resort to a numerical calculation using Eq. (5.9). We used the following method in Python 3 using the NumPy package

1. for both SPDC sources compute $\rho = |\Psi\rangle\langle\Psi|$ where, $|\Psi\rangle = \sum_{n=0}^{n_{\max}} \sqrt{\lambda_n}\,|n,n\rangle$, and $n_{\max}$ is a sum cutoff found by solving $\lambda_{n_{\max}}/\lambda_0 < 10^{-15}$ for a given g and 10^{-15} results from the precision of the numeric data type; usually $n_{\max} \geq 6$.

2. for all modes leaving the sources, add losses and then trace out unwanted reflected modes, i.e. perform the following operation

$$\rho' = \mathrm{Tr}_{r_h,r_s}\left\{\mathcal{U}_{\mathrm{BS}}^{(\eta_s)}\mathcal{U}_{\mathrm{BS}}^{(\eta_h)}|\Psi\rangle\langle\Psi|\left(\mathcal{U}_{\mathrm{BS}}^{(\eta_h)}\right)^\dagger\left(\mathcal{U}_{\mathrm{BS}}^{(\eta_s)}\right)^\dagger\right\},$$

   where r_s and r_h denote the reflected modes from the signal and herald, respectively, and η_s and η_h are the transmissivities of the signal and herald modes, respectively,

3. construct the density operator matrix for $\rho_{\mathrm{in}} = \rho' \otimes \rho'$,

4. apply the $50:50$ BS operation, $\rho_{\mathrm{BS}} = \mathcal{U}_{\mathrm{BS}}\,\rho_{\mathrm{in}}\,(\mathcal{U}_{\mathrm{BS}})^\dagger$,

5. for all $h_1, h_2 = 0, \ldots, N$ project ρ_{BS} onto $|h_1,h_2\rangle : \rho_{\mathrm{BS}}^{(h_1,h_2)} = \langle h_1,h_2|\rho_{\mathrm{BS}}|h_1,h_2\rangle$ such that $h_1+h_2 = N$ and renormalize the result,

6. apply a relative phase difference of $\phi = \frac{\pi}{4}$ between the interferometer arms, $\rho_\phi = e^{ic^\dagger c\phi}\rho_{\mathrm{BS}}^{(h_1,h_2)}e^{-ic^\dagger c\phi}$,

7. find eigenvalues and eigenvectors of ρ_ϕ

8. find the derivative of ρ_ϕ with respect to ϕ

9. compute the SLD matrix from

$$\Lambda(\rho_\phi) = \sum_{i,j}\frac{2\langle e_i(\phi)|\dot{\rho}_\phi|e_j(\phi)\rangle}{\lambda_i(\phi)+\lambda_j(\phi)}|e_i(\phi)\rangle\langle e_j(\phi)|,$$

10. compute the QFI according to the definition

$$Q(\rho_\phi) = \mathrm{Tr}\left\{\rho_\phi\Lambda(\rho_\phi)^2\right\}.$$

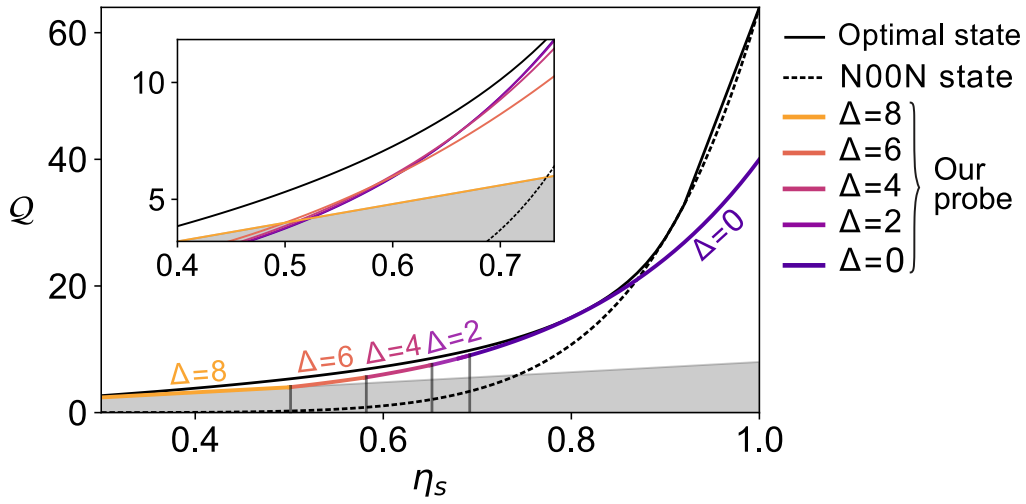

Figure 5.4: Quantum Fisher information $\mathcal{Q}$ calculated for 8-photon ($N = h_1 + h_2 = 8$) probes inside the interferometer as a function of the signal transmissivity η_s which is assumed to be equal in both interferometer modes. Coloured curve in the main figure plots $\mathcal{Q}$ of the probe with the optimal $\Delta = |h_1 - h_2|$ for a given η_s, while the inset shows the full curves of each probe for $\eta_s \in [0.4, 0.75]$. Our probe approximates the performance of the optimal state [black line] and surpasses that of the N00N state [dashed line] for efficiencies below 90%. The grey filled region indicates performance below the shot noise limit.

The above procedure was executed for $N = 8$ and $\eta_h = 1$ (no losses in the heralds) and $\eta_s \in (0, 1)$ in steps of 0.01 (assuming equal transmissivity in both interferometer arms).

The QFI of the optimal state on the other hand, was calculated in MATHEMATICA 12.2 by maximizing over coefficients $\{x_n\}$ in Eq. (5.26), using the function **FindMaxValue** and assuming the coefficients sum up to 1 and are real and positive. As mentioned earlier, the optimized QFI, $\tilde{Q}$, is the upper bound to the real QFI of the optimal states, Q, in the presence of losses but it is known to be a good approximation of the true maximal value of the QFI [159].

The results of these calculations are shown in Fig. 5.4. For $\eta_s \in (0, 0.5\rangle$ the best approximation to the optimal state is given by the probe with $\Delta = 8$; for $\eta_s \in (0.5, 0.58\rangle$ by the probe with $\Delta = 6$; for $\eta_s \in (0.58, 0.66\rangle$ by the probe with $\Delta = 4$; for $\eta_s \in (0.66, 0.69\rangle$ by the probe with $\Delta = 2$; and for $\eta_s > 0.69$ by the probe with $\Delta = 0$, as shown by the coloured line. Here, only fragments of the probe which performed best in the given region of transmissivity are shown but the inset shows the full curves and how they cross each other for a small region between 0.4 and 0.75. The shaded area is the shot noise limit which is a reference point of how much quantum advantage our probes provide. We observe that probes with a small Δ provide a greater advantage over the classical shot noise limit but are more sensitive to losses, while probes with Δ equal to N perform at least as well as the shot noise limit regardless of the amount of losses present. We infer that this allows us to choose the most optimal Δ for a given η_s in our system. This is possible because the probe is heralded. Fig. 5.4 also compares our results with the N00N state. As can be seen, the dashed (representing the N00N state) and black solid (representing the optimal state) lines almost coincide for efficiencies above $\sim 90\%$ (up to a numerical accuracy). This threshold can also be found numerically and for the case $N = 8$, following Ref. [159], we obtain $2.24^{-1/8} \approx 90\%$. Below 90% our probes significantly surpass the N00N state in

terms of the QFI, exhibiting performance close to the optimal. Moreover, in contrast to the N00N and HB states ($\Delta = 0$), our probes perform at least as well as the shot noise limit for any amount of loss.

5.6 Relation between entanglement and quantum Fisher information

In light of the results of Chapter 4 we deduce that states with the highest Fisher information are the states which are closest to the maximal entanglement for the Hilbert space they live in. This is illustrated in Fig. 5.5a where both the logarithmic negativity and QFI are shown for the pure $N = 8$ photon probe. For $h_1, h_2 = 4$ (equal inputs to the beam splitter) the dimension of the Hilbert space reduces as if $N = 4$, which can be understood by looking at the probability distribution for the outputs to the beam splitter in Fig. 5.5b. There, all odd photon-numbered components disappear reducing the dimension of the space by half. The maximal entanglement available in that space is then $E_{\mathcal{N}} = \log_2(4+1) \approx 2.32$ which is shown by the lower dashed line in Fig. 5.5a. We observe the triangle showing the logarithmic negativity for the state $|4, 4\rangle$ almost touches that line, while the other states which live in higher-dimensional spaces are noticeably further away from the maximal entanglement available in their Hilbert space.

The relation between entanglement and the QFI has been studied in, e.g. Ref. [160], where it has been shown that the QFI gives a sufficient condition to recognize multiparticle entanglement and a quantum state must necessarily be entangled to be useful in overcoming the shot noise sensitivity. These states can be recognised if they satisfy $\chi < 1$ where $\chi^2 = N/Q$. As an example, this parameter would take $\chi = \sqrt{8/40}$ for the probes $|4, 4\rangle$ which clearly satisfies the condition.

Interestingly, a quantitative relation between the amount of entanglement and the QFI cannot be drawn for our gHB states. We observe some states have the same amount of entanglement in terms of the logarithmic negativity but very different QFI. This is because, as discussed in Subsection 5.1.2, the evolution of the state under the unitary applying the parameter ϕ, has to happen in the direction perpendicular to the state and different states may change differently in the subspace of quantum states of the same entanglement.

Some further insights into why the probe $|4, 4\rangle$ provides the best QFI can be gained by looking at the probability distributions in Fig. 5.5b and c. These distributions are probability distributions of obtaining outcome $|m, N - m\rangle$ at the output of the beam splitter when probe $|4, 4\rangle$ (b) or $|0, 8\rangle$ (c) enters at the input. From Ref. [161] we know that the most optimal pure state is the coherent superposition of eigenstates corresponding to the minimal and maximal eigenvalues of the generator of the phase dynamics. In our case, the generator is $c^\dagger c$ and the extremal eigenvalues are 0 and 8 with $|0, 8\rangle$ and $|8, 0\rangle$ as the corresponding eigenstates. The most optimal state is thus $\frac{|0,8\rangle+|8,0\rangle}{\sqrt{2}}$. We note that the state in Fig. 5.5b carries the $|0, 8\rangle, |8, 0\rangle$ components with high probability, while for the state in Fig. 5.5c these components have very low probability of exiting the output to the beam splitter. We thus expect that the state in Fig. 5.5b has higher quantum Fisher information which is indeed what we observe in Fig. 5.5a. On the other hand, the state with $|0, 8\rangle$ or $|8, 0\rangle$ at the input, which corresponds to $\Delta = 8$, has the highest probability of generating the balanced $|4, 4\rangle$ state at the output which makes it most robust to losses, as we observed in the previous section.

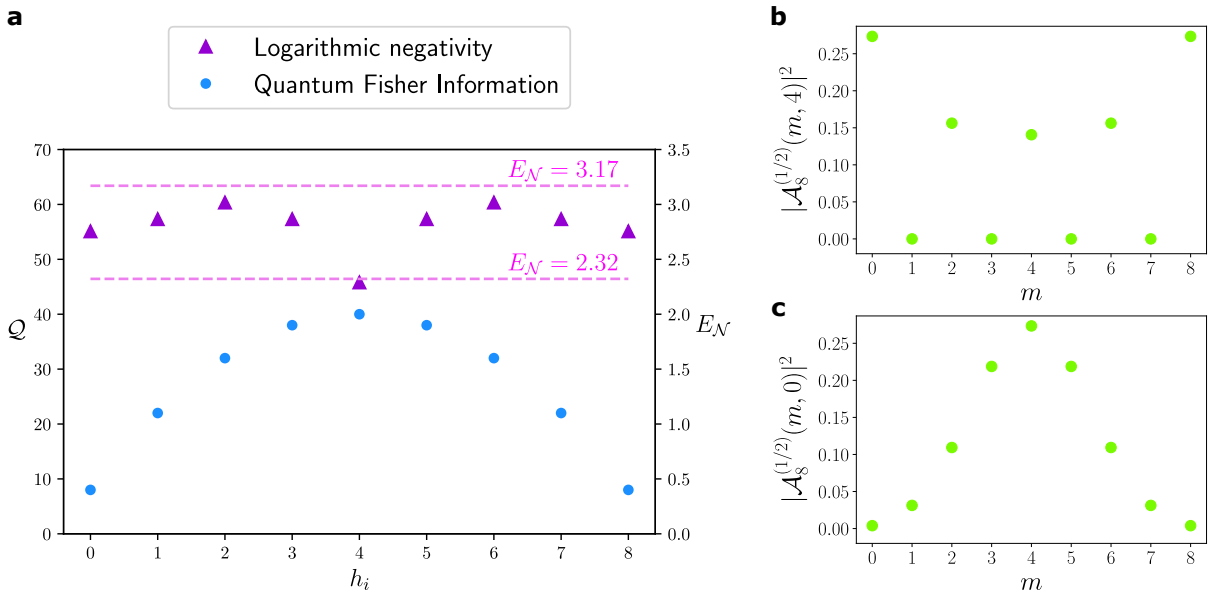

Figure 5.5: **a)** Quantum Fisher information, $\mathcal{Q}$ (blue dots) and logarithmic negativity, $E_\mathcal{N}$ (violet triangles) as a function of the photon number in the heralded input to the beam splitter, h_i where $i = 1, 2$. The light violet dashed lines mark the maximal entanglement available in a Hilbert space of dimension 8 (upper line) and 4 (lower line). The state with the highest relative entanglement ($h_1, h_2 = 4$) also carries the highest quantum Fisher information. Losses are not considered in these results. **b)** Probability amplitudes at the output of the beam splitter when the probe $|4, 4\rangle$ was input. All odd photon number components are zero and the most likely outcomes are states $|0, 8\rangle$ and $|8, 0\rangle$. **c)** Probability amplitudes at the output of the beam splitter when the probe $|0, 8\rangle$ was input. The states $|0, 8\rangle$ and $|8, 0\rangle$ are least likely to occur.

5.7 Experimental setup and results

These theoretical findings have been applied in an experiment done by my collaborators at the group of Professor Ian Walmsley at the University of Oxford [119]. Their findings are summarised briefly below.

In the experiment, periodically poled potassium titanyl phosphate (PPKTP) waveguides pumped with ~ 0.5 ps long pulses from a mode-locked laser at a repetition rate of 100 kHz are used as the SPDC source. The four detectors are superconducting TES which can count up to 10 photons with a detection efficiency exceeding 95% and the interferometer is a fiber-based device in which the distance between two evanescently coupled fibers can be controlled with a micrometer to vary ϕ.

The procedure is to measure interference fringes given by the joint photon-number probability per pump pulse to obtain the herald outcome (h_1, h_2) and measure (s_1, s_2) at the output of the interferometer when the phase difference is ϕ. This will be referred to as the (s_1, s_2, h_1, h_2) rate. To quantify the phase sensitivity for a particular herald outcome (h_1, h_2) the classical Fisher information is calculated using the formula

$$\mathcal{F}_{h_1,h_2}(\phi) = \sum_{s_1,s_2} \frac{\left[\partial_\phi \tilde{\mathrm{pr}}_{s_1,s_2,h_1,h_2}(\phi)\right]^2}{\tilde{\mathrm{pr}}_{s_1,s_2,h_1,h_2}(\phi)}, \tag{5.37}$$

where ∂_ϕ denotes the partial derivative with respect to ϕ, and $\tilde{\mathrm{pr}}_{s_1,s_2,h_1,h_2}(\phi)$ is a model fitted to the measured rates.

The performance of the different probes used in the experiment will be evaluated using the classical Fisher information per detected signal photon conditioned on measuring (h_1, h_2) at the heralding detectors

$$\tilde{\mathcal{F}}_{h_1,h_2}(\phi) = \mathcal{F}_{h_1,h_2}(\phi) / \langle \tilde{n} \rangle , \tag{5.38}$$

where

$$\langle \tilde{n} \rangle = \sum_{s_1,s_2} (s_1 + s_2) \tilde{\mathrm{pr}}_{s_1,s_2,h_1,h_2}(\phi), \tag{5.39}$$

is the total number of detected signal photons. Injecting a coherent state into our interferometer would in principle yield the Fisher information $\mathcal{F} = \langle \tilde{n} \rangle$ when the detected mean photon number is $\langle \tilde{n} \rangle$ [149]. Thus, our figure of merit can be easily compared to the shot noise limit which corresponds to $\tilde{\mathcal{F}}_{h_1,h_2}(\phi) = 1$.

The total efficiency of the heralding and signal modes in the experiment was estimated to be between 47-55%. This includes 90% waveguide transmission, 70% mode coupling efficiency into fibres, 90% interferometer transmission, and $\geq$95% detector efficiency. Due to the latter two losses, the detected $\langle \tilde{n} \rangle$ is 10-15% smaller than the mean photon number inside the interferometer. As such, the Fisher information per photon inside the interferometer is about 10-15% smaller than $\tilde{\mathcal{F}}_{h_1,h_2}(\phi)$. Considering these numbers, we are in the regime of highest losses as shown in Fig. 5.4 and thus probe with $\Delta = N$ should provide the highest sensitivity.

Fig. 5.6a shows $\tilde{\mathcal{F}}_{h_1,h_2}(\phi)$ calculated without post-selection for all probes with $N = 8$. Such large probes are achieved by increasing the pump power to 135 μW per source whereby 16-photon events are detected roughly 7 times per second. As predicted, the best sensitivity is achieved by the probe with the largest Δ due to its increased robustness to loss. The reason for the inability of this probe to surpass the shot noise limit is the contamination of the signal with states for which $\Delta \neq N$. In other words, the detection

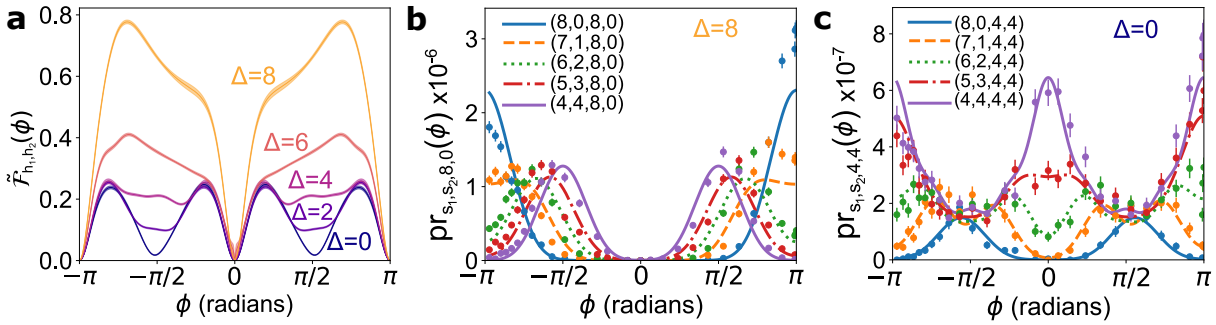

Figure 5.6: **a)** $\tilde{\mathcal{F}}_{h_1,h_2}(\phi)$ of 8-photon probes ($N = 8$) parameterized by $\Delta = |h_1 - h_2|$. Curves are calculated using the data and Eqs. (5.37) and (5.39) without post-selection. Probes with a larger Δ have a larger $\tilde{\mathcal{F}}_{h_1,h_2}(\phi)$ and hence greater phase sensitivity due to their increased robustness to loss. Line thicknesses show 1σ confidence intervals obtained by fitting 50 simulated data sets that are calculated with a Monte Carlo method. **b)** and **c)** show a subset of rates for the probe with $\Delta = 8$ and $\Delta = 0$, respectively. Error bars are one standard deviation assuming Poissonian counting statistics. The lines are a model fitted to $\mathrm{pr}_{s_1,s_2,h_1,h_2}(\phi)$.

of 0 photons in one of the detectors could occur due to photon loss in the mode entering that detector. In principle, the $\Delta = N$ probe is created from all photons originating from a single source while the other produces a vacuum. Therefore, it should be possible to recover shot noise limited performance by blocking one of the sources. That this is indeed the case is shown in Fig. 5.7, where the bold line shows the classical Fisher information for both sources unblocked and the dashed yellow line is the result of one source blocked. The dashed line reaches the shot noise limit at the most optimal phase which is around $\phi = \pm\frac{\pi}{2}$.

Interestingly, our probes do not show oscillations which are typical for HB or N00N states. For example, the probes with $\Delta = 4, 6, 8$ shown in Fig. 5.6a do not have a dip in $\tilde{\mathcal{F}}_{h_1,h_2}(\pm\pi/2)$. The origin of this effect for $\Delta = 8$, which we will take as an example, can be seen directly in the rates shown in Fig. 5.6b. Non-zero gradients in the fringes in the range between 0 and $\pm\pi$ result in high sensitivity of measuring ϕ in this range. This can be contrasted with the fringes of the HB state shown in Fig. 5.6c, where all gradients are zero at $\phi = \pm\frac{\pi}{2}$ leading to a drop in sensitivity at this point. The lack of simple periodicity of $\tilde{\mathcal{F}}_{h_1,h_2}(\phi)$ for gHB states allows estimating ϕ without prior knowledge of the range in which it lies, as is required for N00N or HB states, and thus provides a means for global phase estimation without using an adaptive protocol [162, 163].

There is also a simple way of showing that the features of our probes result from nonclassical behaviour. This is achieved by temporarily delaying photons coming from one source with respect to the other by more than the coherence time. The comparison between the resulting classical Fisher information and the one when photons are injected into the interferometer at the same time is shown in Fig. 5.8 for a probe $|3, 2\rangle$. Indeed, the improvement in favour of the probes where photons interfere is significant. This demonstrates that the probe sensitivity derives from multiphoton interference even at high photon numbers.

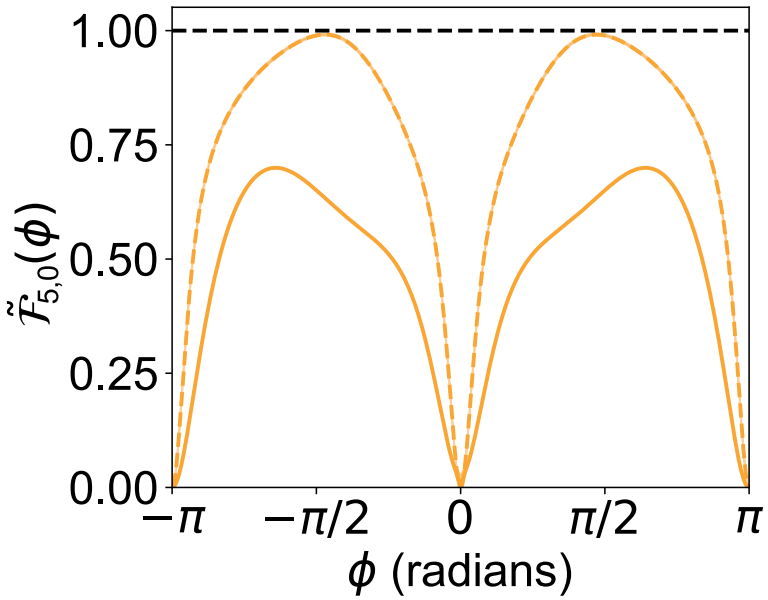

Figure 5.7: $\tilde{\mathcal{F}}_{5,0}(\phi)$ calculated without post-selection. Bold yellow line shows result with both sources unblocked, whereas dashed yellow line is result with one of the sources blocked. The thicknesses of the yellow lines show 1σ confidence intervals obtained by fitting 50 simulated experiments. Dashed black line is the shot noise limit.

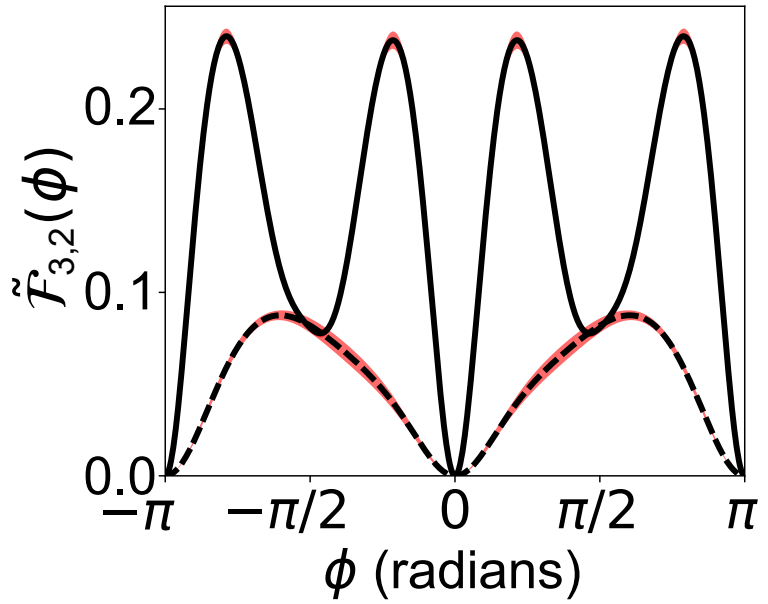

Figure 5.8: $\tilde{\mathcal{F}}_{3,2}(\phi)$ shows a significant improvement in sensitivity in the former case (bold line) compared to the latter case (dashed line), demonstrating that multiphoton interference improved the sensitivity of our probe. Red shaded regions shows 1σ confidence intervals obtained by fitting 50 simulated data sets.

5.8 Conclusions

We proposed and experimentally demonstrated a scheme for quantum-enhanced interferometry that exploits bright two-mode squeezed vacuum sources and photon-number-resolving detectors. This scheme prepares probes which are near-optimal in the presence of arbitrary losses and perform at least as well as the shot noise limit. Thanks to the heralding scheme of our proposal, one has the possibility of choosing the probe with the most optimal Δ in a given experimental scenario. With improvements in the quality of the experimental realisation, in particular increasing coupling efficiency and compatibility with transition-edge sensors, our loss-tolerant scheme paves the way towards scaling up quantum-enhanced interferometry and implementing multi-photon quantum technologies in real-life applications.

Chapter 6

Summary and outlook

In this thesis we demonstrated the applicability of protocols based on multi-photon bipartite entanglement to two selected quantum technologies. The protocols were designed based on the current performance of photonic hardware making them directly implementable in the laboratory. In addition, they were shown to exhibit state-of-the-art features, as summarised below.

The first protocol was capable of performing entanglement distribution in the presence of very high losses in the transmitting channels. We thus foresee its usefulness in quantum communications where the transmission could occur between two parties located on the ground at a large distance and a broadcasting station was placed between them, either on a satellite in the case of free-space communication or on the ground if optical fibres were chosen. Regardless of the scenario, the entanglement distribution protocol achieves the state-of-the-art scaling $O(\sqrt{\eta})$ of efficiency with channel transmittance, which is a quadratic improvement compared to the polarization-entangled photon pairs. Therefore, there is a clear advantage in using multi-photon states over single photon pairs.

The second protocol was based on the same multi-photon states but this time applied for interferometry. In this context, the robustness to losses was reflected in the near-optimal performance of our multi-photon probes in the presence of arbitrary transmission in the interferometer. Moreover, the probes performed at least as well as the shot noise limit regardless of the amount of loss and they could be tuned via the heralding scheme to give the most optimal sensitivity if the amount of loss was known in the system. The possibility of using multi-photon states in quantum metrology is motivating because typically having more photons in a probe relates to higher quantum Fisher information and hence higher sensitivity.

With the above two examples, we hope to show that multi-photon bipartite entangled states have the potential to compete with single-photon pairs in creating quantum technologies. These examples, however, are by no means exhaustive. Further applications could include quantum imaging, quantum key distribution or quantum machine learning. The feature of our multi-photon states that makes them so versatile is the robustness of the state's properties to transmission losses, be it entanglement or quantum Fisher information. We expect that there exist other features of these states that could be the basis of other technologies not mentioned in this thesis.

An important point of this thesis was also the idea of establishing protocols which are feasible with the current experimental equipment. We have considered realistic parameters in all our numerical simulations of a true experiment, however, we have not taken into account the fact that the individual devices may not be exactly compatible with each

other. For example, spontaneous parametric down conversion sources which are compatible with the transition edge sensors that simultaneously achieve high modal purity, efficiency and squeezing are still to be developed. This would enable overcoming the shot noise limit in an actual experimental implementation of our quantum metrology protocol and demonstrate its performance for all generalised Holland-Burnett states discussed in Chapter 5.

Bibliography

[1] Dowling, J. P. and Milburn, G. J. Quantum technology: the second quantum revolution. *Phil. Trans. R. Soc. A.* **361,** 1655–1674 (2003).

[2] Pan, J.-P., Chen, Z.-B., Lu, C.-Y., Weinfurter, H., Zeilinger, A. and Żukowski, M. Multiphoton entanglement and interferometry. *Rev. Mod. Phys.* **84**, 777 (2012).

[3] Horodecki, R., Horodecki, P., Horodecki, M. & Horodecki, K. Quantum entanglement. *Rev. Mod. Phys.* **81,** 865-942 (2009).

[4] Huang, H.-Y., Broughton, M., Cotler, J., Chen, S., Li, J., Mohseni, M., Neven, H., Babbush, B., Kueng, R., Preskill, J., and McClean, J. R. Quantum advantage in learning from experiments. *Science* **376,** 1182-1186 (2022).

[5] Gisin, N. and Thew, R. Quantum communication. *Nat. Photonics* **1,** 165-171 (2007).

[6] Dowling, J. P. Correlated input-port, matter-wave interferometer: Quantum-noise limits to the atom-laser gyroscope. *Phys. Rev. A* **57,** 4736 (1998).

[7] Eldredge, Z., Foss-Feig, M., Gross, J. A., Rolston, S. and Gorshkov, A. V. Optimal and secure measurement protocols for quantum sensor networks. *Phys. Rev. A* **97,** 042337 (2018).

[8] Zhao, S.-R. et al. Field demonstration of distributed quantum sensing without post-selection. *Phys. Rev. X* **11,** 031009 (2021).

[9] Valiev, K. A. Quantum computers and quantum computations. *Phys.-Usp.* **48,** 1 (2005).

[10] Slussarenko, S. and Pryde, G. J., Photonic quantum information processing: a concise review. *Applied Physics Reviews* **6**, 041303 (2019).

[11] Eisaman, M. D., Fan, J., Migdall, A. and Polyakov, S. V. Invited Review Article: Single-photon sources and detectors. *Rev. Sci. Instrum.* **82**, 071101 (2011).

[12] Migdall, A., Polyakov, S. V., Fan, J. and Bienfang, J. C. *Single-photon generation and detection: physics and applications*, Academic Press (2013).

[13] Ghioni, M., Gulinatti, A., Rech, I., Zappa, F. and Cova, S. Progress in Silicon Single-Photon Avalanche Diodes, in *IEEE Journal of Selected Topics in Quantum Electronics* **13**, 852-862 (2007).

[14] Reddy, D. V., Lita, A. E., Nam, S. W., Mirin, R. P. and Verma, V. B. Achieving 98% system efficiency at 1550 nm in superconducting nanowire single photon detectors. In: *Rochester Conference on Coherence and Quantum Optics (CQO-11)*, OSA Technical Digest, Optical Society of America, paper W2B.2 (2019).

[15] Cahall, C., Nicolich, K. L., Islam, N. T., Lafyatis, G. P., Miller, A. J., Gauthier, D. J. and Kim, J. Multi-photon detection using a conventional superconducting nanowire single-photon detector. *Optica* **4,** 1534-1535 (2017).

[16] https://www.nist.gov/news-events/news/2016/01/less-jitter-more-bits-new-material-detecting-photons-captures-more-quantum

[17] Turin, G. An introduction to matched filters. In: *IRE Transactions on Information Theory* **6**, 311-329 (1960).

[18] Lita, A. E., Miller, A. J. and Nam, S. W. Counting near-infrared single-photons with 95% efficiency. *Opt. Express* **16**, 3032–3040 (2008).

[19] Lita, A. E., Calkins, B., Pellouchoud, L. A., Miller, A. J., and Nam, S. W. Superconducting transition-edge sensors optimized for high-efficiency photon-number resolving detectors. *Proc. SPIE* **7681**, 76810D (2010).

[20] Fukuda, D. et al. Titanium-based transition-edge photon number resolving detector with 98% detection efficiency with index-matched small-gap fiber coupling. *Opt. Express* **19**, 870–875 (2011).

[21] Humphreys, P. C., Metcalf, B. J., Gerrits, T., Hiemstra, T., Lita, A. E., Nunn, J., Nam, S. W., Datta, A., Kolthammer, W. S. and Walmsley, I. A. Tomography of photon-number resolving continuous-output detectors. *New J. Phys.* **17,** 103044 (2015).

[22] Lolli, L., Taralli, E. and Rajteri, M. Ti/Au TES to Discriminate Single Photons. *J. Low. Temp. Phys.* **167**, 803–808 (2012).

[23] Sadleir, J. E. *(private communication).*

[24] https://www.nist.gov/news-events/news/2014/10/new-high-resolution-x-ray-spectrometer-beam-lines

[25] Kako, S., Santori, C., Hoshino, K., Gotzinger, S., Yamamato, Y. and Arakawa, Y. A gallium nitride single-photon source operating at 200K. *Nature Mater.* **5,** 887-892 (2006).

[26] Strauf, S., Stoltz, N. G., Rakher, M. T., Coldren, L. A., Petroff, P. M. and Bouwmeester, D. High-frequency single-photon source with polarization control. *Nature Photon.* **1**, 704-708 (2007).

[27] Maurer, C., Becher, C., Russo, C., Eschner, J. and Blatt, R. A single-photon source based on a single Ca^+ ion. *New J. Phys.* **6**, 94 (2004).

[28] Hennrich, M., Legero, T., Kuhn, A. and Rempe, G. Photon statistics of a non-stationary periodically driven single-photon source. *New J. Phys.* **6**, 86 (2004).

[29] Alleaume, R., Treussart, F., Messin, G., Dumeige, Y., Roch, J.-F., Beveratos, A., Brouri-Tualle, R., Poizat, J.-P. and Grangier, P. Experimental open-air quantum key distribution with a single-photon source. *New J. Phys.* **6**, 92 (2004).

[30] Gaebel, T., Popa, I., Gruber, A., Domhan, M., Jelezko, F. and Wrachtrup, J. Stable single-photon source in the near infrared. *New J. Phys.* **6,** 98 (2004).

[31] Högele, A., Galland, C., Winger, M. and Imamoğlu, A. Photon antibunching in the photoluminescence spectra of a single carbon nanotube. *Phys. Rev. Lett.* **100**, 217401 (2008).

[32] Senellart, P., Solomon, G., and White, A. High-performance semiconductor quantum-dot single-photon sources. *Nature Nanotech* **12,** 1026–1039 (2017).

[33] Loredo, J., Broome, M., Hilaire, P., Gazzano, O., Sagnes, I., Lemaitre, A., Almeida, M., Senellart, P. and White, A. Boson sampling with single-photon Fock states from a bright solid-state source. *Phys. Rev. Lett.* **118,** 130503 (2017).

[34] Wang, H. et al. High-efficiency multiphoton boson sampling. *Nat. Photonics* **11,** 361–365 (2017).

[35] Ellis, D. J. P., Bennett, A. J., Dangel, C., Lee, J. P., Griffiths, J. P., Mitchell, T. A., Paraiso, T.-K., Spencer, P., Ritchie, D. A. and A. J. Shields, A. J. Independent indistinguishable quantum light sources on a reconfigurable photonic integrated circuit. *Appl. Phys. Lett.* **112,** 211104 (2018).

[36] Antón, C. et al. Interfacing scalable photonic platforms: solid-state based multiphoton interference in a reconfigurable glass chip. *Optica* **6,** 1471-1477 (2019).

[37] Louisell, W. H., Yariv, A. and Siegman, A. E. Quantum fluctuations and noise in parametric processes. I. *Phys. Rev.* **124**, 1646–1654 (1961).

[38] Klyshko, D. N. Scattering of light in a medium with nonlinear polarizability. *Sov. Phys. JETP* **28**, 522 (1969).

[39] Burnham, D. C. and Weinberg, D. L. Observation of simultaneity in parametric production of optical photon pairs. *Phys. Rev. Lett.* **25**, 84 (1970).

[40] Ferguson, K. R., Beavan, S. E., Longdell, J. J. and Sellars, M. J. Generation of light with multimode time-delayed entanglement using storage in a solid-state spin-wave quantum memory. *Phys. Rev. Lett.* **117**, 020501 (2016).

[41] Mandel, L. and Wolf, E. *Optical Coherence and Quantum Optics*, Cambridge University Press, New York (1995).

[42] Chen, J., Pearlman, A. J., Ling, A., Fan, J. and Migdall, A. A versatile waveguide source of photon pairs for chip-scale quantum information processing. *Opt. Express* **17,** 6727 (2009).

[43] Zhang, C., Huang, Y., Liu, B., Li, C. and Guo, G. Spontaneous parametric down-conversion sources for multiphoton experiments. *Advanced Quantum Technologies* **4(5),** 2000132 (2021).

[44] Novikova, T. I., Kuznetsov, K. A., Leontyev, A. A. and Kitaeva, G. Kh. Study of SPDC spectra to reveal temperature dependences for optical-terahertz biphotons. *Appl. Phys. Lett.* **116,** 264003 (2020).

[45] Flórez, J., Lundeen, J. S., and Chekhova, M. V. Pump depletion in parametric down-conversion with low pump energies. *Opt. Lett.* **45,** 4264-4267 (2020).

[46] Grice, W. P., U'Ren, A. B. and Walmsley, I. A. Eliminating frequency and space-time correlations in multiphoton states. *Phys. Rev. A* **64,** 063815 (2001).

[47] Grice, W. P. and Walmsley, I. A., Spectral information and distinguishability in type-II down-conversion with a broadband pump. Phys. Rev. A **56,** 1627 (1997).

[48] Fiorentino, M., Spillane, S. M., Beausoleil, R. G., Roberts, T. D., Battle, P. and Munro, M. W. Spontaneous parametric down-conversion in periodically poled KTP waveguides and bulk crystals. *Opt. Express* **15,** 7479-7488 (2007).

[49] Gerry, C. and Knight, P. *Introductory Quantum Optics*, Cambridge University Press (2004).

[50] Lvovsky, A. I. Squeezed light. In: *Photonics Volume 1: Fundamentals of Photonics and Physics*, John Wiley & Sons, Ltd., (2015).

[51] Buzek, V. and Knight, P. L. Squeezed States: Basic Principles. In: *Quantum Squeezing*, Springer, Berlin Heidelberg (2004).

[52] Klimov, A. B. and Chumakov, S. M. *A Group-Theoretical Approach to Quantum Optics: Models of Atom-Field Interactions*, Wiley (2009).

[53] Tan, D., Sun, X. and Qiu, J. Femtosecond laser writing low-loss waveguides in silica glass: highly symmetrical mode field and mechanism of refractive index change. *Opt. Mater. Express* **11,** 848-857 (2021).

[54] Bonneau, D., Lobino, M., Jiang, P., Natarajan, C. M., Tanner, M. G., Hadfield, R. H., Dorenbos, S. N., Zwiller, V., Thompson, M. G. and O'Brien J. L. Fast path and polarization manipulation of telecom wavelength single photons in lithium niobate waveguide devices. *Phys. Rev. Lett.* **108,** 053601 (2012).

[55] Sun, J., Timurdogan, E., Yaacobi, A., Hosseini, E. S. and Watts, M. R. Large-scale nanophotonic phased array. *Nature* **493,** 195–199 (2013).

[56] Crespi, A., Osellame, R., Ramponi, R., Bentivegna, M., Flamini, F., Spagnolo, N., Viggianiello, N., Innocenti, L., Mataloni, P. and Sciarrino, F. Suppression law of quantum states in a 3d photonic fast Fourier transform chip. *Nat. Commun.* **7,** 10469 (2016).

[57] Rambu, A. P., Apetrei, A. M., Doutre, F., Tronche, H., Tiron, V., de Micheli, M. and Tascu, S. Lithium niobate waveguides with high-index contrast and preserved nonlinearity fabricated by a high vacuum vapor-phase proton exchange. *Photon. Res.* **8,** 8-16 (2020).

[58] Silverstone, J. W., Bonneau, D. O'Brien, J. L. and Thompson, M. G. Silicon quantum photonics. *IEEE J. Sel. Top. Quantum Electron.* **22,** 390–402 (2016).

[59] Guo, X., Zou, Cl., Schuck, C. et al. Parametric down-conversion photon-pair source on a nanophotonic chip. *Light Sci. Appl.* **6,** e16249 (2017).

[60] Meyer-Scott, E., Prasannan, N., Eigner, C., Quiring, V., Donohue, J. M., Barkhofen, S. and Silberhorn, C. High-performance source of spectrally pure, polarization entangled photon pairs based on hybrid integrated-bulk optics. *Opt. Express* **26,** 32475-32490 (2018).

[61] Bennink, R. S. Optimal collinear Gaussian beams for spontaneous parametric down-conversion. *Phys. Rev. A* **81,** 053805 (2010).

[62] Calkins, B. et al. High quantum-efficiency photon-number-resolving detector for photonic on-chip information processing. *Opt. Express* **21,** 22657–22670 (2013).

[63] Höpker, J. P., Gerrits, T., Lita, A., Krapick, S., Herrmann, H., Ricken, R., Quiring, V., Mirin, R., Nam, S. W., Silberhorn, C. and Bartley, T. J. Integrated transition edge sensors on titanium in-diffused lithium niobate waveguides *APL Photonics* **4,** 056103 (2019).

[64] Krawtchouk, M. Sur une generalisation des polynômes d'Hermite. *Comptes Rendus de l'Academie des sciences, Series I - Mathematique* **189,** 620–622 (1929).

[65] Atakishiyeva, M. K., Atakishiyev, N. M. and Wolf, K. B. Kravchuk oscillator revisited. *J. Phys.: Conf. Ser.* **512,** 012031 (2014).

[66] Olver, F. W. J., Olde Daalhuis, A. B., Lozier, D. W. Schneider, B. I., Boisvert, R. F. Clark, C. W., Miller, B. R., Saunders, B. V., Cohl, H. S. and McClain, M. A. (Eds.) NIST Digital Library of Mathematical Functions. http://dlmf.nist.gov/, Release 1.1.3 of 2021-09-15.

[67] Koekoek, R. and Swarttouw, R. F. Krawtchouk. In: *The Askey-Scheme of Hypergeometric Orthogonal Polynomials and its q-Analogue.* Technische Universiteit Delft, Faculty of Technical Mathematics and Informatics Report 98-17, Delft, Netherlands (1998).

[68] Zeilinger, A. General properties of lossless beam splitters in interferometry. *Am. J. Phys.* **49,** 882 (1981).

[69] Fearn, H. and Loudon, R. Quantum theory of the lossless beam splitter. *Opt. Commun.* **64,** 485 (1987).

[70] Koepf, W. Hypergeometric Database. In: *Hypergeometric Summation.* Universitext. Springer, London (2014).

[71] Hong, C. K., Ou, Z. Y. and Mandel, L. Measurement of subpicosecond time intervals between two photons by interference. *Phys. Rev. Lett.* **59,** 2044 (1987).

[72] Pittman, T, B, Strekalov, D. V., Migdall, A., Rubin, M. H., Sergienko, A. V. and Shih, Y. H. Can two-photon interference be considered the interference of two photons? *Phys. Rev. Lett.* **77,** 1917 (1996).

[73] Holland, M. J. and Burnett, K. Interferometric detection of optical phase shifts at the Heisenberg limit. *Phys. Rev. Lett.* **71,** 1355–1358 (1993).

[74] Boto, A. N., Kok, P., Abrams, D. S., Braunstein, S. L., Williams, C. P. and Dowling, J. P. Quantum interferometric optical lithography: exploiting entanglement to beat the diffraction limit. *Phys. Rev. Lett.* **85,** 2733 (2000).

[75] Lee, H., Kok. P. and Dowling, J. P. A quantum Rosetta stone for interferometry. *J. Mod. Opt.* **49,** 2325-2338 (2002).

[76] Lee, C. T. External photodetection of cavity radiation. *Phys. Rev. A* **48,** 2285 (1993).

[77] Kiss, T., Herzog, U. and Leonhardt, U. Compensation of losses in photodetection and in quantum-state measurements. *Phys. Rev. A* **52,** 2433 (1995).

[78] Wootters, W. K. and Zurek, W. H. A single quantum cannot be cloned. *Nature* **299,** 802-803 (1982).

[79] Briegel, H.-J., Dur, W., Cirac, J. I. and Zoller, P. Quantum repeaters: the role of imperfect local operations in quantum communication. *Phys. Rev. Lett.* **81,** 5932-5935 (1998).

[80] Munro, W. J., Stephens, A. M., Devitt, S. J., Harrison, K. A. and Nemoto, K. Quantum communication without the necessity of quantum memories. *Nat. Photonics* **6,** 777-781 (2012).

[81] Muralidharan, S., Kim, J., Lütkenhaus, N., Lukin, M. D. and Jiang, L. Ultrafast and fault-tolerant quantum communication across long distances. *Phys. Rev. Lett.* **112,** 250501 (2014).

[82] Azuma, K., Tamaki, K. and Lo, H.-K. All-photonic quantum repeaters. *Nat. Commun.* **6,** 6787 (2015).

[83] Humphreys, P. C., Kalb, N., Morits, J. P. J., Schouten, R. N., Vermeulen, R. F. L., Twitchen, D. J., Markham, M. and Hanson, R. Deterministic delivery of remote entanglement on a quantum network. *Nature* **558**, 268-273 (2018).

[84] Zwerger, M., Pirker, A., Dunjko, V., Briegel, H. J. and Dür, W. Long-range big quantum-data transmission. *Phys. Rev. Lett.* **120,** 030503 (2018).

[85] Hasegawa, Y., Ikuta, r., Matsuda. N., Tamaki. K., Lo, H.-K., Yamamoto, T. Azuma, K. and Imoto, N. Experimental time-reversed adaptive Bell measurement towards all-photonic quantum repeaters. *Nat. Commun.* **10,** 378 (2019).

[86] Li, Z.-D. et al. Experimental quantum repeater without quantum memory. *Nat. Photonics* **13,** 644-648 (2019).

[87] Yu, Y. et al. Entanglement of two quantum memories via fibres over dozens of kilometres. *Nature* **578,** 240-245 (2020).

[88] Pu, Y.-F., Zhang, S., Wu, Y.-K., Jiang, N., Chang, W. Li, C. and Duan, L.-M. Experimental demonstration of memory-enhanced scaling for entanglement connection of quantum repeater segments. *Nat. Photonics* **15,** 374-378 (2021).

[89] Wallnöfer, J., Hahn, F., Gündoğan, M., Sidhu, J. S., Wiesner, F., Walk, N., Eisert. J. and Wolters, J. Simulating quantum repeater strategies for multiple satellites. *Commun. Phys.* **5,** 169 (2022).

[90] Khatri, S., Brady, A. J., Desporte, R. A., Bart, M. P. and Dowling, J. P. Spooky action at a global distance: analysis of space-based entanglement distribution for the quantum internet. *npj Quantum Inf* **7,** 4 (2021).

[91] Aspelmeyer, M., Jennewein, T., Pfennigbauer, M., Leeb, W. R. and Zeilinger, A. Long-distance quantum communication with entangled photons using satellites. *IEEE J. Selected Top. Quant. Electron.* **9,** 1541-1551 (2003).

[92] Tang, Z. Chandrasekara, R., Tan, Y. C., Cheng, C., Sha, L., Hinag, G. C., Oi, D. K. L. and Ling, A. Generation and analysis of correlated pairs of photons aboard a nanosatellite. *Phys. Rev. Appl.* **5,** 054022 (2016).

[93] Bedington, R., Bai. X., Truong-Cao, E., Tan, Y. C., Durak, K., Zafra, A. V., Grieve, J. A., Oi, D. K. L. and Ling, A. Nanosatellite experiments to enable future space-based QKD missions. *EPJ Quant. Technol.* **3,** 12 (2016).

[94] Takenaka, H., Carrasco-Cassado, A., Fujiwara, M., Kitamura, M., Sasaki, M. and Toyoshima, M. Satellite-to-ground quantum-limited communication using a 50-kg-class microsatellite. *Nat. Photonics* **11,** 502-508 (2017).

[95] Ren, J.-G. et al. Ground-to-satellite quantum teleportation. *Nature* **549,** 70-73 (2017).

[96] Oi, D. K. L. et al. Cubesat quantum communications mission. *EPJ Quant. Technol.* **4,** 6 (2017).

[97] Yin, J. et al. Satellite-based entanglement distribution over 1200 kilometers. *Science* **356,** 1140-1144 (2017).

[98] Kerstel, E., Gardelein, A., Barthelemy, M., The CSUG Team, Fink, M., Joshi, S. K. and Ursin, R. Nanobob: a cubesat mission concept for quantum communication experiments in an uplink configuration. *EPJ Quant. Technol.* **5,** 6 (2018).

[99] Dai, H. et al. Towards satellite-based quantum-secure time transfer. *Nat. Phys.* **16,** 848-852 (2020).

[100] Yin, J. et al. Entanglement-based secure quantum cryptography over 1,120 kilometres. *Nature* **582,** 501-505 (2020).

[101] Cao, Y. et al. Long-distance free-space measurement-device-independent quantum key distribution. *Phys. Rev. Lett.* **125,** 260503 (2020).

[102] Chen, Y.-A. et al. An integrated space-to-ground quantum communication network over 4,600 kilometres. *Nature* **589,** 214-219 (2021).

[103] Pirandola, S. Satellite quantum communications: Fundamental bounds and practical security. *Phys. Rev. Research* **3,** 023130 (2021).

[104] Eberhard, P. H. and Ross, R. R. Quantum field theory cannot provide faster than light communication. *Found. Phys.* **2,** LBL-24984 (1988).

[105] Życzkowski, K., Horodecki, P., Sanpera, A. and Lewenstein, M. Volume of the set of separable states. *Phys. Rev. A* **58,** 883 (1998).

[106] Vidal, G. and Werner, R. F. Computable measure of entanglement. *Phys. Rev. A* **65,** 032314 (2002).

[107] Plenio, M. B. Logarithmic negativity: a full entanglement monotone that is not convex. *Phys. Rev. Lett.* **95,** 090503 (2005).

[108] Bourgoin. J.-P. et al. A comprehensive design and performance analysis of low Earth orbit satellite quantum communication. *New J. Phys.* **15,** 023006 (2013).

[109] Hogg, D., Berry, D. W. and Lvovsky, A. Efficiencies of quantum optical detectors. *Phys. Rev. A* **90,** 053846 (2014).

[110] Stevens, M. J., Glancy, S., Nam, S. W. and Mirin, R. P. Third-order antibunching from an imperfect single-photon source. *Opt. Express* **22,** 3244-3260 (2014).

[111] Lucamarini, M., Yuan, Z. L., Dynes, J. F. and Shields, A. J. Overcoming the rate-distance limit of quantum key distribution without quantum repeaters. *Nature* **557,** 400-403 (2018).

[112] Chen, J.-P. et al. Sending-or-not-sending with independent lasers: secure twin-field quantum key distribution over 509 km. *Phys. Rev. Lett.* **124,** 070501 (2020).

[113] Pittaluga, M., Minder, M., Lucamarini, M., Sanzaro, M., Woodward, R. I., Li, M.-J., Yuan, Z. and Shields, A. J. 600-km repeater-like quantum communications with dual-band stabilization. *Nat. Photon.* **15,** 530-535 (2021).

[114] Liu, H. et al. Field test of twin-field quantum key distribution through sending-or-not-sending over 428 km. *Phys. Rev. Lett.* **126,** 250502 (2021).

[115] Stobińska, M. et al. Quantum interference enables constant-time quantum information processing. *Sci. Adv.* **5,** eaau9674 (2019).

[116] Mycroft, M. E., Buraczewski, A., Barz, S. and Stobińska, M. Long-range distribution of multiphoton entanglement. In: *Quantum Information and Measurement (QIM) V: Quantum Technologies*, OSA Technical Digest, Optica Publishing Group, paper F5A.82 (2019).

[117] Mycroft, M. E., Buraczewski, A., Barz, S. and Stobińska, M. Long-range distribution of multiphoton entanglement. In: *2019 IEEE Photonics Society Summer Topical Meeting Series (SUM)* pp. 1-2 (2019).

[118] Mycroft, M. E., McDermott, T., Buraczewski, A. and Stobińska, M. Proposal for distribution of multi-photon entanglement with TF-QKD rate-distance scaling. Preprint at arXiv:1812.10935 (2021).

[119] Thekkadath, G. S. et al. Quantum-enhanced interferometry with large heralded photon-number states. *npj Quantum Inf.* **6,** 89 (2020).

[120] Genovese, M. Experimental quantum enhanced optical interferometry. *AVS Quantum Sci.* **3,** 044702 (2021).

[121] Caves, C. M. Quantum-mechanical noise in an interferometer. *Phys. Rev. D* **23,** 1693 (1981).

[122] McKenzie, K., Shaddock, D. A., McClelland, D. E., Buchler, B. C. and Lam, P. K. Experimental demonstration of a squeezing-enhanced power-recycled Michelson interferometer for gravitational wave detection. *Phys. Rev. Lett.* **88,** 231102 (2002).

[123] Berni, A. A., Gehring, T., Nielsen, B. M., Händchen, V., Paris, M. G. A. and Andersen, U. L. Ab initio quantum-enhanced optical phase estimation using real-time feedback control. *Nature Photon* **9,** 577–581 (2015).

[124] Lloyd, S. Enhanced sensitivity of photodetection via quantum illumination. *Science* **321,** 1463-1465 (2008).

[125] Ortolano, G., Losero, E., Pirandola, S., Genovese, M. and Ruo-Berchera, I. Experimental quantum reading with photon counting. *Science Advances* **7,** 4 (2021).

[126] Boto, A. N., Kok, P., Abrams, D. S., Braunstein, S. L., Williams, C. P. and Dowling, J. P. Quantum-interferometric optical lithography: exploiting entanglement to beat the diffraction limit. *Phys. Rev. Lett.* **85,** 2733 (2000).

[127] D'Angelo, M., Chekhova, M. V. and Shih, Y. Two-photon diffraction and quantum lithography. *Phys. Rev. Lett.* **87,** 013602 (2001).

[128] Kalashnikov, D., Paterova, A., Kulik, S. et al. Infrared spectroscopy with visible light. *Nature Photon.* **10,** 98–101 (2016).

[129] The LIGO Scientific Collaboration. A gravitational wave observatory operating beyond the quantum shot-noise limit. *Nature Phys.* **7,** 962–965 (2011).

[130] Aasi, J. et al. Enhanced sensitivity of the LIGO gravitational wave detector by using squeezed states of light. *Nature Photon.* **7,** 613–619 (2013).

[131] The Virgo Collaboration. Increasing the astrophysical reach of the advanced Virgo detector via the application of squeezed vacuum states of light. *Phys. Rev. Lett.* **123,** 231108 (2019).

[132] Crespi, A., Lobino, M., Matthews, J. C. F., Politi, A., Neal, C. R., Ramponi, R., Osellame, R. and O'Brien, J. L. Measuring protein concentration with entangled photons. *Appl. Phys. Lett.* **100,** 233704 (2012).

[133] Wolfgramm, F., Vitelli, C., Beduini, F. A., Godbout, N. and Mitchell, M. W. Entanglement-enhanced probing of a delicate material system. *Nat. Photon.* **7,** 28-32 (2013).

[134] Taylor, M. A., Janousek, J., Daria, V., Knittel, J., Hage, B., Bachor, H.-A. and Bowen, W. P. Biological measurement beyond the quantum limit. *Nat. Photon.* **7,** 229-233 (2013).

[135] Cimini, V., Mellini, M., Rampioni, G., Sbroscia, M., Leoni, L., Barbieri, M. and Gianani, I. Adaptive tracking of enzymatic reactions with quantum light. *Opt. Express* **27,** 35245-35256 (2019).

[136] Kay, S. M. *Fundamentals of statistical signal processing: Estimation theory*, New Jersey: Prentice-Hall (1993).

[137] Helstrom, C. W. *Quantum detection and estimation theory*, New York: Academic Press (1976).

[138] Holevo, A. S. *Probabilistic and statistical aspects of quantum theory*, Amsterdam: North-Holland (1982).

[139] Braunstein, S. L. and Caves, C. M. Statistical distance and the geometry of quantum states. *Phys. Rev. Lett.* **72,** 3439 (1994).

[140] Bollinger, J. J., Itano, W. M., Wineland, D. J. and Heinzen, D. J. Optimal frequency measurements with maximally correlated states. *Phys. Rev. A* **54,** R4649–R4652 (1996).

[141] Mitchell, M. W., Lundeen, J. S. and Steinberg, A. M. Super-resolving phase measurements with a multiphoton entangled state. *Nature* **429,** 161–164 (2004).

[142] Walther, P., Pan, J.-W., Aspelmeyer, M., Ursin, R., Gasparoni, S. and Zeilinger, A. De Broglie wavelength of a non-local four-photon state. *Nature* **429,** 158–161 (2004).

[143] Nagata, T., Okamoto, R., O'Brien, J. L., Sasaki, K. and Takeuchi, S. Beating the standard quantum limit with four-entangled photons. *Science* **316,** 726–729 (2007).

[144] Kim, H., Park, H. S. and Choi, S.-K. Three-photon N00N states generated by photon subtraction from double photon pairs. *Opt. Express* **17,** 19720–19726 (2009).

[145] Afek, I., Ambar, O. and Silberberg, Y. High-NOON states by mixing quantum and classical light. *Science* **328,** 879–881 (2010).

[146] Matthews, J. C. F., Politi, A., Bonneau, D. and O'Brien, J. L. Heralding two-photon and four-photon path entanglement on a chip. *Phys. Rev. Lett.* **107,** 163602 (2011).

[147] Ulanov, A. E., Fedorov, I. A., Sychev, D., Grangier, P. and Lvovsky, A. Loss-tolerant state engineering for quantum-enhanced metrology via the reverse Hong–Ou–Mandel effect. *Nat. Commun.* **7,** 11925 (2016).

[148] Slussarenko, S., Weston, M. W., Chrzanowski, H. M., Shalm, L. K., Verma, V. B., Nam, S. W. and Pryde, G. J. Unconditional violation of the shot-noise limit in photonic quantum metrology. *Nat. Photonics* **11,** 700 (2017).

[149] Datta, A., Zhang, L., Thomas-Peter, N., Dorner, U., Smith, B. J. and Walmsley, I. A. Quantum metrology with imperfect states and detectors. *Phys. Rev. A* **83,** 063836 (2011).

[150] Dorner, U., Demkowicz-Dobrzański, R., Smith, B. J., Lundeen, J. S., Wasilewski, W., Banaszek, K. and Walmsley, I. A. Optimal quantum phase estimation. *Phys. Rev. Lett.* **102,** 040403 (2009).

[151] Kacprowicz, M., Demkowicz-Dobrzański, R., Wasilewski, W., Banaszek, K. and Walmsley, I. Experimental quantum-enhanced estimation of a lossy phase shift. *Nat. Photonics* **4,** 357 (2010).

[152] Demkowicz-Dobrzański, R., Banaszek, K. and Schnabel, R. Fundamental quantum interferometry bound for the squeezed-light-enhanced gravitational wave detector GEO 600. *Phys. Rev. A* **88,** 041802 (2013).

[153] Sun, F., Liu, B. H., Gong, Y. X., Huang, Y. F., Ou, Z. Y. and Guo, G. C. Experimental demonstration of phase measurement precision beating standard quantum limit by projection measurement. *EPL* **82,** 24001 (2008).

[154] Xiang, G.-Y., Higgins, B. L., Berry, D., Wiseman, H. M. and Pryde, G. Entanglement-enhanced measurement of a completely unknown optical phase. *Nat. Photonics* **5,** 43–47 (2011).

[155] Thomas-Peter, N., Smith, B. J., Datta, A., Zhang, L., Dorner, U. and Walmsley, I. A. Real-world quantum sensors: Evaluating resources for precision measurement. *Phys. Rev. Lett.* **107,** 113603 (2011).

[156] Xiang, G., Hofmann, H. and Pryde, G. Optimal multi-photon phase sensing with a single interference fringe. *Sci. Rep.* **3,** 2684 (2013).

[157] Jin, R.-B., Fujiwara, M., Shimizu, R., Collins, R. J., Buller, G. S., Yamashita, T., Miki, S., Terai, H., Takeoka, M. and Sasaki, M. Detection-dependent six-photon Holland-Burnett state interference. *Sci. Rep.* **6,** 36914 (2016).

[158] Matthews, J. C. F., Zhou, X.-Q., Cable, H., Shadbolt, P. J., Saunders, D. J., Durkin, G. A., Pryde, G. J. and O'Brien, J. L. Towards practical quantum metrology with photon counting. *npj Quantum Inf.* **2,** 1–7 (2016).

[159] Demkowicz-Dobrzanski, R., Dorner, U., Smith, B. J., Lundeen, J. S., Wasilewski, W., Banaszek, K. and Walmsley, I. A. Quantum phase estimation with lossy interferometers. *Phys. Rev. A* **80,** 013825 (2009).

[160] Pezzé, L. and Smerzi, A. Entanglement, Nonlinear Dynamics, and the Heisenberg Limit. *Phys. Rev. Lett.* **102,** 100401 (2009).

[161] Giovanetti, V., Lloyd, S. and Maccone, L. Quantum metrology. *Phys. Rev. Lett.* **96,** 010401 (2006).

[162] Xiang, G. Y., Higgins, B. L., Berry, D. W., Wiseman, H. M. and Pryde, G. J. Entanglement-enhanced measurement of a completely unknown optical phase. *Nature Photon.* **5,** 43–47 (2011).

[163] Daryanoosh, S., Slussarenko, S., Berry, D. W., Wiseman, H. M. and Pryde, G. J. Experimental optical phase measurement approaching the exact Heisenberg limit. *Nat. Commun.* **9,** 4606 (2018).